



Universität
Augsburg
University



Universität Augsburg
Lehrstuhl für
Experimentalphysik I

Hybrid LiNbO_3 -(Al)GaAs devices for quantum dot optomechanics

Dissertation
zur Erlangung des akademischen Grades
Dr. rer. nat.

Eingereicht an der
Mathematisch Naturwissenschaftlich Technischen Fakultät
der Universität Augsburg

von

Emeline D. S. Nysten

Augsburg, August 2021



SAWtrain
network



nim
nanosystems initiative munich

Erstgutachter: Prof. Dr. Hubert Krenner
Zweitgutachter: Prof. Dr. Wolfgang Brütting
Datum der mündlichen Prüfung: 29.10.2021

Abstract

Acoustic phonons, in the form of elastic waves, couple easily to many excitations present in condensed matter which makes them ideally suited for the design and realization of hybrid quantum systems. In this context, surface acoustic waves (SAWs), mechanical waves confined to the surface of solid state substrates and generated by interdigital transducers (IDTs) on piezoelectric substrates, have been proven to be a useful tool for the control of quantum systems. In parallel, semiconductor quantum dots (QDs) have also been considered as an essential part of future quantum systems and technology as an optically active and addressable two-level system and as an efficient source of single and indistinguishable photons. In this work, we focus on the control of optically active semiconductor QDs by the mechanical field of a SAW through the deformation potential coupling. The strength of this interaction can be quantified by a coupling parameter just like for many hybrid quantum devices, in this case, it is the optomechanical coupling parameter γ_{OM} linking the modulation of the emission energy as a function of the surface displacement of the SAW.

In this thesis, the goal is to increase the optomechanical coupling between the two systems. For this purpose, the III-V semiconductor quantum dots are transferred onto a strong piezoelectric substrate, LiNbO_3 . After a brief introduction on surface acoustic waves, semiconductor quantum dots and their interaction, the fabrication technique used to create the hybrid devices analysed in this work is presented. This technique, called epitaxial lift-off, is used to release a QD membrane from its GaAs substrate to transfer it onto a LiNbO_3 SAW-chip.

Next, the coupling of the surface acoustic waves is studied first through finite element simulations which show an increased optomechanical coupling parameter due to a localisation of the SAW field inside the membrane for increasing SAW frequency. The simulations results are confirmed by fabricating and measuring an hybridised SAW sample. The coupling of the wave to the membrane is quantified by measuring both the SAW signal transmitted across the hybridised delay line and the optomechanical response of the dots inside the epilayer.

To further increase the sound-matter coupling, the epilayer was transferred inside a SAW resonator cavity where both the electrical reflection of the resonator and the optomechanical coupling of the dots to the resonator modes were recorded. The QD-SAW coupling exhibits a more complex behaviour than expected and finite element method simulations show that the origin of this behaviour is not the classical linear

deformation potential coupling.

Finally, the transferred epilayer can be patterned into more complex structures such as photonic ring resonators and their access waveguides. The interaction between the SAW, the QDs and the resonators was measured and analysed. The QDs were tuned in and out of resonance with the ring resonator modes. In addition to the photonic modes, the emergence of phononic resonances was observed. These phononic resonances showed an interesting non-linear behaviour which is analysed in more detail.

Zusammenfassung

Akustische Phononen in Form von elastischen Wellen koppeln leicht an viele Anregungen in kondensierter Materie, wodurch sie sich ideal für die Entwicklung und die Realisierung hybrider Quantensysteme eignen. In diesem Zusammenhang haben sich akustische Oberflächenwellen (SAWs), mechanische Wellen, deren Ausbreitung auf die Oberfläche von Festkörsubstraten beschränkt ist und mittels Interdigitalwandlern (IDTs) auf piezoelektrischen Substraten erzeugt werden können, als nützliches Werkzeug zur Steuerung von Quantensystemen erwiesen. Gleichzeitig werden Halbleiter-Quantenpunkte (QDs) als wesentlicher Bestandteil zukünftiger Quantensysteme und -technologien betrachtet, da es sich bei diesen um optisch aktive und einzeln ansprechbare Zwei-Niveau-Systeme und damit um effiziente Quellen einzelner und ununterscheidbarer Photonen handelt. Diese Arbeit konzentriert sich auf die Kontrolle optisch aktiver Halbleiter-QDs durch das mechanische Feld einer SAW mittels der Deformationspotentialkopplung. Die Stärke dieser Wechselwirkung kann, wie bei vielen hybriden Quantenbauelementen, durch einen Kopplungsparameter quantifiziert werden, in diesem Fall durch den optomechanischen Kopplungsparameter γ_{OM} , der die Modulation der Quantenpunkt-Emissionsenergie mit der Auslenkung der Oberfläche durch die SAW verknüpft.

Ziel dieser Arbeit ist es, die optomechanische Kopplung zwischen den beiden Systemen zu erhöhen. Dazu werden die III-V Halbleiter-Quantenpunkte auf ein starkes piezoelektrisches Substrat, LiNbO_3 , übertragen. Nach einer kurzen Einführung zu akustischen Oberflächenwellen, Halbleiter-Quantenpunkten und deren Wechselwirkung wird die Fabrikationstechnik zur Herstellung der in dieser Arbeit analysierten Hybridbauelemente vorgestellt. Diese Technik, die als epitaktischer Lift-Off bezeichnet wird, wird verwendet, um eine QD-Membran von ihrem GaAs-Substrat zu lösen, um sie auf einen LiNbO_3 -SAW-Chip zu übertragen.

Daraufhin wird die Kopplung der akustischen Oberflächenwellen zur QD-Membran zunächst durch Finite-Elemente-Simulationen untersucht. Dabei zeigt sich mit steigender SAW-Frequenz, aufgrund einer Lokalisierung des SAW-Feldes innerhalb der Membran, ein erhöhter optomechanischer Kopplungsparameter. Die Simulationsergebnisse werden durch die Herstellung und Untersuchung einer hybridisierten SAW-Probe bestätigt. Die Kopplung der Oberflächenwelle an die Membran wird quantifiziert, indem sowohl das über die hybridisierte Verzögerungsleitung übertragene SAW-Signal, als auch die optomechanische Reaktion der Quantenpunkte innerhalb der Epischicht gemessen werden.

Um die Schall-Materie-Kopplung weiter zu erhöhen, wurde die Epischicht in einen SAW-Resonator transferiert. Für dieses System wurde sowohl die elektrische Reflexion des Resonators als auch die optomechanische Kopplung der Quantenpunkte an die Resonatormoden untersucht. Die QD-SAW-Kopplung zeigt dabei ein komplexeres Verhalten als erwartet und Simulationen mittels der Finite-Elemente-Methode zeigen, dass der Ursprung dieses Verhaltens nicht in der klassischen linearen Verformungspotentialkopplung liegt.

Abschließend wird eine übertragene Epischicht weiter strukturiert um komplexere photonische Strukturen wie Ringresonatoren und deren Zugangswellenleiter herzustellen. Die Interaktion zwischen SAW, QDs und Resonatoren wurde dabei gemessen und im Detail analysiert. Dabei kann die SAW dazu benutzt werden, um einen Quantenpunkt dynamisch in Resonanz mit der Ringresonatormode zu bringen. Neben den photonischen Resonanzen kann dabei auch das Auftreten von phononischen Moden innerhalb der Ringresonatoren beobachtet werden. Diese phononischen Resonanzen zeigen ein ausgeprägtes nichtlineares Verhalten, welches im Detail analysiert wird.

Contents

Abstract	iii
Zusammenfassung	v
Introduction	1
1 Surface Acoustic Waves	5
1.1 Acoustic waves in solids: basic properties	5
1.2 Excitation of surface acoustic waves: interdigital transducer	9
1.3 Reflective transducer: Bragg reflectors	13
1.3.1 Infinite-length grating	13
1.3.2 Finite-length grating	16
1.3.3 Reflection coefficient of individual electrodes	18
1.4 One-port resonator	19
2 Quantum Dots Optomechanics	23
2.1 Semiconductor quantum dots	23
2.1.1 Fundamentals of semiconductor	23
2.1.2 Semiconductor heterostructures: quantum dot properties	27
2.2 Interfacing quantum dots with surface acoustic waves: deformation potential coupling	31
2.3 Optical and electrical measurement setup	33
2.3.1 Time-integrated spectroscopy	33
2.3.2 Time-resolved spectroscopy	37
3 Semiconductor Heterointegration	41
3.1 Epitaxial growth of semiconductor quantum dots	41
3.1.1 Droplet-etched GaAs/(Al)GaAs QDs	42
3.1.2 Self-assembled InAs QDs	43
3.2 SAW-chip fabrication	44
3.2.1 E-beam lithography	44
3.2.2 Metallisation and lift-off	44
3.3 Epitaxial lift-off and transfer	45

3.3.1	Palladium adhesion layer	45
3.3.2	Confirmation of the Pd-GaAs interdiffusion	46
3.4	Post-processing of the (Al)GaAs membrane	48
3.4.1	Photolithography and chemical etching	48
3.4.2	Photonic devices	49
4	Analysis of the SAW Propagation in Fused (Al)GaAs-LiNbO₃ Hybrids	53
4.1	Finite element simulation of QD-SAW coupling	53
4.2	Sample geometry	57
4.3	Electrical characterisation	58
4.4	Optomechanical characterisation	59
5	Quantum Dots and Surface Acoustic Wave Resonators	65
5.1	Samples geometry	65
5.2	Electrical characterisation	67
5.3	Optomechanical characterisation	72
5.3.1	Position dependent QD-resonator coupling and time-domain analysis	73
5.3.2	QD-resonator coupling	76
5.4	FEM simulation	81
5.4.1	Geometry of the resonators model	82
5.4.2	Bare resonators	84
5.4.3	Hybridised resonators	84
6	Perspective: Quantum Dots and Photonic Structures on LiNbO₃	87
6.1	Ring resonator: whispering gallery mode cavities	87
6.2	Design and fabrication	90
6.3	Photonic mode: SAW tuning of QD in/out of resonance	92
6.4	Observation of phononic modes	97
6.4.1	Power dependence of the phononic modes: Duffing oscillator behaviour	99
	Conclusion and Perspectives	103
	Appendices	105
A	Materials Parameters	107
A.1	Voigt notation	107
A.2	Rotation matrices	109
A.3	LiNbO ₃ material parameters	110
A.4	GaAs material parameters	111
A.4.1	Elasto-optic tensor of GaAs	113
A.5	Al _x Ga _(1-x) As material parameters	113
	List of Symbols	116

List of Acronyms	118
Bibliography	127
List of Publications	129
Acknowledgement	131

Introduction

Elastic waves and acoustic phonons are easily coupled to many excitations in condensed matter. This unique property makes them ideally suited for the design and realization of hybrid quantum systems [1]. In this concept, surface acoustic waves (SAWs), mechanical waves confined to the surface of solid state substrates and generated by interdigital transducers (IDTs) on piezoelectric substrates, have been proven to be a useful tool for the control of quantum systems [2]. SAWs have been theoretically demonstrated to act as a versatile on-chip quantum transducer and to enable the dynamic control of quantum systems [3, 4]. Experimentally, SAWs have been used to control superconducting qubits, to transfer quantum state between superconducting qubits using single SAW quanta, to transport electrons and spin between electrostatic quantum dots (QDs) and to coherently control optically active quantum dots [2].

Superconducting qubits can be coupled to the SAW by changing the geometry of the capacitance of a transmon qubit into an IDT and the same type of quantum electrodynamics experiments from the optical domain could be reproduced in the acoustic domain [5]. Additionally, superconducting qubits were integrated into high-Q SAW resonators and strong interactions between both systems were observed [6, 7]. Using a SAW resonator with an IDT coupled to two qubits, the quantum state transfer between two superconducting qubits using single SAW phonon has been demonstrated [8].

SAWs were also demonstrated to efficiently and on-demand transport individual electrons between two electrostatically defined quantum dots in a 2D semiconductor heterostructure [9, 10]. With the same technique, the transfer of spin information between two QDs was demonstrated [11], as well as the generation of a stream of single photons by pumping single electrons into a region of holes [12].

In this work, we focus on the control of optically active semiconductor QDs by a SAW [13]. On one hand, the electric field of a SAW can be used to transport charge carriers in the quantum well connected to the dots. These charge carriers can then be injected inside the QDs [14, 15]. Additionally, the occupancy state of the dots can be controlled. Depending on the polarisation of the electric field at the position of the QD during the acoustic cycle, a certain charge carrier species is predominantly injected into the quantum emitter, influencing the occupancy state that is formed [14, 16, 17]. Additionally, by controlling the timing of the optical excitation of the QD during the acoustic cycle, the emission of the QD can be switched between a charged and a neutral exciton [18]. On the other hand, the mechanical field of the SAW dynamically modulates

the emission energy of the QDs through the deformation potential coupling [19, 20, 21].

This work focusses on this optomechanical coupling between QDs and SAWs. Just like for other hybrid quantum systems, the strength of the interaction can be quantified by a coupling parameter, in this case the optomechanical coupling parameter γ_{OM} [3]. The goal of this work is to increase the optomechanical coupling between the semiconductor quantum dots and the surface acoustic waves. For this purpose, the III-V semiconductor quantum dots are combined with a strong piezoelectric substrate, LiNbO₃. Indeed, while SAWs can be generated directly on III-V semiconductors and their heterostructures due to their piezoelectricity, they have a low electromechanical coupling coefficient (GaAs $K^2 \approx 0.07\%$). This means that the conversion of the applied electrical power to acoustic power by the transducers on that substrate is not efficient. On the other hand, LiNbO₃ has a much larger electromechanical coupling coefficient ($K^2 \approx 5\%$) but does not provide any type of high-quality qubit system of interest for the realisation of hybrid quantum systems. To combine both materials and their qualities, we use an epitaxial lift-off technique to release a QD membrane from its GaAs substrate and to transfer it on top of a LiNbO₃ substrate [22, 23, 24].

This work starts with introducing the theory of surface acoustic waves in solids in **Chapter 1**. The solution to the wave equation in a semi-infinite space is calculated and the excitation of surface acoustic waves by interdigital transducers (IDTs) using the reverse piezoelectric effect is explained. Furthermore, the different geometries of IDTs used in devices throughout this work are described. In addition to the classical delay line SAW devices, the one-port SAW resonator is also introduced as the combination of two Bragg reflectors containing the acoustic field and bracketing a simple single finger IDT. The reflective behaviour of the reflectors is first discussed followed by the one-port resonator and its electrical characteristics.

Following this, **Chapter 2** describes the fundamentals of semiconductors and semiconductor quantum dots as well as their optical properties. Additionally, the interaction of surface acoustic waves with the QDs is explained and the measurement schemes used to quantify this interaction are described.

Chapter 3 introduces the concept of semiconductor heterointegration used to fabricate the samples investigated in this work. The epitaxial growth of semiconductor QDs is presented as well as the lithography process used for the SAW chip fabrication. The epitaxial lift-off and transfer of a semiconductor QD membrane onto a LiNbO₃ SAW-chip is presented and is proved to be a successful fabrication technique for the hybrid semiconductor-LiNbO₃ samples investigated in this work. The post-processing of the as-transferred membrane is also explained in detail.

The coupling of surface acoustic waves inside the transferred QD membrane is investigated in **Chapter 4**. First, finite element simulations of the QD-SAW coupling inside a unit cell show a localisation of the SAW field inside the membrane. To confirm this observation, a hybridised sample was fabricated and the coupling of the SAW to the epilayer was quantified by measuring both the SAW signal transmitted across the hybridised delay line and the optomechanical response of the dots.

To further increase the sound-matter coupling, the epilayer was transferred inside a SAW resonator cavity and the analysis of this sample is presented in **Chapter 5**. The electrical reflection of the resonator as well as the optomechanical coupling of the dots

to the resonator modes were recorded. The QD-SAW coupling exhibits a more complex behaviour than expected and finite element method simulations shows that the origin of this behaviour is not the classical linear deformation potential coupling.

In **Chapter 6**, the transferred epilayer was patterned into more complex photonic structures: ring resonators and their access waveguides. The interactions between the SAW, the QDs and the resonators were measured and analysed. The QDs are tuned in and out of resonance with the ring resonator mode and the emergence of phononic resonances is observed. These phononic resonances show an interesting non-linear behaviour which is analysed in more detail.

Surface Acoustic Waves

In this chapter, we are discussing the basic properties and theory concerning surface acoustic waves (SAW) and the transducers and resonators used in this work to control the acoustic field. First, the basic properties of surface acoustic waves on piezoelectric substrates are discussed. The excitation of surface acoustic waves using interdigital transducers (IDT) is then discussed and the IDT geometries used in this work are described and their frequency response is calculated. After the description of the classical IDTs, we introduce one-port SAW resonators. These cavities are made of two Bragg reflectors containing the acoustic field and bracketing a simple single finger IDT. The reflective behaviour of the reflectors is first discussed followed by the one-port resonator and its electrical characteristics. This chapter is based largely on the books of David Morgan [25], of Daniel Royer and Eugène Dieulesaint [26, 27] and of Supriyo Datta [28]. The theoretical development has been summarised and for more details, the books are referenced.

1.1 Acoustic waves in solids: basic properties

To describe the properties of acoustic waves inside a solid, we have to first consider the elastic behaviour of anisotropic solids. In this approach, the displacement $\mathbf{u} = (u_1, u_2, u_3)$ of a particle, by definition an elementary region of the material, from its equilibrium position $\mathbf{x} = (x_1, x_2, x_3)$ to a position $\mathbf{x} + \mathbf{u}$ is considered. Internal forces will then try to restore the particle to its initial position \mathbf{x} in order to re-establish the equilibrium. Since there are no internal forces present when the solid is displaced as a whole or rotated, it is more convenient to consider the deformation or strain of the material which is defined as:

$$S_{ij} = \frac{1}{2} \left(\frac{\partial u_i}{\partial x_j} + \frac{\partial u_j}{\partial x_i} \right), \quad i, j = 1, 2, 3 \tag{1.1}$$

for each point \mathbf{x} . From this definition, the strain is null for a material displacement as a whole and for any rotation of the solid. Additionally, the strain tensor is symmetrical, $S_{ij} = S_{ji}$, which reduces the number of independent components from 9 to 6. The

internal forces due to the strain inside the material are described by the stress tensor T_{ij} . In elastic materials, this stress tensor is proportional to the strain tensor for small strain:

$$T_{ij} = c_{ijkl}S_{kl}, \quad i, j, k, l = 1, 2, 3 \quad (1.2)$$

This equation is a generalisation of Hooke's law and the proportional constant c_{ijkl} is called the stiffness or elasticity tensor which is generally a fourth rank tensor with 81 components. Taking into account that the stress tensor is symmetrical just like the strain tensor, the number of independent components is reduced to 36 as $c_{ijkl} = c_{jikl}$ and $c_{ijkl} = c_{ijlk}$. These relations are called the minor symmetries of the stiffness tensor. Additionally, thermodynamic considerations shows that the first pair of indices can be interchanged with the second pair so that $c_{ijkl} = c_{klij}$. This relation, called the major symmetry, further reduces the number of independent components to 21. The addition of crystal symmetries also has an impact on the number of components for the stiffness tensor. For example, a cubic crystal structure such as the one of GaAs, InAs and (Al)GaAs only has three independent constants in its stiffness tensor.

Since surface acoustic waves are a dynamic deformation of the material, the displacement \mathbf{u} is a function of time and obeys Newton's second law of motion, which combined with the previous equations leads to the well-known wave equation. In this equation, the force per unit of volume $\frac{\partial T_{ij}}{\partial x_j}$ is equal to the density of the material ρ multiplied by the acceleration $\frac{\partial^2 u_i}{\partial t^2}$:

$$\rho \frac{\partial^2 u_i}{\partial t^2} = \frac{\partial T_{ij}}{\partial x_j}, \quad i, j = 1, 2, 3 \quad (1.3)$$

This equation is valid for any anisotropic material but does not consider piezoelectricity which is crucial for the excitation of SAWs in acoustic devices as shown later. Piezoelectricity occurs in crystal structures missing an inversion symmetry and couples the elastic stress and strain to the electrical field and displacement inside the solid. In piezoelectric materials, the stress tensor is not only dependent on the elastic strain but also on the electric field \mathbf{F} . Assuming that all the components are small enough that the relationship can be taken as linear, the stress tensor T_{ij} can be written as:

$$T_{ij} = c_{ijkl}S_{kl} + e_{kij}F_k, \quad i, j, k, l = 1, 2, 3 \quad (1.4)$$

where e_{kij} is the piezoelectric tensor. Inversely, the electric displacement \mathbf{D} is given by:

$$D_i = \epsilon_{ij}F_j + e_{ijk}S_{jk}, \quad i, j, k, l = 1, 2, 3 \quad (1.5)$$

where ϵ_{ij} is the permittivity tensor of the material. The piezoelectric tensor, present in both equations, has the symmetry: $e_{ijk} = e_{ikj}$. Since we are now considering the dynamics of both the elastic and electric fields, Newton's equation of motion and the

Maxwell equations have to be solved simultaneously. From this, two solutions can be found. One solution is an electromagnetic wave accompanied by mechanical strain which has the majority of its energy in the electromagnetic part. The other is the elastic wave accompanied by electric field which is the solution we are interested in. This mechanical wave travels much more slowly than electromagnetic waves at a velocity five orders of magnitude smaller than the speed of light. Due to this low velocity, the electric field can be expressed using a quasi-static approach where the electric field is derived from a scalar potential Φ and the magnetic field variation is neglected, $\nabla \times \mathbf{F} = -\frac{\partial \mathbf{B}}{\partial t} \approx 0$:

$$F_i = -\frac{\partial \Phi}{\partial x_i} \quad (1.6)$$

Using this relation, Equation 1.4, the wave equation (Equation 1.3) and the definition of the strain, the equation of motion can be expressed in terms of the displacement of the wave and the electrical potential Φ as:

$$\rho \frac{\partial^2 u_i}{\partial t^2} = e_{kij} \frac{\partial^2 \Phi}{\partial x_j \partial x_k} + c_{ijkl} \frac{\partial^2 u_k}{\partial x_j \partial x_l} \quad (1.7)$$

Assuming that the material is an insulator, there are no free charges and $\nabla \cdot \mathbf{D} = 0$. Equation 1.5 becomes:

$$e_{jkl} \frac{\partial^2 u_l}{\partial x_j \partial x_k} - \epsilon_{jk} \frac{\partial^2 \Phi}{\partial x_j \partial x_k} = 0 \quad (1.8)$$

Both equations 1.7 and 1.8 give us four equations for the four quantities u_i and Φ . The wave motion can then be determined by applying the appropriate boundary conditions. In the case of surface acoustic waves which propagate along the surface of solids, an infinite crystal occupying the half space $x_3 < 0$ is considered and the space above $x_3 > 0$ is vacuum. The wave propagates along the x_1 direction and so the wavefronts are parallel to x_2 . The mechanical boundary condition is that no forces are applied on the free surface at $x_3 = 0$:

$$T_{31}|_{x_3=0} = T_{32}|_{x_3=0} = T_{33}|_{x_3=0} = 0 \quad (1.9)$$

Additionally, since we are only interested in waves contained at the surface of the material, another boundary condition is introduced to the displacement which decays to zero for negative x_3 :

$$u_i|_{x_3 \rightarrow -\infty} = 0 \quad (1.10)$$

The type of waves we are interested in this work are the Rayleigh waves, named after Lord Rayleigh who first described them in 1885 [29]. Rayleigh waves are polarised in

the (x_1, x_3) plane, which contains the surface normal x_3 and the propagation direction x_1 and is known as the sagittal plane. Since piezoelectric materials are considered, electrical boundary conditions are applied to the surface in addition to the mechanical ones. The first condition is that the electrical potential Φ has to be continuous at the surface or interface of the piezoelectric:

$$\Phi|_{\substack{x_3 \rightarrow 0 \\ x_3 < 0}} = \Phi|_{\substack{x_3 \rightarrow 0 \\ x_3 > 0}} \quad (1.11)$$

The second condition is just like for the displacement, the electrical potential decreases to zero far away from the surface:

$$\Phi|_{x_3 \rightarrow \pm\infty} = 0 \quad (1.12)$$

The other electrical boundary conditions are dependent on the material covering the surface of the piezoelectric. Two cases can be distinguished: the surface is covered by a perfect dielectric or the surface is metallised or shorted. In the case of a perfect dielectric with a permittivity $\epsilon_d = 0$, known as the open-circuit condition, there are no free charges and the component of the electrical displacement field normal to the surface is null $D_3|_{x_3=0} = 0$ whereas the components of the electric field tangential to the surface $F_{1,2}$ are continuous. On the other hand, when the surface is covered by a thin film of metal with $\epsilon_d = \infty$, known as the short-circuit condition, the electrical potential Φ as well as the tangential electric fields, $F_{1,2}$ and $D_{1,2}$, vanish at the surface, $\Phi|_{x_3=0} = 0$ and $D_{1,2}|_{x_3=0} = 0$. The normal component of the electrical displacement is then no longer continuous. The two different boundary conditions influence the phase velocity of the SAW, depending on the permittivity of the adjacent medium ϵ_d . The phase velocity for the free surface is defined as v_f and the phase velocity for the metallised surface is defined as v_m . When the medium covering the surface is vacuum, $\epsilon_d = \epsilon_0$, the wave velocity is located between the two extrema: $v_m < v < v_f$. The velocity for a metallised surface is lower than the free surface velocity due to the elimination of the tangential electric field at the surface which partially suppresses the piezoelectricity of the material. Using both of these velocities, the electromechanical coupling coefficient K can be defined by:

$$K^2 = \frac{v_f^2 - v_m^2}{v_f^2 + \frac{\epsilon_d}{\epsilon_p} v_m^2} \quad (1.13)$$

where ϵ_p is the permittivity of the piezoelectric substrate. The square of the electromechanical coupling coefficient defines the proportion of electrical energy which is converted into mechanical energy when it is applied to the surface of the piezoelectric material by the interdigitated transducers introduced in the next section. It is therefore a measure of the suitability of materials, depending on the surface orientation and the wave propagation direction, to produce surface acoustic waves. As presented later in this chapter, it is also an important parameter for the electrical reflectivity of

electrodes inside Bragg reflectors which are used to define SAW cavities. Assuming that both phase velocities are close to each other, $v_f \approx v_m$, the equation for the electromechanical coupling parameter for materials with larger permittivity like LiNbO₃ ($\epsilon_p/\epsilon_0 = 46$ [26]) can be simplified to:

$$K^2 = \frac{2(v_f - v_m)}{v_f(1 + \frac{\epsilon_d}{\epsilon_p})} \quad (1.14)$$

$$\Rightarrow K^2 = 2\frac{v_f - v_m}{v_f} = \frac{2\Delta v}{v_f} \quad (1.15)$$

Due to the complexity of the wave equations, it is usually impossible to solve them analytically for an anisotropic material. Therefore, in this work, we used finite element modelling (FEM) to find the solution for the wave equation. Thanks to the nature of the Rayleigh waves, the model can be solved in a simple 2D model. The details of the simulation are explained in Chapter 3.

Material	Cut and propagation direction	Velocity (m/s)	K^2 (%)	ϵ_p/ϵ_0
LiNbO ₃	Y X	3488	4.8	46
LiNbO ₃	128° Y X	3992	5.3	46
GaAs	(100) [011]	2865	0.07	11

Table 1.1: Characteristic of the piezoelectric materials used for the generation and propagation of surface acoustic waves [26]. LiNbO₃ and GaAs are the main materials investigated in this work.

In table 1.1, the properties of the piezoelectric materials used in this work, LiNbO₃ and GaAs, are summarised. The cut of the crystal is defined by the normal to the surface and the propagation direction of the wave. The table also justify our motivation for transferring the III-V semiconductor QDs onto a stronger piezoelectric material with a better electromechanical coupling parameter K^2 such as LiNbO₃ and, more specifically, the 128° rotated Y-cut of LiNbO₃ with a wave propagation in the X direction.

1.2 Excitation of surface acoustic waves: interdigital transducer

In this section, we are looking at the excitation of surface acoustic waves on a piezoelectric substrate. The excitation is done using the inverse piezoelectric effect in which a deformation of the substrate is induced by applying an electric voltage to the surface of the material. The electrodes used to excite surface acoustic waves have a specific geometry which enables the coupling of the electrodes to the SAW modes. These electrodes are called interdigital transducer (IDT) due to their specific comb-like geometry. One of the simplest implementations of such a structure is depicted schematically in

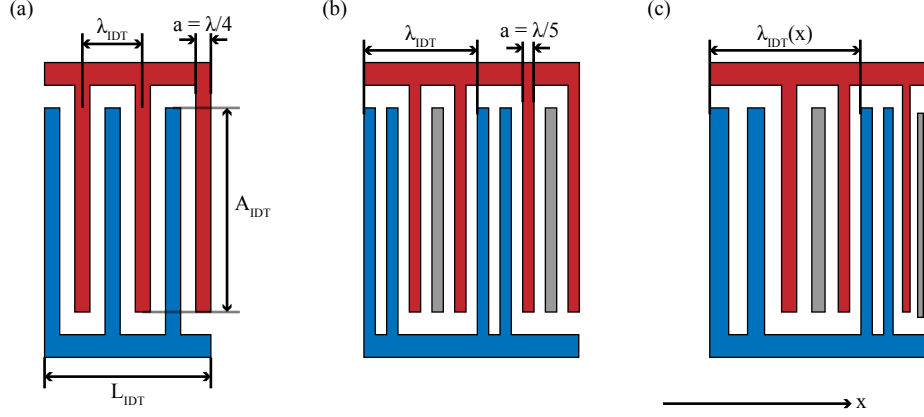


Figure 1.1: Geometry of the IDTs used in this work: (a) Single-finger IDT (b) Split-52 IDT [21] and (c) Chirped Split-52 IDT [30].

Figure 1.1(a). This transducer is called Split-1 or single finger IDT and consists of two comb-shaped interlocked electrodes with opposite polarity. The periodicity of the transducer, indicated by λ_{IDT} in Figure 1.1, is the principal parameter of the IDT. If a radio frequency signal (rf-signal) is applied to the transducer, a SAW will be excited if the frequency of the signal fulfils the resonant condition. This condition relates f_{rf} to λ_{IDT} via v_{SAW} , the phase velocity of the SAW:

$$f_{rf} = \frac{v_{SAW}}{\lambda_{IDT}} \quad (1.16)$$

This resonance condition states that the waves produced by each finger have to constructively interfere in order to launch a complete surface acoustic wave along the $\pm x_1$ direction. The other important parameters are the length of the IDT, L_{IDT} , or the number of fingers contained by the IDT as well as the aperture A_{IDT} and the metallisation ratio a/p of the IDT. The aperture is defined by the overlap of the two electrode fingers, as depicted in figure 1.1(a), and defines the width of the SAW wavefront. The metallisation ratio a/p is the ratio between the width of the electrode fingers a and the pitch or distance between those fingers p . The usual metallisation ratio chosen is $a/p = 0.5$ which sets the width of a finger to $a = \lambda/4$ in the case of a Split-1 geometry.

The frequency response of the IDT can be calculated by using an impulse model [31, 32, 33]. This model considers each finger n of the IDT as an independent source of a plane wave in the $x_1 = x$ direction. The wave is expressed by:

$$A_n \exp\left(i2\pi f \left(\frac{x_n}{v_{SAW}} - t\right)\right) \quad (1.17)$$

There, A_n is the amplitude of the wave emitted by the n -th finger and contains the sign expressing the polarity of this finger. The magnitude of A_n depends on the length and overlap of the fingers and can thus be used to modify the filtering characteristic of the

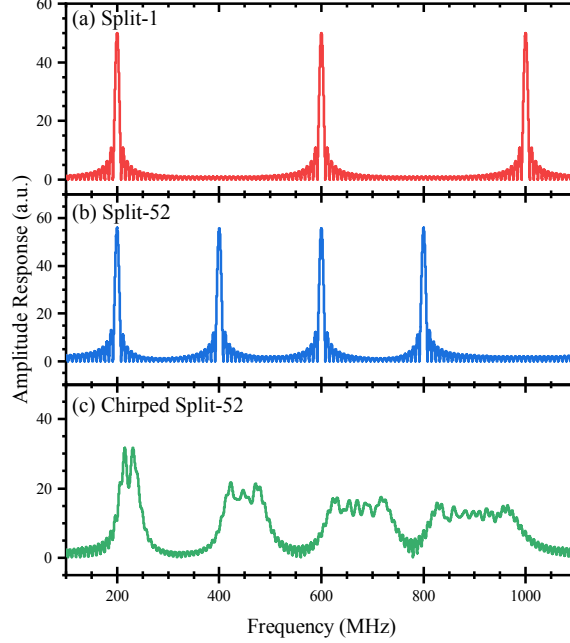


Figure 1.2: Frequency response amplitude $|H(f)|$ for a Split-1 (a), a Split-5-2 (b) [21] and a chirped Split-52 IDT (c) [30]. The fundamental frequency of of the Split-1 and Split-52 IDTs is fixed to $f_1 = 200$ MHz with a length of $L_{IDT} = 500 \mu\text{m}$ on a LiNbO_3 substrate. The same length is taken for the chirped Split-52 IDT but with a fundamental frequency range of $f_1 = [200 : 250]$ MHz.

surface acoustic wave devices and realize any type of frequency response. In this work, A_n is kept constant for all fingers so that the SAW is generated evenly over the whole aperture of the IDT. The parameter x_n is the position of the n -th finger and defines the phase shift between the waves emitted from the different fingers. The frequency response function of the IDT $|H(f)|$, which defines the capability of the IDT to launch a surface acoustic wave at a specific frequency, is then given by:

$$|H(f)| = \left| \sum_{n=1}^N A_n \exp \left(i2\pi \frac{f x_n}{v_{SAW}} \right) \right| \quad (1.18)$$

where N is the number of fingers in the IDT. This expression shows that the frequency response function of an IDT is simply the Fourier transform of the spatial arrangement of the IDT's fingers. In the case of a Split-1 geometry, $A_n = (-1)^n$ and $x_n = n \cdot \frac{\lambda_{IDT}}{2}$ can be inserted in Equation 1.18. The value of the frequency response for a Split-1 IDT with a length $L_{IDT} = 500 \mu\text{m}$ and a fundamental resonance frequency $f_1 = 200$ MHz on a 128° -rotated LiNbO_3 substrate ($v_{SAW} = 4000 \text{ m s}^{-1}$) is plotted in Figure 1.2(a). Aside from the peak at the designed fundamental frequency $f_1 = 200$ MHz, additional peaks can be seen at odd harmonics $f_{SAW,m} = (2 \cdot m + 1) \cdot f_{SAW,1}$, $m \in \mathbb{N}$. This shows that a Split-1 IDT can only excite the odd harmonics of the fundamental resonant frequency. This is due to the fact that, in the case of even harmonics, all the fingers of the electrodes would have the same potential which is not possible in this symmetric

design. Another important characteristic of the frequency response of an IDT is the shape of the peaks. These peaks have the typical Fraunhofer diffraction pattern caused by the finite length of the IDT L_{IDT} . This length can be described by a rectangular function in the spatial finger arrangement x_n . Upon performing the Fourier transform of the spatial finger arrangement to calculate the frequency response, this leads to the formation of the observed $|\text{sinc}(f) = \frac{\sin(f)}{f}|$ envelope function which is typical for this type of transducers. Therefore, the zero points in the amplitude of the frequency response are separated by the inverse of the temporal length of the IDT: $T_{IDT}^{-1} = \frac{v_{SAW}}{L_{IDT}}$. The width of the peaks in the frequency response, and, thus, the spectral bandwidth of the IDT, is inversely proportional to the length of the IDT. This is a logical consequence of the frequency response of the transducer being the Fourier transform of the spatial finger arrangement of the IDT's finger. The temporal length T_{IDT} is also the shortest SAW pulse that the IDT can generate. Therefore, an IDT with a low number of fingers is able to generate a short SAW pulse but presents a large frequency bandwidth whereas a long IDT will not be able to send short pulses but has good filtering capabilities.

To generate both even and odd harmonics, the IDT has to be changed to a non-symmetric finger geometry. One of these geometries is the Split-52 depicted in Figure 1.1(b) and developed by Florian Schüle in at Augsburg Universität [32, 21]. The IDT consists of 5 fingers per period with 2 fingers of one polarity followed by two fingers of the inverse polarity separated by a floating finger. This dummy finger only purpose is to achieve a constant mass loading and, thus, a constant wave velocity and suppress reflections within the IDT. The amplitude of the frequency response of this Split-52 geometry is plotted in Figure 1.2(b) for an IDT length of $L_{IDT} = 500 \mu\text{m}$ and a fundamental resonant frequency $f_1 = 200 \text{ MHz}$. The peaks for the harmonics $f_m = m \cdot f_1$ with $m = 1, 2, 3, 4, 6, \dots$ can clearly be seen. Just like for the even harmonics in the Split-1 IDT, the 5th harmonics is not generated by the Split-52 IDT because all the fingers would have to be at the same potential.

To access an even larger frequency range, a chirp can be introduced into the Split-52 configuration. This chirp is a linear variation of the period $\lambda(x)$ along the axis of the IDT x as illustrated in Figure 1.1(c). This type of geometry was developed by Matthias Weiß at the Universität Augsburg [30, 33]. The linear variation of the SAW wavelength inside the IDT is given by:

$$\lambda(x) = \lambda_0 + \frac{\lambda_1 - \lambda_0}{L_{IDT}} \cdot x = \lambda_0 + \alpha \cdot x \quad (1.19)$$

and leads to the appearance of a fundamental frequency band and its higher harmonics in the frequency response amplitude given by:

$$f_{SAW,n}(x) = m \cdot \frac{v_{SAW}}{\lambda(x)} = m \cdot \frac{v_{SAW}}{\lambda_0 + \alpha \cdot x}, \quad m = 1, 2, 3, 4, 6, \dots \quad (1.20)$$

All the frequency bands can be calculated by the same impulse model as for the other IDTs and the frequency response for such an IDT is plotted in Figure 1.2(c) for an IDT of length $L_{IDT} = 500 \mu\text{m}$ and a fundamental frequency $f_1 = [200 : 250] \text{ MHz}$. The

other frequency bands are therefore at $f_2 = [400 : 500]$ MHz, $f_3 = [600 : 750]$ MHz and $f_4 = [800 : 1000]$ MHz.

All of these IDT designs were used in this work to control the frequency range used to interact with the semiconductor QDs. To contain and concentrate the surface acoustic waves, we also fabricated SAW cavities. These consist of 2 reflectors, called Bragg reflectors, and an IDT used to excite the surface acoustic wave inside the cavity and are described in the following section.

1.3 Reflective transducer: Bragg reflectors

In this section, we want to theoretically analyse the reflective behaviour of the Bragg reflectors containing the acoustic field inside the SAW resonator. These Bragg reflectors are usually made of metal electrodes with a constant width a separated by a pitch p . These electrodes are either shorted by connecting them with bus bars or in an open-circuit or floating geometry, where they are disconnected from each other. Grooves are also usually used but are not considered in this work. The Bragg reflector has a strong reflection at the Bragg frequency which occurs when the SAW wavelength is equal to $2p$. The theoretical analysis made here is based on the reflective array model (RAM). To simplify the model, we assume that there is no diffraction or waveguiding and the resistivity of the electrodes and bus bars is ignored.

1.3.1 Infinite-length grating

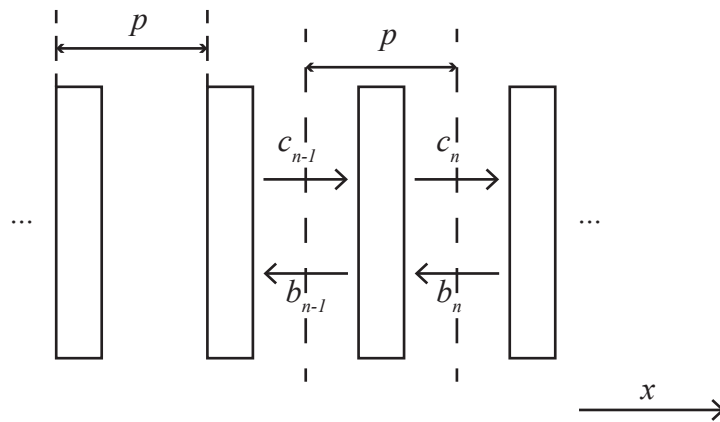


Figure 1.3: Scheme for the RAM analysis of an infinite-length grating. Reproduced from [25].

In this section, we are considering a grating of infinite length made of regular strips, electrodes, with a pitch p as shown in figure 1.3. We want to characterise this grating, its reflection and, specifically, calculate the theoretical width of its first stop band. For this purpose, we use the RAM approach which starts by considering the scattering of

the SAW wavefront (c_n and b_n) by individual strips coming from the left- and right-hand side of the strip. Each strip is described by a P-matrix. A P-matrix is a type of scattering matrix usually used to describe the behaviour of surface acoustic waves grating or transducers. This matrix relates the amplitudes of the transmitted (b_{n-1} and c_n) waves to the incident (b_n and c_{n-1}) waves. For this purpose, ports are defined as the position where the wave is measured and are often positioned close to the edge of the transducer. In this case, port 1 is placed on the left side of the electrode and port 2 on the right side. The P-matrix is then given by:

$$\begin{pmatrix} b_{n-1} \\ c_n \end{pmatrix} = \begin{bmatrix} p_{11} & p_{12} \\ p_{21} & p_{22} \end{bmatrix} \begin{pmatrix} c_{n-1} \\ b_n \end{pmatrix}$$

The coefficients of the P-matrix p_{ij} are then given by the equations below:

$$\begin{aligned} p_{11} &= r_{s1} \exp(-jkp) \\ p_{12} &= p_{21} = t_s \exp(-jkp) \\ p_{22} &= r_{s2} \exp(-jkp) \end{aligned} \tag{1.21}$$

r_{s1} and r_{s2} are the reflection coefficients for waves coming from the left and right, respectively. t_s is the transmission coefficient and k is the wavenumber of the SAW which is assumed to be real because losses are not considered in this approach. All of those coefficients refer to the centre of the strip. Due to reciprocity consideration, $p_{12} = p_{21}$ and the transmission is the same in both directions. We assume t_s to be real because a non-zero phase for t_s can be compensated by changing the value of the wavenumber k . This way, k also allows any change in the phase velocity of the SAW due to the grating so that the effective velocity is given by $v_e = \omega/k$. The coefficient t_s is taken to be positive and, since there are no losses, we obtain:

$$t_s = \sqrt{1 - |r_{s1}|^2} = \sqrt{1 - |r_{s2}|^2} > 0$$

which has for consequence that $|r_{s1}| = |r_{s2}|$ and, using power conservation, we get:

$$r_{s2} = -r_{s1}^* \tag{1.22}$$

Since the electrodes used in our experiments are symmetrical, they also behave symmetrically so that $r_{s1} = r_{s2}$. The reflection coefficients are both imaginary numbers and have therefore a phase of $\phi_r = \pm\pi/2$. The scattering by one strip can be written as:

$$\begin{aligned} b_{n-1} &= (r_{s1}c_{n-1} + t_sb_n) \exp(-jkp) \\ c_n &= (r_{s2}b_n + t_sc_{n-1}) \exp(-jkp) \end{aligned}$$

Transforming these equations to express the waves on the right as a function of the waves on the left and using the relation $r_{s1}r_{s2} = 1 - t_s^2$ gives:

$$\begin{aligned} b_n &= -(r_{s1}/t_s)c_{n-1} + (1/t_s)b_{n-1} \exp(jkp) \\ c_n &= (1/t_s)c_{n-1} \exp(-jkp) + (r_{s2}/t_s)b_{n-1} \end{aligned} \quad (1.23)$$

We now look for a grating-mode solution which is a combination of the overall wave motion constituents b_n and c_n such that:

$$\begin{aligned} b_n &= b_{n-1} \exp(-j\gamma p) \\ c_n &= c_{n-1} \exp(-j\gamma p) \end{aligned}$$

By substituting these into equations 1.23, it gives:

$$\cos(\gamma p) = \frac{\cos(kp)}{t_s} \quad (1.24)$$

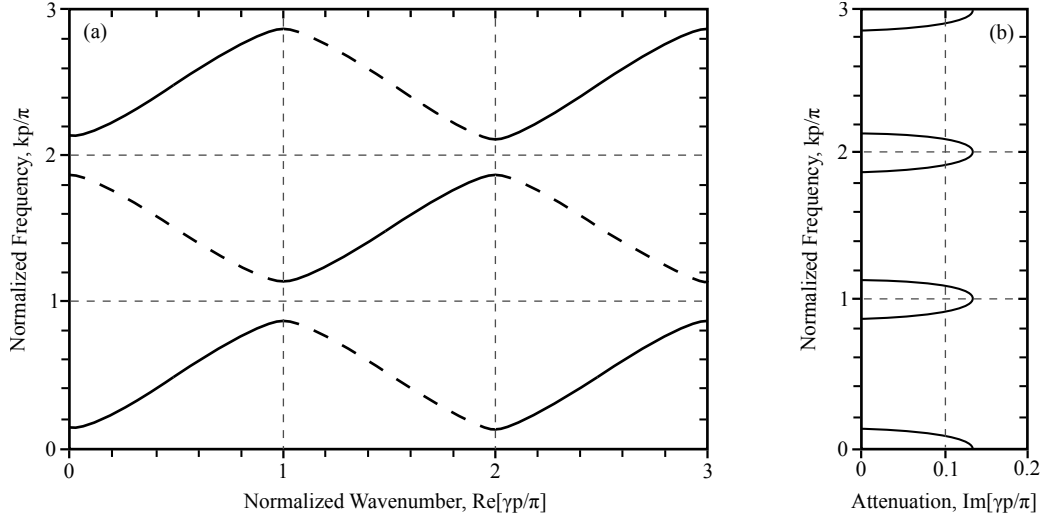


Figure 1.4: Dispersion relation between the normalized frequency kp/π and the complex normalized wavenumber $\gamma p/\pi$ for an infinite grating. Reproduced from [25].

This equation relates the normalized frequency kp/π to the complex normalized wavenumber $\gamma p/\pi$ and is plotted in Figure 1.4(a) for the real part of $\gamma p/\pi$ and in Figure 1.4(b) for its imaginary part. Since we assumed that there are no losses, k is real and so is $\cos(\gamma p)$. For most frequencies, γ is real and there is a solution with $\gamma \approx k$. Since $0 < t_s < 1$ must be respected, the right side of equation 1.24 is greater than unity when kp is near $M\pi$ which is when $p \approx M\lambda/2$, $M \in \mathbb{N}$. In that case, γ has an imaginary part and is expressed as $\gamma = M\pi/p + j\alpha$, where α is the attenuation coefficient. When kp approaches $M\pi$, the imaginary part increases and the grating presents a stop band.

This is clearly illustrated in Figure 1.4. Additionally, assuming that $v_e = \omega/k$ the effective phase velocity of the wave is independent of frequency, the stop bands all have the same width given by:

$$\frac{\Delta f}{f_{c1}} = \frac{2}{\pi} \sin^{-1}(|r_{s1}|) \approx \frac{2}{\pi} |r_{s1}| \quad (1.25)$$

where $f_{c1} = v_e/(2p)$ is the centre frequency of the first stop band, i.e. for $M = 1$. This approximation is valid for a small $|r_{s1}|$, which is the case in experiments. Additionally, in each stop band, the imaginary part of γ , α , is maximized at the centre of the stop band, so that $\cosh(\alpha p) = 1/t_s$, which gives $\alpha \approx |r_{s1}|/p$ for small $|r_{s1}|$.

1.3.2 Finite-length grating

After examining the theoretical case of an infinite-length grating, we analyse the practical case of the finite-length grating. Indeed, reflectors used in our experiments have a finite length and the definition of the P-matrix for this type of transducer will change. Here, we are considering a reflector containing N electrodes with the waves on the left characterised by the amplitudes c_0 and b_0 and the waves on the right by b_N and c_N just like for the infinite-length grating. When the reflector is perfectly reflecting, so $b_N = 0$, this result in $P_{11} = b_0/c_0$ and $P_{21} = c_N/c_0$. If the wave is only incoming, $c_0 = 0$ and we have $P_{22} = c_N/b_N$ and $P_{12} = b_0/b_N$. The P-matrix of the complete grating is found by diagonalising the P-matrix of a single strip, shown in the previous section, this gives:

$$\begin{aligned} P_{11} &= \frac{p_{11} \sin(N\gamma p)}{\sin(N\gamma p) - p_{12} \sin((N-1)\gamma p)} \\ P_{12} &= P_{21} = \frac{p_{12} \sin(\gamma p)}{\sin(N\gamma p) - p_{12} \sin((N-1)\gamma p)} \\ P_{22} &= \frac{p_{22} \sin(N\gamma p)}{\sin(N\gamma p) - p_{12} \sin((N-1)\gamma p)} \end{aligned} \quad (1.26)$$

where the p_{ij} are given by equation 1.21. The details on the calculation of the parameters P_{ij} are available in Appendix D in the book of David Morgan [25]. These parameters are dependent on the position of the ports. In this case, they are defined to be located at a distance $p/2$ from the end of the strip. In the case of a metal strips reflector with $p = \lambda/2$, it is at the edge of the reflector. By using the power conservation rule, it can be shown that:

$$\frac{1}{|P_{11}|^2} = 1 + \left| \frac{t_s}{r_{s1}} \right|^2 \frac{\sin^2(\gamma p)}{\sin^2(N\gamma p)} \quad (1.27)$$

which shows that $|P_{11}|$ cannot be larger than unity. At the centre of the first stop band, where $p = \lambda/2$, the reflection coefficient becomes:

$$|P_{11}| = \tanh(N\alpha p) \approx \tanh(N|r_{s1}|) \quad (1.28)$$

which results from equation 1.26 after some manipulation. At this frequency, P_{11} is dephased by π to r_{s1} but, taking port 1 to be situated at the centre of the first strip, results in the same phase for both quantities. In the case of a weakly reflecting grating, when $N|r_{s1}| \ll 1$, equation 1.27 transforms into:

$$|P_{11}|^2 \approx |r_{s1}|^2 \left[\frac{\sin(Nkp)}{\sin(kp)} \right]^2 \quad (1.29)$$

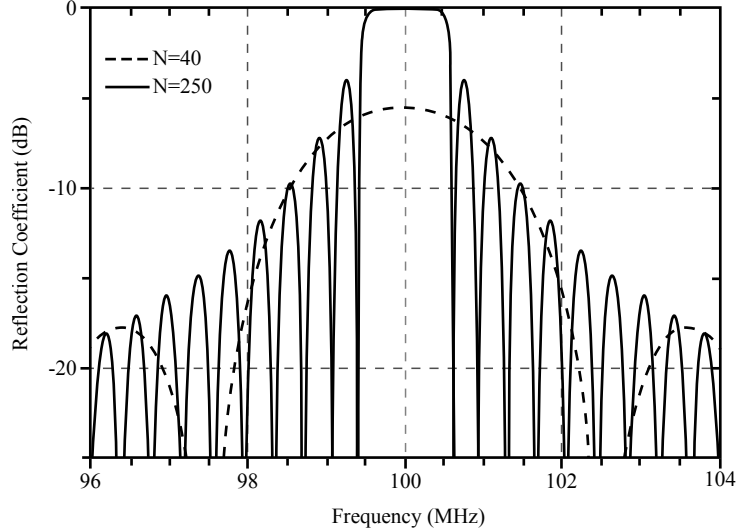


Figure 1.5: Amplitude of the reflection coefficient for two reflectors of different lengths with the number of electrodes fixed to $N = 40$ and $N = 250$ and the centre frequency to $f_c = 100$ MHz. The reflection coefficient of one electrode is taken to be $|r_s| = 0.015$. Reproduced from [25].

An example of the reflection coefficient for reflectors of different lengths is presented in figure 1.5. It shows the clear difference in the amplitude of the reflection in the middle of the stop band for both lengths. Additionally, we can see from this plot that, for a short reflector, the stop band width is dependent on the number of electrodes. However, when the number of electrodes is sufficiently high to ensure almost 100% reflection, the stop band width stays constant and is equal to the one of an infinite grating given by equation 1.25. For a strongly reflecting grating, $|P_{11}|$ reaches a value close to unity when the frequency is in the range of the stop band and it then equal to unity when $N \rightarrow \infty$.

Before the wave is completely reflected, the wave penetrates into the grating. This penetration length L_p can be calculated from the delay τ_g induced by the grating on the wave. This delay is given by $\tau_g = -d\phi/d\omega$, where ϕ is the phase of P_{11} . In the case of a semi-infinite grating, $N \rightarrow \infty$, the delay becomes $\tau_g = p/(v_e|r_{s1}|)$. From this, the penetration length is given by:

$$L_p = \frac{v_e \tau_g}{2} = \frac{p}{2|r_{s1}|} \quad (1.30)$$

and, in the case of a metallisation ratio of $a/p = 1/2$, this relation simplifies to $L_p = a/|r_{s1}|$.

1.3.3 Reflection coefficient of individual electrodes

The theoretical strips presented in the former sections are in most practical cases metal electrodes which can be short-circuited together or left floating. Grooves are also another often-used alternatives for reflective strips in resonators. In the case of metal strips, the reflection is thought to arise from two contributions: one electrical loading and one mechanical loading of the surface acoustic wave. These effects are generally small and can be added to calculate the complete reflection coefficient of one electrode. The reflection of one electrode on both sides can thus be described by:

$$r_{s1} \approx r_{s1E} + r_{s1M} \quad ; \quad r_{s2} \approx r_{s2E} + r_{s2M} \quad (1.31)$$

Both terms are determined independently when the other is assumed to be equal to zero. In the case of the electrical coefficient, the thickness h of the electrode is taken to be 0. The reflection coefficient is the same in both directions of incidence and therefore $r_{s1E} = r_{s2E} = r_{sE}$. At the centre of the first stop band, the electrical reflection coefficient is given by:

$$r_{sE} = \pm \frac{1}{2} J\pi \frac{\Delta v}{v} \left[\mp \cos \Delta + \frac{P_{1/2}(\pm \cos \Delta)}{P_{-1/2}(\pm \cos \Delta)} \right] \quad (1.32)$$

The upper signs in this equation relates to the open-circuit electrode whereas the lower signs are attributed to the short-circuit electrodes. P_ν is the Legendre function and $\Delta = \pi a/p$, where a is the width of the electrodes and p is the pitch between the electrodes. The coefficient is taken to be constant through the whole stop band due to the slow variation of its value with frequency. The coefficient is dependent on the substrate material coupling parameter $\Delta v/v$ and the metallisation ratio a/p . When $a/p = 1/2$ which is a classical design parameter, the open- and short-circuit electrodes both give $|r_{sE}| = 0.718\Delta v/v$ where the value r_{sE}/j is negative for shorted electrodes and positive for floating electrodes.

The mechanical terms r_{s1M} and r_{s2M} are dependent on the thickness of the metal film h and both the deposited metal and the substrate material and orientation. It is however independent on the electrode connection. The value of r_{s1M} is given by [28]:

$$r_{s1M} = jR_M \frac{h}{\lambda_0} \sin\left(\frac{2\pi a}{\lambda_0}\right) \quad (1.33)$$

where $\lambda_0 = 2p$ and $r_{s2M} = -r_{s1M}^*$ derives from equation 1.22. The coefficient R_M is given by:

$$R_M = -\frac{2\pi(\Delta v/v)}{\epsilon_\infty} \left[(u_1/\Phi)^2(\alpha_1 + \rho v_f^2) + (u_2/\Phi)^2(\alpha_2 + \rho v_f^2) + (u_3/\Phi)^2 \rho v_f^2 \right] \quad (1.34)$$

Material	C_1	C_2
LiNbO ₃ -128° Y-X	-2 %	+0.8
LiNbO ₃ -Y-Z	-1.7 %	-0.24

Table 1.2: Electrode reflection data for LiNbO₃-128° Y-X for shorted Al electrodes and for a metallisation. In the case of open-circuit electrodes, the sign of C_1 is reversed [25, 34, 35].

u_j are the surface displacements of the SAW on a free surface with the axes defined such that x_1 is the propagation direction and x_3 is the surface normal pointing into the vacuum. Φ is the corresponding surface potential and v_f is the free surface velocity of the wave. All these quantities can be given by a wave analysis or finite element model simulation. The constants α_1 , α_2 and ρ are the properties of the film material which is assumed to be isotropic. ρ is the density of the metal film and the constants α_i can be calculated from the Lamé constants with the following equations:

$$\alpha_1 = 4\mu \frac{\lambda + \mu}{\lambda + 2\mu} \quad (1.35)$$

$$\alpha_2 = \mu \quad (1.36)$$

In the case of Aluminium, which is used in this work, $\alpha_1 = 7.8 \cdot 10^{10} \text{ N/m}^2$, $\alpha_2 = 2.5 \cdot 10^{10} \text{ N/m}^2$ and $\rho = 2695 \text{ kg/m}^3$. Since the terms $(u_j/\phi)^2$ are real for most commonly used materials, r_{s1M} is imaginary and $r_{s2M} = r_{s1M}$. The value for aluminium electrodes on LiNbO₃-128° Y-X and LiNbO₃-Y-Z are given in table 1.2 where $r_{s1} = r_{s2} = jC_1 + JC_2h/\lambda_0$ with C_1 being the electrical component of the reflective coefficient and C_2 the mechanical one.

For most materials and cuts, the mechanical component of the reflection coefficient is in phase with the electrical component for shorted electrodes. One of the exceptions is LiNbO₃-128° Y-X where the components are in phase only for floating electrodes. In this case, reflectors are more efficient in their reflection for disconnected electrodes.

1.4 One-port resonator

One-port resonators are made of two reflectors, either shortened or floating, and an IDT exciting the acoustic field inside the cavity defined by the reflectors. The general geometry of such a resonator is displayed in Figure 1.6, where the important design parameters are defined. L_p is the penetration length inside the reflectors, Δ is the distance between the centre of the first electrode of each reflector and d is the distance between the edges of the reflectors which is the length which was used to define the resonators design in our fabrication. In our case, we consider symmetrical electrodes with a metallisation ratio of $a/p = 1/2$ so that $a = \lambda_0/4$. In this case, the reflection coefficients for waves incident from both directions are the same and we have $r_{s1} = r_{s2} = r_s$ and $\Delta = d + \lambda_0/4$.

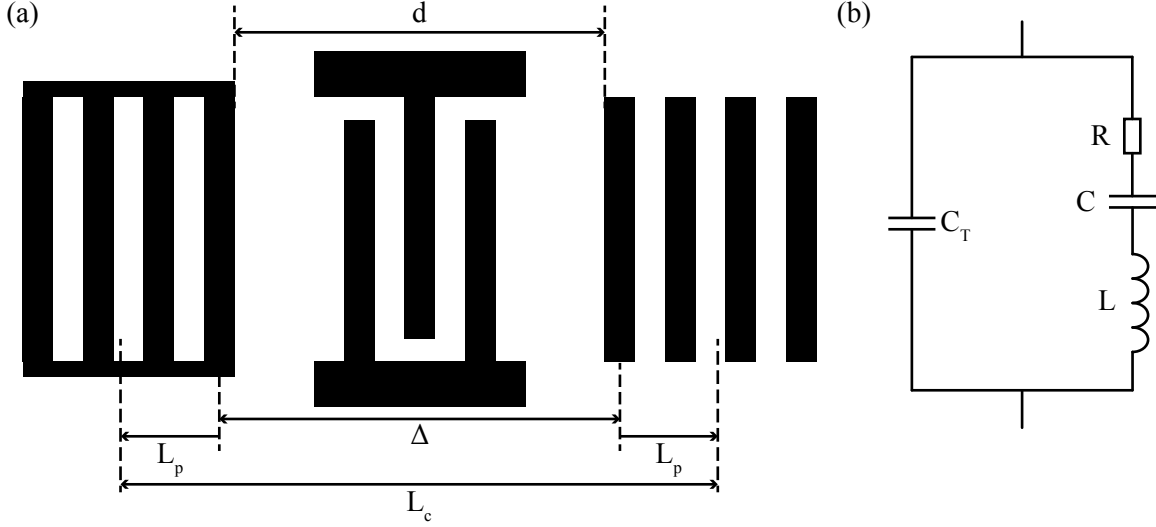


Figure 1.6: (a) Geometry of a one-port resonator containing the IDTs and the two reflectors. The different important design parameters are displayed in the scheme such as the distance between the reflectors Δ and d , L_p the penetration length inside the resonator and L_c the effective length of the cavity. (b) RLC circuit model of the resonator at resonance, i.e. for $f = f_c$.

As derived before, the reflectors are reflecting the surface acoustic wave in a frequency range given by Equation 1.25 with a centre frequency $f_c = 2v_e/p$ given by the pitch of the reflectors. Additionally, only the SAWs which respect the resonance condition defined by the cavity length will build inside the cavity and form standing waves. For the other frequencies, the waves are dampened by destructive interferences. This resonant condition is respected when the phase change of the SAW for a cavity round trip is equal to an integer multiple of π . This phase change for this cavity round trip is given by $2\phi - 2\omega\Delta/v_e$, where ϕ is the phase of P_{11} , the reflection of the gratings. Since $\omega/v_e = 2\pi/\lambda$ and the phase of P_{11} is equal to the phase of the reflection coefficient of one electrode, i.e. $\phi = \phi_r = \pm\pi/2$, we obtain:

$$2\phi - 2\omega\Delta/v_e = n \cdot 2\pi \Leftrightarrow \Delta = (n \pm 1/2) \cdot \lambda/2 \quad (1.37)$$

where $n \in \mathbb{N}$. From this relation, we can fix the distance between the reflectors to $d = n \cdot \lambda_0/2$ where $\lambda_0 = 2p$ is the wavelength of the centre frequency of the reflectors stop band. The spacing between the resonant modes or free spectral range (FSR) is simply given by:

$$FSR = \frac{v_e}{2L_c} = \frac{v_e}{2(\Delta + 2L_p)} = \frac{v_e}{2(\Delta + \frac{p}{|r_{s1}|})} \quad (1.38)$$

When the FSR is larger than the width of the reflectors' stop band, i.e. when the cavity is small enough, the resonator presents only one resonant mode. On the other

hand, multiple modes can be achieved when the size of the cavity increases, reducing the FSR to a value lower than the width of the reflectors' stop band.

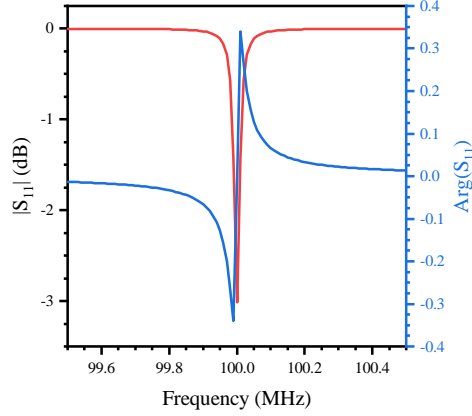


Figure 1.7: Plot of the magnitude and phase of the complex function of the scattering parameter S_{11} for one mode of a SAW resonator with a centre frequency $f_0 = 100$ MHz, an internal quality factor Q_i of 5000 and an external quality factor Q_e of 15000.

In addition to the resonant cavity, an IDT is added inside the resonator to excite the surface acoustic wave. The IDT also enables an electrical measurement of the phononic mode of the resonator and the excitation of the surface acoustic wave inside the cavity. The behaviour of the resonator can be modelled by a resonant RLC circuit. This model circuit is schematically depicted in Figure 1.6(b). C_T is the transducer capacitance and the other electrical elements, the resistor R , the capacitance C and the inductance L , model the electrical behaviour of the SAW resonator. This electrical model is based on an analysis of the impedance of the transducer inside such a SAW resonator. The details of this analysis are available in Chapter 11 of the book of David Morgan [25] and in Chapter 10 of the book of Supriyo Datta [28]. The drawbacks of this model is that it is only valid for one mode and in a range of frequencies close to the centre frequency of this mode. When the resonator presents multiple modes, the model can be expanded by multiple resonant branches in the equivalent circuit, which are connected in parallel with each other. This equivalent circuit model is still a good tool to calculate the quality factor of the cavity, especially the unloaded or internal quality factor Q_i of the cavity. This factor characterises the quality of the SAW cavity outside of the influence of the external circuit.

In this work, we used a vector network analyser measuring the reflective scattering parameter S_{11} to characterise the SAW resonator. Using the RLC equivalent circuit model presented here, each resonant mode is fitted by the following complex equation established by Manenti and coworkers [6, 7]:

$$S_{11}(f) = \frac{(Q_e - Q_{i,n})/Q_e + 2iQ_{i,n} \cdot (f - f_{0,n})/f}{(Q_e + Q_{i,n})/Q_e + 2iQ_{i,n} \cdot (f - f_{0,n})/f} \quad (1.39)$$

where $Q_{i,n}$ and $Q_{e,n}$ denote the internal and external quality factor of mode n and its coupling to the external circuit, respectively. $f_{0,n}$ is the resonance frequency of the n -th

mode. The magnitude and phase of the complex function is plotted in Figure 1.7 for a resonator mode with a centre frequency $f_0 = 100$ MHz, an internal quality factor Q_i of 5000 and an external quality factor Q_e of 15000. The complex function shows the typical shape expected for the electrical reflection of a resonator. The magnitude (red) dips strongly at the centre frequency and the phase (blue) shows a pronounced jump at the centre frequency.

Quantum Dots Optomechanics

In this chapter, the basic optical properties of semiconductor quantum dots (QDs) as well as their interactions with surface acoustic waves are described. Additionally, the experimental setups used to quantify the SAW modulation of the QD's emission are described.

2.1 Semiconductor quantum dots

Semiconductor quantum dots are based on the confinement of charge carriers in 3 dimensions on length scales close to their De Broglie wavelength. This results in the formation of discrete energy states and therefore sharp emission lines for optical transitions between those states. This confinement can be achieved by combining optically active semiconductors with different bandgap energies E_g . In this section, we discuss the basic properties of the material system used as well as the theory behind the quantum confinement and its effect on the optical properties of the quantum dot system. The experimental fabrication of semiconductor quantum dots, on the other hand, is described in Chapter 3. This section is based on the books by Mark Fox and by Oliver Gywat, Hubert Krenner and Jesse Berezovsky [36, 37, 38]. The theory is only explained briefly and, for more details, the reader may refer to these books.

2.1.1 Fundamentals of semiconductor

For the fabrication of the semiconductor heterostructures and the QDs studied in this work, two parameters are of utmost importance: the lattice constant c and the bandgap energy E_g of the semiconductor crystal. For this reason, the material systems used predominantly to fabricate QDs are GaAs, AlAs, InAs and their ternary alloys $\text{Al}_x\text{Ga}_{(1-x)}\text{As}$ and $\text{In}_x\text{Ga}_{(1-x)}\text{As}$. This material system enables the tuning of both the lattice constant and the energy bandgap of the semiconductor by just adjusting the composition x of the semiconductors. These alloys are called III-V semiconductors and crystallise in a zinc-blende crystal structure. This structure consists of two face-centred cubic (fcc) lattices, one made entirely of group III atoms and the other of group V atoms, and

shifted by $1/4c$ with respect to each other in all three spatial dimensions, c being the lattice constant.

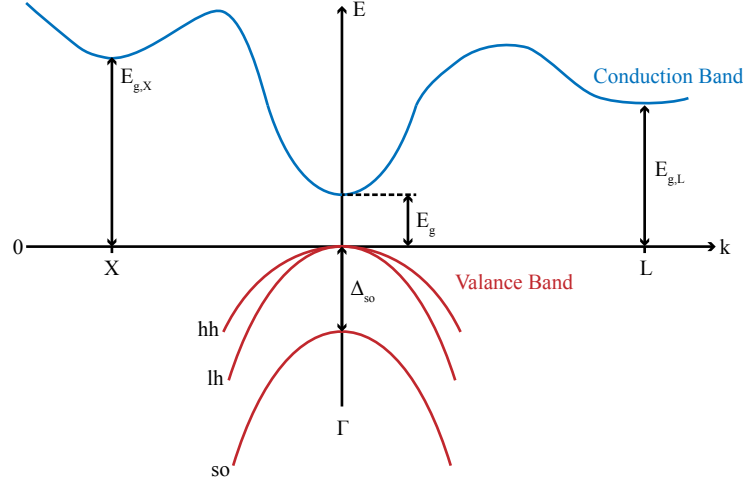


Figure 2.1: Schematic of the band structure of GaAs around the Γ point, adapted from [36, 33].

A schematic of the band structure of GaAs around the Γ point of the Brillouin zone is displayed in Figure 2.1. At $T = 0$ K, the valence band is the last band located below the Fermi level and thus is fully occupied. The conduction band is free of electrons and is located above this level. Both bands are separated by a region where no charge carriers are allowed, the so-called bandgap E_g . In the case of GaAs, there are three minima in the conduction band at the X-, L- and Γ -point and therefore three bandgap energies can be identified: $E_{g,X}$, $E_{g,L}$ and $E_{g,\Gamma}$. The smallest bandgap is the one situated at the Γ -point where the electron wave vector $\mathbf{k} = (0, 0, 0)$, where the minimum of the conduction band coincides with the maximum of the valence band. This property makes GaAs a direct bandgap semiconductor which has a large impact of the optical properties of the semiconductor. The direct bandgap enables efficient optical transitions between the valence band, originating from the p-bonding molecular orbitals, and the conduction band, originating from the s-antibonding molecular orbitals, at the Γ -point. An electron, e^- , can thus be excited by a photon with an energy $\hbar\omega_{ph} \geq E_g$ to the conduction band and further relaxes to the minimum of the band. It leaves behind a hole, h^+ , inside the valence band which relaxes to the maximum of the valence band. This electron-hole pair can then recombine spontaneously by emitting a photon, provided that they are at the same position in real- and k -space. Indeed, the optical transitions in k -space are vertical due to the quasi-null impulse of photons. This full process is referred to as a photoluminescence (PL) process and is the major spectroscopy technique employed in this work.

As can be seen in Figure 2.1, different bands can be approximated using a parabolic

function around the Γ -point:

$$E(k) = E_0 + \frac{\hbar^2 k^2}{2m^*} \quad (2.1)$$

where m^* is the effective mass of the charge carrier and describes the inverse of the band curvature:

$$m^* = \hbar \left(\frac{d^2 E}{dk^2} \right)^{-1} \quad (2.2)$$

This approximation enables the description of the charge carrier motion as the movement of a free particle in vacuum with a modified mass, m^* .

As shown in Figure 2.1, the valance band consists in three different bands. Two of them are degenerated at the Γ -point and are called the heavy hole (hh) and light hole bands (lh). They have different curvatures, which leads to this difference in effective mass and therefore in their name. The third band is split-off to lower energy by the spin-orbit coupling (Δ_{so}) and is referred as the split-off band. In the case of GaAs, the split-off energy Δ_{so} is large enough so that this band can be ignored for most optical properties considerations ($\Delta_{so} = 340$ meV [39]).

When an electron-hole pair is photogenerated in the semiconductor at low temperature, the attractive Coulomb forces between the two charge carriers can result in the formation of a bound state called exciton. The exciton can be described by a simple hydrogen model and the bonding energy between both charge carriers can be given by:

$$E_X = \frac{e^4 \mu}{32\pi^2 \hbar^2 \epsilon^2} \approx 4.2 \text{ meV} \quad (2.3)$$

where μ is the effective reduced mass of the exciton, $\mu = \left(\frac{1}{m_e^*} + \frac{1}{m_h^*} \right)^{-1}$, and ϵ is the dielectric constant of the material ($\epsilon = 13.1 \cdot \epsilon_0$ for GaAs). The number presented here is in good agreement with the value observed in experiments for GaAs [40]. The radius, r_X of the theoretical hydrogen model or spatial extent of the exciton can be calculated by:

$$r_X = \frac{4\pi \hbar^2 \epsilon}{\mu e^2} \approx 13 \text{ nm} \quad (2.4)$$

Confining the exciton on the length scale of this radius will lead to a quantum confinement and the formation of discrete, quantized energy levels. This quantum confinement is used to create quantum dots where the confinement is present in all three spatial directions. The fabrication of semiconductor heterostructures using materials with different bandgap energies is the method used here to create such confinement potentials for both electrons and holes. As mentioned previously, this is why GaAs,

	GaAs	AlAs	InAs
E_g^Γ	1.519 eV	3.099 eV	0.417 eV
E_g^L	1.815 eV	2.46 eV	1.133 eV
E_g^Γ	1.981 eV	2.24 eV	1.433 eV

Table 2.1: Bandgap energies for GaAs, AlAs and InAs at the three high symmetry points, X, L and Γ , in k -space [41].

	$\text{Al}_x\text{Ga}_{(1-x)}\text{As}$	$\text{In}_x\text{Ga}_{(1-x)}\text{As}$
E_g^Γ	$(-0.127 + 1.31 x)$ eV	0.477 eV
E_g^L	0 eV	0.33 eV
E_g^Γ	0.055 eV	1.4 eV

Table 2.2: Bowing parameter C for the ternary alloys $\text{Al}_x\text{Ga}_{(1-x)}\text{As}$ and $\text{In}_x\text{Ga}_{(1-x)}\text{As}$ [41].

InAs and AlAs as well as their ternary alloys are used. The bandgaps of all three materials at the X-, L- and Γ -points are summarised in Table 2.1.

In the case of the ternary alloys employed to fabricate the heterostructures (A_{1-x}B_x), the dependence of the bandgap on the alloy composition x is described by a quadratic formula [42]:

$$E_g(\text{A}_{1-x}\text{B}_x) = (1 - x)E_g(\text{A}) + xE_g(\text{B}) - x(1 - x)C \quad (2.5)$$

where C , called the bowing parameter, accounts for the deviation from a linear interpolation between $E_g(\text{A})$ and $E_g(\text{B})$. For the alloys $\text{Al}_x\text{Ga}_{(1-x)}\text{As}$ and $\text{In}_x\text{Ga}_{(1-x)}\text{As}$, the bowing parameters C for each bandgap are summarised in Table 2.2.

One important property of $\text{Al}_x\text{Ga}_{(1-x)}\text{As}$ is the transition from a direct semiconductor to an indirect semiconductor at a composition around $x = 0.4$ due to the different slopes in the increase of the bandgap energies. In addition to the bandgap energy, an important parameter for the fabrication of heterostructures is the lattice constant c of the crystal. This lattice constant also changes with the composition of the ternary alloy and can be simply approximated by a linear interpolation between the two lattice constants of the full binary materials [41, 43]:

$$c(\text{Al}_x\text{Ga}_{(1-x)}\text{As}) = (5.6533 + 0.0078 \cdot x) \text{ \AA} \quad (2.6)$$

$$c(\text{In}_x\text{Ga}_{(1-x)}\text{As}) = (5.6533 + 0.405 \cdot x) \text{ \AA} \quad (2.7)$$

Due to the relatively small increase of the lattice constant for $\text{Al}_x\text{Ga}_{(1-x)}\text{As}$ when going from GaAs to AlAs, both materials can be grown epitaxially as continuous films on top of each other. On the other hand, the growth of thick layer of InAs on top of GaAs is not possible due to the large ($\approx 7\%$) difference in lattice constant. It is

however used as the driving force for the fabrication of self-assembled quantum dots, as explained later in Chapter 3.

2.1.2 Semiconductor heterostructures: quantum dot properties

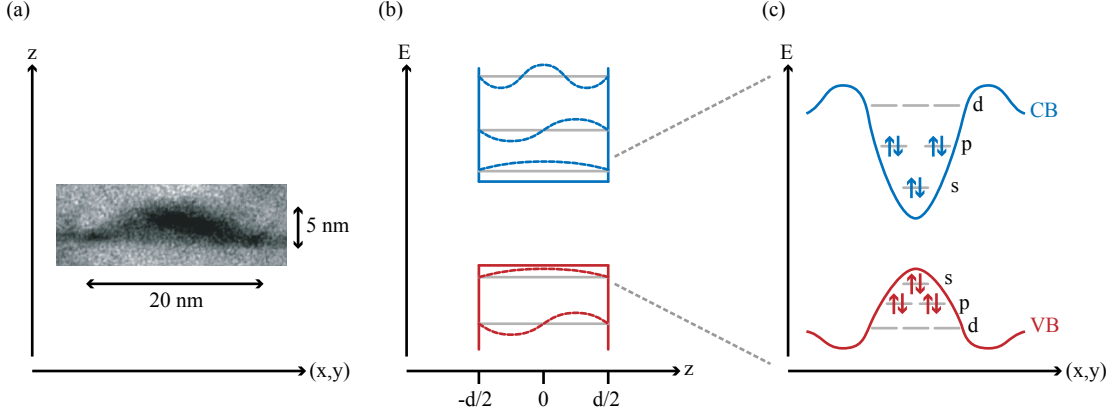


Figure 2.2: (a) Transmission electron microscope image of an $\text{In}_x\text{Ga}_{(1-x)}\text{As}$ QD imbedded in a GaAs matrix, adapted from [44]. (b) Schematic of the confinement in the z -direction which can be described as an infinite potential well. (c) Schematic of the band structure of the QD due to the confinement in the (x,y) -direction which results in discrete states for the electron and holes, adapted from [38, 33].

In this section, the optical properties of QDs will be discussed whereas the practical growth of semiconductor QDs will be addressed in Chapter 3. To create a quantum dot, a small island of a material with a lower bandgap energy is embedded in a matrix made of a semiconductor with a larger bandgap energy. In Figure 2.2(a) a transmission electron micrograph of an $\text{In}(\text{Ga})\text{As}$ -QD embedded in a GaAs matrix is presented. This image shows that the typical shape of such a QD is a flat island with a dimension in the z -direction around three to four times smaller than the dimensions in the (x,y) -plane (5 nm to 20 nm in the (x,y) -direction). This asymmetry in the shape of the QD has an impact on the quantum confinement of the electrons and holes inside the QD. In the z -direction, the QD can be approximated by an infinite potential well of width d , as shown in Figure 2.2(b) for the conduction and valence band of the heterostructure:

$$V_z = \begin{cases} \infty, & \text{for } |z| \geq d/2 \\ 0, & \text{for } |z| < d/2 \end{cases} \quad (2.8)$$

The solution to such a well-known quantum confinement problem are discrete energy levels in the direction of the confinement described by the following equation:

$$E_z^{e,h} = \frac{\hbar^2 \pi^2 n_z^2}{2m_{e,h} d^2} \quad (2.9)$$

The spacing between the energy levels $E_z^{e,h}$ increases with the quantum number $n_z = 1, 2, 3, \dots$ and with decreasing width d . If the system is not confined in the (x,y)-plane, this type of heterostructure is called a quantum well (QW). Charges carriers present in a QW still have continuous energy bands and their motion is still continuous in the (x,y)-direction but the energy levels are split in subbands determined by the quantum number n_z . This infinite potential approximation is a strong simplification but still gives us the same quadratic dependence on the distance d as the QD does on its height. As the confinement in the z-direction is much stronger than the one in the x- and y-directions, the only levels which are taken into account are the lowest energy levels with $n_z = 1$. The weaker confinement in the (x,y)-plane can be described by a harmonic oscillator potential:

$$V_{x,y} = \frac{1}{2}m^*(\omega_x^2x^2 + \omega_y^2y^2) \quad (2.10)$$

and, assuming that the potential has a radial symmetry, $\omega = \omega_x = \omega_y$, the energy levels can be determined by:

$$E_{x,y}^{e,h} = \hbar\omega(n_x + n_y + 1) \quad (2.11)$$

with the quantum numbers $n_x, n_y = 0, 1, 2, 3, \dots$ for both spatial directions. The total energy of a specific state is therefore given by the sum of both quantum numbers, $l = n_x + n_y$, and the atomic nomenclature is typically used to label the energy levels with s-, p-, d-,... shells for the quantum number $l = 0, 1, 2, \dots$. The different energy levels in the parabolic potential are schematically shown in Figure 2.2(c). It is clear that, except for the lowest shell ($l = 0$), the energy levels are degenerated since different combinations of the quantum numbers n_x and n_y give the same value for the quantum number l . Each state can then be populated by two electrons of opposite spin. Additionally, the parabolic nature of the potential causes the energy levels or shells to be equally spaced. In this work, only the optical transitions between the two s-shells are considered and the higher energy levels are neglected. We are therefore considering the QD as a two-level system which makes it an interesting structure for quantum computing. The same photoluminescence phenomenon as in the direct semiconductor bandgap can be observed in a QD. In this case, an electron-hole pair or exciton can be photogenerated by a laser with a energy above the bandgap and the electron and holes relaxes to their respective most energetically favourable levels by dissipating phonons in the crystal. The electron and holes can then recombine through the emission of a photon. This photon can then be collected and detected as a function of their energy and a PL spectrum can be obtained. Such a spectrum is plotted in Figure 2.3 and shows a series of sharp emission lines, originating from several QDs.

The emission energy depends on two important parameters: the energy difference between the two s-shells in the conduction and valance bands of the QD and on the occupancy state of these s-shells. The energy difference E_{trans} between the two transition states is given by the sum of the bandgap E_g of the material the QD is made of

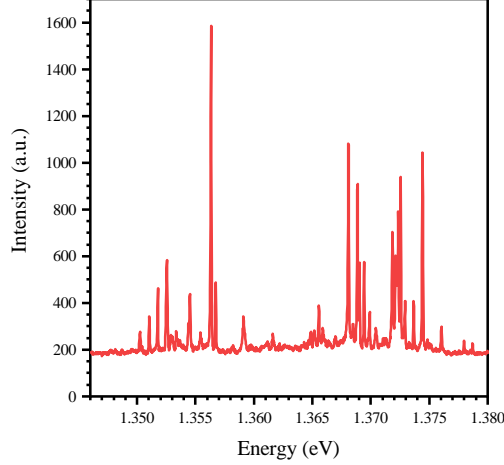


Figure 2.3: PL spectrum of a sample containing QDs showing the sharp emission lines attributed to several QDs.

and the confinement energies $E_z^{e,h}(n_z = 1)$ and $E_{x,y}^{e,h}(l = 0)$ for the electron and holes respectively:

$$E_{trans} = E_g + E_z^e(n_z = 1) + E_z^h(n_z = 1) + E_{x,y}^e(l = 0) + E_{x,y}^h(l = 0) = E^e + E^h \quad (2.12)$$

Since this energy is dependent on the confinement in all three spatial directions, it is especially sensitive to the size and shape of the QD. When QDs are fabricated, see Chapter 3, their size is statistically distributed which explains the appearance of many lines inside the PL spectrum. The size distribution and therefore the emission energy distribution can be controlled by the growth conditions. Most importantly, the density of the QDs can also be controlled so that a laser focussed to a point of $\approx 1 \mu\text{m}^2$ can be used to excite QDs and the emission of single QDs can be collected. This technique is called μ -PL and is presented in the following sections. In addition to the confinement energies, the emission energy is dependent on the occupation state of the energy levels as the Coulomb interaction between the charge carriers inside the s-shell has to be taken into account. This energy shift due to the Coulomb interaction is dependent on the number of electrons and holes present in the s-shell. The four optically active occupancy states, or excitonic states, are schematically depicted in Figure 2.4.

Each of these occupancy state is optically active and is referred to as an exciton. The neutral exciton X^0 contains one electron and one hole. The charged excitons X^- and X^+ each contain an additional electron or hole, respectively. Finally, the neutral biexciton $2X^0$ has both s-shells fully filled with two electrons and holes. The absolute energy of one of these excitonic states is then given by the confinement energy of the electron E^e and holes E^h and the Coulomb interaction for all the possible interactions between the two types of charge carriers. As a result, the energies for all these occupancy states are given by:

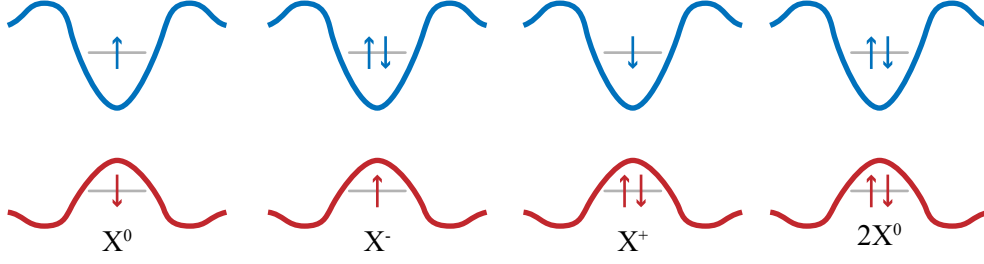


Figure 2.4: The four possible types of optically active occupancy states of the s-shell. The neutral exciton X^0 contains one electron and one hole. The charged excitons X^- and X^+ contain an additional electron or hole. For the neutral biexciton $2X^0$, both s-shells are fully filled with two electrons and holes, respectively.

$$E_{X^0} = E^e + E^h - V^{eh} \quad (2.13)$$

$$E_{X^-} = 2E^e + E^h - 2V^{eh} + V^{ee} \quad (2.14)$$

$$E_{X^+} = E^e + 2E^h - 2V^{eh} + V^{hh} \quad (2.15)$$

$$E_{2X^0} = 2E^e + 2E^h - 4V^{eh} + V^{ee} + V^{hh} \quad (2.16)$$

The attractive force between different charge carriers V^{eh} reduces the total energy whereas the repulsive interaction between two electrons V^{ee} and between two holes V^{hh} increases the total energy. The emitted photon energy is given by the energetic difference between the initial and final state of the optical transition, which thus gives for each excitonic states:

$$\Delta E_{X^0} = E^e + E^h - V^{eh} \quad (2.17)$$

$$\Delta E_{X^-} = E^e + E^h - 2V^{eh} + V^{ee} \quad (2.18)$$

$$\Delta E_{X^+} = E^e + E^h - 2V^{eh} + V^{hh} \quad (2.19)$$

$$\Delta E_{2X^0} = E^e + E^h - 3V^{eh} + V^{ee} + V^{hh} \quad (2.20)$$

Since the attractive and repulsive forces due to the Coulomb interactions are not generally equal, the different emission energies are therefore not identical. The emission of a QD is thus split into discrete lines, which makes it possible to address a specific transition of a single QD. Typical splittings are in the order of several meV, depending on the interaction terms V^{xx} . The exact ordering of each emission energy strongly depends on the geometry of the respective quantum dots and can vary from system to system. Since the electron is usually less localised than the hole wave function, the following ordering is often found: $V^{ee} < V^{eh} < V^{hh}$. Therefore, the X^+ emission is shifted towards higher energies with respect to the neutral exciton X^0 and the X^- is shifted towards lower energies. The energy shift $(\Delta E_{X^0} - \Delta E_{2X^0})$ between the neutral exciton and the biexciton is called the biexciton binding energy and was often observed

to be positive, meaning the biexciton emission is shifted towards lower energies. These tendencies are confirmed by the experimental PL measurement of two QDs presented in Figure 2.5. In this work, we analysed only individual emission lines and the identification of the occupancy state at the origin of this emission line was not considered as it does not change the mechanical interaction of the phonon and the exciton.

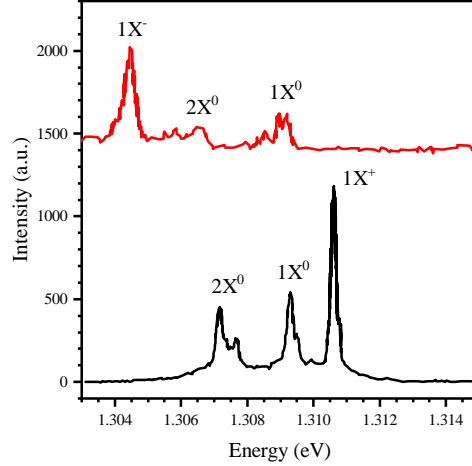


Figure 2.5: μ -PL spectrum of two QDs showing the different emission energies of the excitonic states, reproduced from [32].

2.2 Interfacing quantum dots with surface acoustic waves: deformation potential coupling

The surface acoustic waves excited on a sample consist of an electrical and mechanical fields which both interact with the QD's energy states. In this work, our analysis focusses mostly on the influence of the mechanical field on the QD's emission. In this section, we will first summarize briefly how the electrical field of the SAW can be used to manipulate the state of the QD and then explain the mechanical influence on the QD's emission through the deformation potential coupling. A more detailed description of the different influences of both the electrical and mechanical fields on the QD is available in the review paper by Weiß and Krenner [13].

The main component of the electric field influence is SAW induced spatio-temporal carrier dynamics (STCDs). In semiconductors, the SAW's piezoelectric potential is superimposed onto the band structure which results in a type-II band edge modulation. This modulation generates stable points for electrons and holes in the conduction and valence bands, respectively, that are spatially separated. Rocke and coworkers demonstrated the ionisation of photogenerated excitons inside a quantum well due to the type-II band modulation by the piezoelectric field accompanying the surface acoustic wave [45, 46]. Those ionized excitons can then be transported by the SAW along its propagation direction in the plane of the quantum well over large distances. For QDs connected to a continuous 2D system or wetting layer, this phenomenon can be used to

dynamically regulates the carrier injection into the QD which acts as a local deep trap for electrons and holes in the quantum well band structure [14, 15]. Furthermore, this acoustic transportation can be used to generate carrier inside the 2D continuum and to acoustically pump a single-photon source [47, 48]. The SAW electric field can also be used to control the occupancy of the QDs. Depending on the polarisation of the electric field at the position of the QD during the acoustic cycle, a certain charge carrier species is predominantly injected into the quantum emitter, influencing the occupancy state that is formed [14, 16, 17]. Additionally, by controlling the timing of the optical excitation of the QD during the acoustic cycle, the emission of the QD can be switched between a charged and a neutral exciton [18].

The electric field can also influence the emission energy of the QD through the quantum confined stark effect (QCSE), which is based on the polarisation of excitons in a quantum system [49]. The energy shift in the QD's emission by the QCSE is given by:

$$\Delta E_{QCSE} = -\beta \mathbf{F}^2 \quad (2.21)$$

where β is the polarisability of the exciton inside the quantum system. The quadratic dependence of the energy shift on the electric field means that the spectral modulation of the QD's emission has twice the frequency of the SAW inducing it and increases quadratically with the amplitude of the SAW. Due to these properties, this effect can be easily distinguished from the mechanical influence of the SAW.

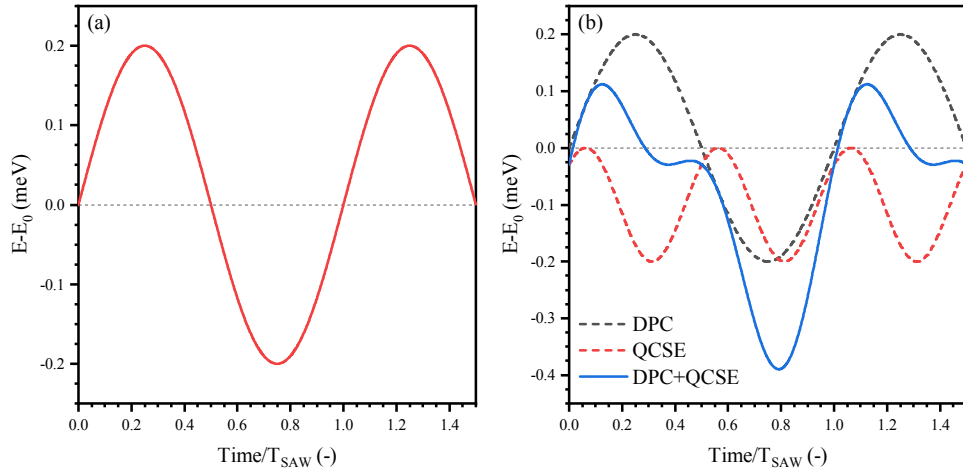


Figure 2.6: Theoretical depiction of the modulation of the QD's emission energy due to the SAW through: (a) deformation potential coupling (DPC) and (b) the combination of the deformation potential coupling (DPC) and the quantum confinement stark effect (QCSE).

The acousto-optic spectral control of the QD's emission studied in this work is based on the deformation potential coupling. In this case, the strain associated to the wave changes the lattice constant of the crystal and thus modulates the bandgap energy E_g

of the semiconductor. A compressive strain decreases the lattice constant which leads to an increase in the bandgap energy whereas a tensile strain decreases the bandgap energy. This effect, called deformation potential coupling, is directly proportional to the local hydrostatic pressure. A SAW is characterised by a dynamic pressure field $p(x, t) = p_0 \cdot \sin(\omega_{SAW}t + kx)$, which induces a type-I band edge modulation. The dynamic energy shift of the bandgap due to the SAW can then be characterised by:

$$\Delta E(x, t) = \frac{dE_{gap}}{dp} \cdot p(x, t) = \frac{dE_{gap}}{dp} \cdot p_0 \cdot \sin(\omega_{SAW}t + kx) \quad (2.22)$$

where $\frac{dE_{gap}}{dp}$ is the strength of the deformation potential coupling. This parameter is solely dependent on the material of the quantum emitter and in the case of GaAs, this parameter is equal to $\frac{dE_{gap}}{dp} = 115 \mu\text{eV MPa}^{-1}$ [50]. Since the transition energy of the QDs is directly related to the bandgap energy of the semiconductor, the same energy modulation can be observed for the discrete QD's emission line [19, 24, 21, 51]. Therefore, the modulation of the QD's emission follows the SAW frequency and is linearly proportional to the SAW amplitude. In Figure 2.6(a), the sole modulation of the QD's emission through the deformation potential coupling is plotted and follows the simple sinusoidal function of the SAW. When the quantum confinement stark effect is added, the quadratic dependence of the modulation on the SAW amplitude can be seen as presented in Figure 2.6(b). In addition to the DPC sinusoidal modulation, the QCSE adds a continuous offset towards lower energies and a sinusoidal modulation with the double SAW frequency. The phase difference between the QCSE and DPC modulations depends on the material system and the position of the QD. These characteristics makes it easier to see the influence of the electrical field on the QD's emission compared to a simple mechanical modulation. In this work, the influence of the electric field is considered to be negligible due to the palladium layer present below the QD membrane in the experiment which short-circuits the electric field coming from the LiNbO_3 substrate. Additionally, the experiments conducted in Chapter 6 without the presence of the palladium layer don't show any indication that the QD's emission is influenced by the presence of an electric field which confirms that the main modulation is introduced by the mechanical field of the SAW.

2.3 Optical and electrical measurement setup

To measure the SAW modulation of the QD's emission by the deformation potential coupling, two main measurement schemes are used in this work: time-integrated and time-resolved spectroscopy. The measurement setup used in this thesis are presented here as well as the typical measured signal.

2.3.1 Time-integrated spectroscopy

Our setup to measure the influence of the deformation potential coupling of the surface acoustic wave on the QDs using stroboscopic μ -PL spectroscopy is depicted schematically in Figure 2.7. The measurement setup is separated in three main parts: the

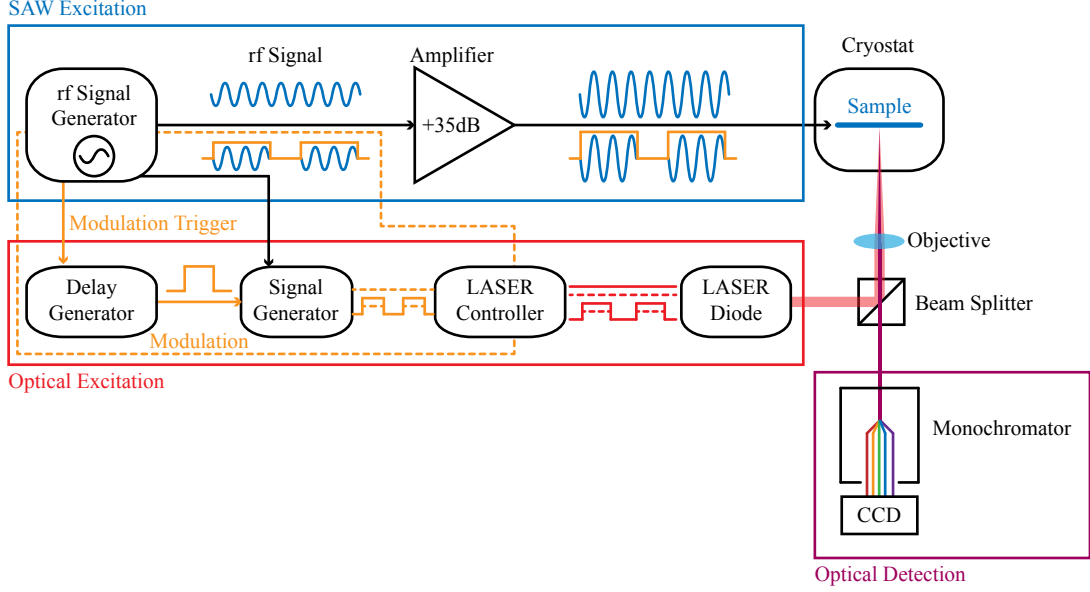


Figure 2.7: Schematic of the time-integrated measurement setup. The SAW excitation part of the setup is indicated in blue, the optical excitation in red. The modulation of both signals which can be implemented is indicated in the dashed orange box. The optical detection of the setup is indicated in purple.

SAW excitation (blue rectangle), the optical excitation (red rectangle) and the optical detection (purple rectangle), which all converge around the cryostat containing the sample and operate independently. Additionally, the SAW signal and the laser signal can be modulated (orange dashed rectangle) and both signals are synchronised so that both excitations are applied simultaneously at the QD. The SAW excitation starts with the generation of the rf signal by a signal generator (*Stanford Research Systems*, SG382, SG384 or *Rohde & Schwarz*, SME03) which fixes the frequency of the SAW f_{rf} and the initial amplitude of the signal P_{rf} . This signal can be amplified using an rf amplifier (*Mini-Circuits*, ZHL-42W+, ZHL-42W or ZHL-2010+) for the experiments which require higher amplitudes, which is the case in this work. The amplified signal is then applied to the IDTs on the sample through the rf wiring of the cryostat. The optical excitation is provided by a diode laser emitting light with a wavelength of either $\lambda_{laser} = 660$ nm (*PicoQuant*, LDH-D-C-660) or $\lambda_{laser} = 833$ nm (*PicoQuant*, LDH-D-C-840) depending on the type of QDs which are investigated. The diode laser are controlled using a laser driver unit (*PicoQuant*, PDL 800-B or PDL 800-D) which fixes the laser current and therefore the optical power output (P_{laser}). The driver unit can operate the laser in continuous wave (cw) or pulsed mode. In the pulsed mode, the laser diode will emit light pulses with a minimum length of $\tau_{laser} \approx 70$ ps for $\lambda_{laser} = 660$ nm and $\tau_{laser} \approx 95$ ps for $\lambda_{laser} = 833$ nm, respectively. The repetition frequency of the laser f_{laser} can be fixed either by an external source, indicated by the signal generator in Figure 2.7 (*Stanford Research Systems*, CG635 or *Agilent* 33250A), sending a trigger to the laser controller or by one of the two internal frequency oscilla-

tors present in the laser controller. The stroboscopic excitation of the QD during the acoustic cycle can be phase averaged by using the cw mode, the internal frequency oscillator or by using a laser frequency non-commensurable with the frequency of the SAW, $f_{laser} \neq \frac{f_{rf}}{n}$, $n = 1, 2, 3, \dots$. Another possibility is the phase-locking of the pulsed laser excitation with the SAW. In that case, the SAW frequency is set to an integer multiple of the laser frequency, $f_{laser} = \frac{f_{rf}}{n}$, $n = 1, 2, 3, \dots$, and both signal generators are locked to the same reference oscillator. The QD is therefore always excited at the same time during the SAW acoustic cycle which can be controlled by changing the relative phase between the SAW signal generator and the laser signal generator. This stroboscopic phase-locked measurement enables the measurement of the QD modulation at different times during the acoustic cycle. The optical detection part is composed of a monochromator spectrally dispersing the emitted signal. The monochromator has a focal length of either 0.5 m or 0.75 m, depending on the measuring setup (*Princeton Instruments*, SP-2750, *Acton Research Corporation*, SpectraPro 2500i or *Andor*, SR-500i). The dispersed optical signal is then detected by an liquid nitrogen or thermoelectrically cooled charge coupled device (*Princeton Instruments*, Spec-10 or *Andor*, iDus 416) which acquires a time-integrated multichannel spectrum.

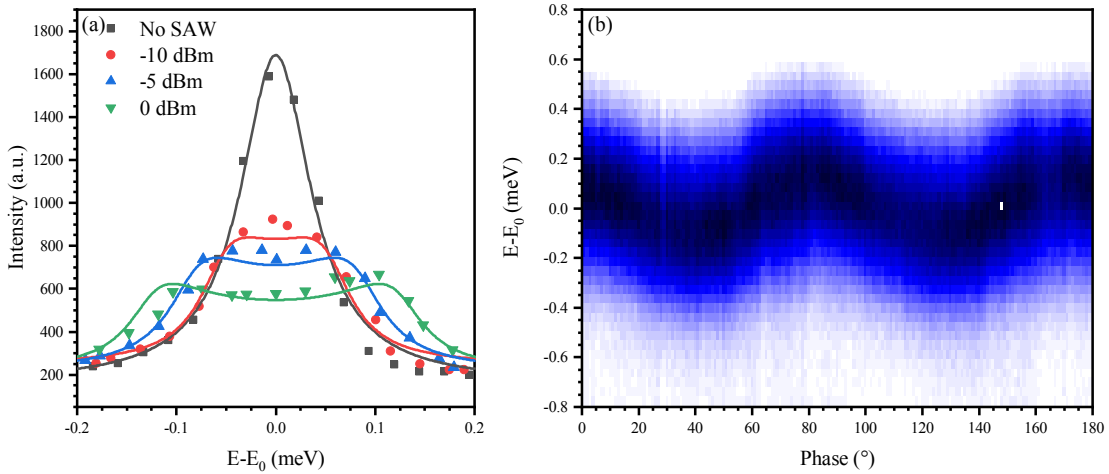


Figure 2.8: (a) Time-integrated and phase averaged stroboscopic measurement of a QD's emission without (black) and with the influence of the SAW at three different powers: -10 dBm (red), -5 dBm (blue) and 0 dBm (green). (b) Phase locked time-integrated stroboscopic measurement of a QD's emission modulated by the SAW. The phase was changed at the laser signal generator.

The rf signal exciting the SAW can also be modulated and the duty cycle of this modulation can also be adjusted. This is done in order to avoid any type of spurious heating of the sample due to the incomplete conversion of the electrical power to mechanical waves. This type of measurement mode is illustrated in the orange dashed rectangle in Figure 2.7 and is only applied for the pulsed excitation mode of the laser. The modulation of the SAW is done by the same signal generator generating the original rf signal and the pulse period T_{mod} as well as the pulse length $T_{mod,SAW}$ can be controlled by the instrument. The ratio between the two quantities defines the duty

cycle of the modulation and is the one adjusted to avoid the heating of the sample. To measure the photoluminescence of the QDs only when they are influenced by the SAW, the laser also has to be modulated and both pulses have to be superimposed at the QD. This is done by applying a matching gate signal of length $T_{mod,laser}$ to the laser driver's gating input or by combining this square pulse with the rf signal provided by the laser signal generator. This gate signal is produced by a delay generator (*Stanford Research Systems*, DG645 or DG535) and the instrument is triggered by the SAW signal generator as illustrated in Figure 2.7. For each rf pulse produced by the SAW signal generator, the delay generator is triggered to emit a square pulse of length $T_{mod,laser}$, delayed by a time t_d . This time delay t_d is adjusted to ensure the overlap of both the laser pulse and the SAW pulse in time at the position of the QD under investigation. The magnitude of the delay t_d depends on the two different signals propagation times. Due to the relative slow SAW velocity, it is thus mostly dependent on the propagation length of the SAW from the IDT to the QD. The delay t_d is usually determined experimentally by recording the emission spectrum of the measured QD as a function of t_d and by selecting the delay time with the highest influence of the SAW on the QD's emission. Due to the time needed for the SAW pulse to be build up by the IDT, the effective length of the physical SAW pulse is shorter than the length set by the signal generator $T_{mod,SAW}$. To ensure the excitation of the QD by the laser only at times when the full SAW amplitude is reached, the length of the laser modulation is taken to be shorter than the SAW gate length ($T_{mod,laser} < T_{mod,SAW}$). The disadvantage of the modulated optical excitation scheme lies in the reduced average emission intensity which leads to longer acquisition times to collect the same number of photons as for the continuous measurement scheme.

In this type of experimental setup, the signal collected is an average of QD's emission over many SAW's cycle. Additionally, in the case of a phase averaged excitation, the QD's excitation by the laser is equally distributed over an acoustic cycle for the cw-excitation or is equally averaged over many acoustic cycles for the pulsed excitation so that the measurement is taken to be a time-integrated measurement of the SAW's influence on the QD's emission. The line shape of such a time-integrated spectrum is described by the integral of a sinusoidally time modulated Lorentzian line over one acoustic cycle [51]:

$$I(E) = I_0 + f_{rf} \frac{2A}{\pi} \int_0^{1/f_{rf}} \frac{w}{4 \cdot (E - (E_0 + \Delta E \cdot \sin(2\pi \cdot f_{rf} \cdot t)))^2 + w^2} dt \quad (2.23)$$

This change in the QD's emission line is illustrated in Figure 2.8(a). The unperturbed Lorentzian emission line (black) changes to the typical double peak structure characteristic of the time modulated Lorentzian line from Equation 2.23 (red). As the applied rf power P_{rf} increases, the modulation of the QD increases and the double peak structure becomes more pronounced (blue and green). Equation 2.23 can be used to fit the spectra and Figure 2.8 shows how the experimental data are nicely reproduced. From the fit, the amplitude of the modulation ΔE can be extracted which, in turn, makes it possible to quantify the local hydrostatic pressure at the position of the quantum dot. This experimental setup provides therefore a simple way to measure the local

strain amplitude induced by a SAW at the position of the QD. However, due to the time-averaging excitation and the time-integrating detection, the time dependence of the modulation cannot be resolved. For this purpose, the phase-locked stroboscopic excitation scheme can be used where the SAW and optical excitation are phase-locked by setting $f_{rf} = n \cdot f_{laser}$, as explained previously. In that case, the QD is excited at a specific time during the acoustic cycle which is controlled by the relative phase between both generators. The whole acoustic cycle can be resolved by changing the phase of one of the signal generator while keeping the other constant. For each phase a spectrum of the QD's emission is recorded and the combination of all these spectra is plotted in Figure 2.8(b) in a false colour plot. The sinusoidal modulation of the QD's signal is clearly resolved. The period of the SAW is resolved for a phase difference of 90° as the phase is changed at the laser signal generator and the laser frequency is fixed at $f_{laser} = f_{rf}/4$. Another possibility to resolve the time modulation of the QD is the use of a time-resolved measurement setup which is described in the next section.

2.3.2 Time-resolved spectroscopy

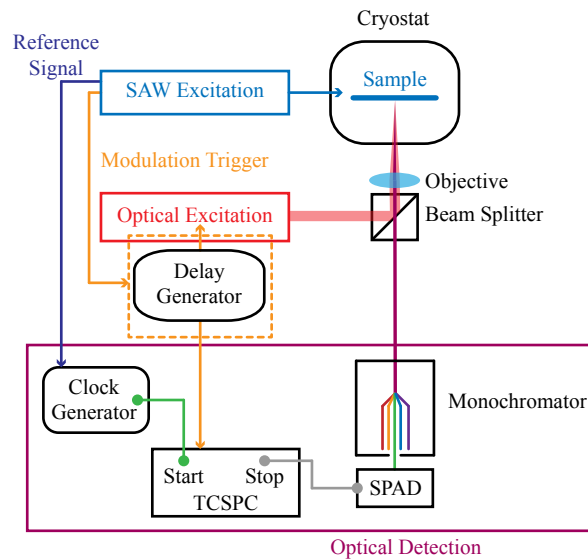


Figure 2.9: Schematic of the time-resolved measurement setup. The SAW excitation, optical excitation and modulation parts are all the same as for the time-integrated measurement. The optical detection of the setup, indicated in purple, changes with respect to the time-integrated setup.

In this measurement scheme, the SAW and optical excitation parts remains the same as in the previous section. However, in the optical detection, the time-integrating detector (CCD camera) after the monochromator is exchanged by a single photon avalanche diode (SPAD) which allows a time-resolved detection of the signal with a high time resolution (< 50 ps). These photodiode devices are perpetually operated beyond their breakdown voltage so that the detection of a single photon leads to an avalanche breakdown detected electrically. After the avalanche breakdown, the diode enters a dead time

where no events can be further detected. This dead time is in the range of 50-80 ns which is much larger than the typical SAW period $T_{SAW} < 8$ ns. Additionally, the maximal number of photons which can be emitted during one acoustic cycle are dependent on the decay rate or lifetime Γ_{QD} of the QD's emission. Due to these two reasons, the direct observation of the SAW dynamics in real time is not possible. To record the SAW dynamics, we use a technique called time-correlated single photon counting (TCSPC). In this technique, the QD under study is periodically excited and the optically detected single photon detection events are correlated with the excitation time.

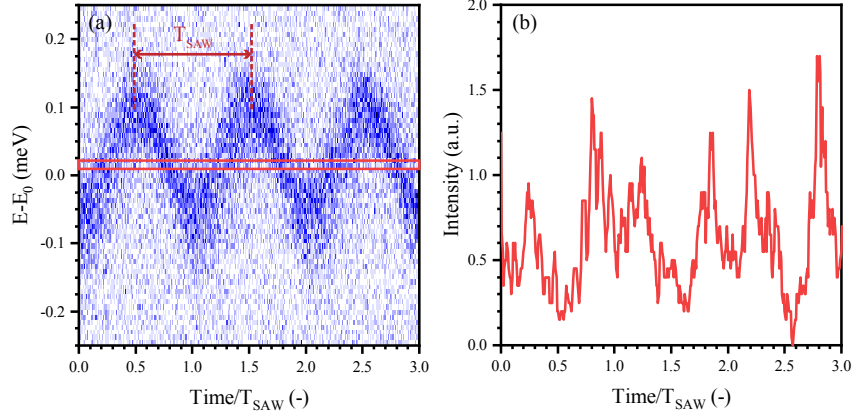


Figure 2.10: (a) False colour plot of the full energy-time modulation of the QD's emission by the SAW. (b) Histogram of the QD's emission counts modulated by a SAW at a fixed energy indicated by the red rectangle in (a).

In our case, the experimental setup using TCSPC is depicted in Figure 2.9. As stated previously, the SAW and optical excitation parts remain unchanged. The collected emission of the QD is spectrally filtered by the same grating monochromator used previously and only photons with a specified energy are detected by a SPAD (*Micro Photon Devices*, PDM) with a time resolution of $\tau_{res} < 50$ ps. The detected counts are correlated in time with respect to a synchronisation signal of frequency $\frac{f_{rf}}{n}$ by a two-channel TCSPC module (*PicoQuant*, PicoHarp 300). The synchronisation signal is delivered by a clock generator (*Stanford Research System*, CG635) and is set to an integer fraction n of the SAW frequency. This fraction is necessary in order to stay below the maximum synchronisation rate of the TCSPC module (84 MHz). The TCSPC module has a function similar to a stopwatch: the synchronisation signal (re)starts the clock at every n -th SAW cycle and a detected photon stops the time measurement. The synchronisation signal should restart the clock at the exact same phase of the SAW for each cycle and therefore, the clock generator is locked to the same reference oscillator than the SAW signal generator. Counts are recorded over many acoustic cycles and can then be plotted as a function of the time between the synchronization trigger and the photon count in a histogram. The detection energy is controlled and swept by the position of the grating inside the monochromator and for each detection energy the time evolution of the QD's emission is recorded. From this, the full spectral and temporal evolution of the QD's emission can be resolved as seen in the false colour plot in Figure

2.10(a). From this type of measurement, the clear sinusoidal modulation of the dot's emission by the SAW can be seen and the SAW period can be resolved. A histogram of a specific detection energy, indicated by the red rectangle in Figure 2.10(a), is plotted in Figure 2.10(b). The clear intensity peaks, where the QD emission energy is equal to the detection energy set by the monochromator, can be observed. Just like in the time-integrated measurements, a modulation scheme can be used and the delay generator provides a gate signal to the TCSPC module to ensure that photons are only counted when the QD is optically excited.

Conclusion

In this chapter, we summarised the fundamental properties of III-V semiconductors GaAs, AlAs, InAs and their ternary alloys. Additionally, the optical properties of the semiconductor heterostructures forming QDs were explained as well as their interaction with surface acoustic waves. The experimental spectroscopy methods used to measure the SAW modulation of the QDs through deformation potential coupling are also described.

Semiconductor Heterointegration

The main goal of this work is to increase the optomechanical coupling between QDs and surface acoustic waves, with the deformation potential coupling as the dominant coupling mechanism. For this purpose, we transfer the QD membrane onto a strong piezoelectric substrate, lithium niobate LiNbO_3 . Indeed, surface acoustic waves can be excited directly onto the GaAs/(Al)GaAs QD wafer thanks to the material's piezoelectricity. However, the electromechanical coupling coefficient K^2 is quite low at $\approx 0.07\%$. On the other hand, LiNbO_3 is the substrate material of choice for SAWs because of its high electromechanical coupling coefficient $K^2 \approx 5\%$ but it does not provide any type of high quality qubit system such as QDs. In this chapter, we present the fabrication techniques used to combine the two materials and their qualities. Firstly, the growth of semiconductor quantum dots is described. Secondly, the fabrication of the SAW-chip is explained followed by the epitaxial lift-off technique used to release the QD membrane and transfer it on top of a LiNbO_3 substrate. Finally, the success of this transfer is analysed and the post-processing of the membrane is shown.

3.1 Epitaxial growth of semiconductor quantum dots

Various methods can be used to produce quantum dots, each with its own advantages and applications. One of these methods is the formation of colloidal QDs in solution by chemical processes. These QDs have a large range of optoelectronic applications such as QD-LED or QD-based solar cells [52]. In this work, the QDs are based on the epitaxial growth of III-V semiconductor systems on top of a GaAs substrate. These type of QDs have good optical properties and can be grown with low enough densities which enables the optical excitation and detection of single QDs. Additionally, a sacrificial layer made of (Al)GaAs with an aluminium content larger than 0.6 can be epitaxially grown without additional strain below the QDs, which makes the release and the transfer of the QDs onto a new substrate via epitaxial lift-off possible. Two types of epitaxially grown QDs were used in this work and both were grown by molecular beam epitaxy but with different processes and in different material systems. The two approaches are described here.

3.1.1 Droplet-etched GaAs/(Al)GaAs QDs

In the case of the GaAs/ $\text{Al}_x\text{Ga}_{(1-x)}\text{As}$ system, the method used is local droplet etching (LDE). In this method, liquid droplets of Ga are used to etch nanoholes into the GaAs substrate which can then be filled to produce the QDs [53]. The QDs used in this work were grown by our collaborators at the Johannes Kepler Universität Linz and the Chinese Academy of Sciences following the technique summarized in Figure 3.1(a) and described by Atkinson and coworkers [54].

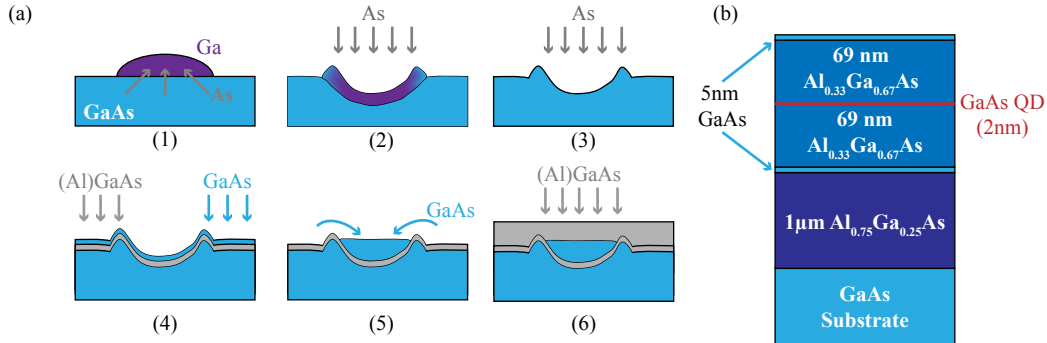


Figure 3.1: (a) Summary of the GaAs QD fabrication. A Ga droplet forms a nanohole in the GaAs substrate (1-3). The hole is then covered by $(\text{Al})\text{GaAs}$ (4) and filled with GaAs (5) and finally capped with $(\text{Al})\text{GaAs}$ (6). (b) Layer structure of the investigated QDs in this work.

The sample is grown by solid state source molecular beam epitaxy. The first step consists in the deposition of Ga which forms droplets on the surface of the substrate (1). The density of these droplets, and thus of the QDs, can be controlled by modifying the flux of Ga during this step. The As contained in the substrate diffuses inside the droplet driven by the concentration gradient at the interface. This migration causes the etching of the nanohole while the droplet spreads out and is being recrystallized by the influx of As (2). The competition between these two processes controls the size of the nanoholes and, therefore, the emission energy of the QDs. Following the complete crystallization of the hole in GaAs (3), an $\text{Al}_x\text{Ga}_{(1-x)}\text{As}$ barrier layer is grown followed by a layer of GaAs (4). The growth is then interrupted to allow for the GaAs to migrate towards the bottom of the holes in order to form the QD (5). The QD is covered by another $\text{Al}_x\text{Ga}_{(1-x)}\text{As}$ barrier layer to ensure full 3D confinement of the charge carriers within the QD (6). The $\text{Al}_x\text{Ga}_{(1-x)}\text{As}$ layer is then capped off with a GaAs layer to avoid its oxidation.

The QDs sample layer structure used in this work is presented in Figure 3.1(b). In this case, a sacrificial layer made of $\text{Al}_{0.75}\text{Ga}_{0.25}\text{As}$ covers the GaAs substrate in order to be used for epitaxial lift-off to transfer the QD membrane present on top. This membrane consists of 2 barrier layers of $\text{Al}_{0.33}\text{Ga}_{0.67}\text{As}$ of 69 nm with the GaAs QDs in the middle. Since the QDs are going to be transferred onto a new substrate, the membrane is sandwiched by two 5 nm-thick GaAs capping layers to avoid oxidation on both sides.

3.1.2 Self-assembled InAs QDs

The sample is again grown by molecular beam epitaxy and uses the lattice mismatch between GaAs and In(Ga)As to create the QDs. This type of growth mode is known as the Stranski-Krastanov growth mode [55]. Due to the lattice mismatch between In(Ga)As and GaAs, absent in the (Al)GaAs system, the epitaxial growth of InAs or In(Ga)As on GaAs is strained and leads to the formation of islands [56, 57, 58]. The QDs used in this work were grown by our collaborators at the TU München.

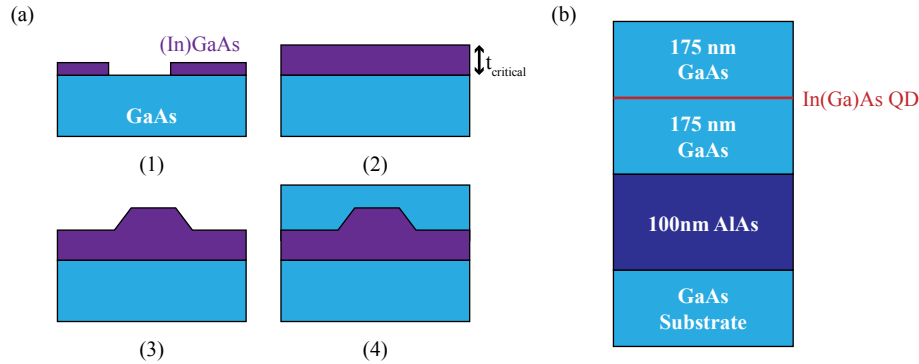


Figure 3.2: (a) Summary of the InGaAs QD fabrication. In(Ga)As is deposited on top of the GaAs substrate in a 2D growth mode (1). When the layer reaches a critical thickness (2), the strain is released by growing islands in a 3D growth mode (3). When the islands have reached the desired size, they are encapsulated in a GaAs barrier layer (4). (b) Layer structure of the investigated QDs in this work.

The growth process is summarised in Figure 3.2(a). It starts with a layer-by-layer growth in 2D which forms what is known as the wetting layer (1). This layer is strongly strained due to the lattice mismatch and the strain increases with the growth until a critical thickness is reached (2). Beyond this thickness, it becomes energetically favourable to form islands to release the strain energy contained in the layer (3). These islands are then covered by a GaAs layer to passivate the surface and ensure the 3D confinement of the charge carriers inside the QDs (4). The size and the position of the QDs follow a statistical distribution, which the centre and the width of can be controlled via the growth conditions. These parameters can be difficult to control so the dots are often grown with a gradient of the In-content across the wafer by stopping the rotation of the wafer during the In(Ga)As deposition. In the region with lower concentration of In, a continuous wetting layer of In(Ga)As without any island is present. As the content of In increases across the wafer, the lattice mismatch and therefore the strain in the grown layer becomes more prominent and it leads to an increase in the QDs density [44]. The photoluminescence of the QDs which is spectrally distinct from the wetting layer can be mapped across the wafer. From this information, a position in the wafer with a low density of QDs can be selected and separated from the wafer to be used for our experiment.

The wafer layer structure of the QDs used in this work is displayed in Figure 3.2(b). Once again, a sacrificial layer is grown below the QD membrane. In this case, it consists

in a 100 nm-thick AlAs layer followed by a 350 nm-thick membrane with the In(Ga)As QDs in the centre. The thickness of the GaAs layer was chosen to contain the light in photonic devices patterned on a LiNbO₃ substrate.

3.2 SAW-chip fabrication

Before the transfer of the QD membrane by epitaxial lift-off, the SAW transducers and/or resonators have to be patterned on the LiNbO₃ substrate. Usually, this step is done by photolithography but, in this work, the use of original patterns not present on already available mask makes it difficult. Therefore, the SAW-chips presented here were prepared using electron beam lithography (EBL).

3.2.1 E-beam lithography

In a classical E-beam lithography/lift-off process, the die is taken from a LiNbO₃-128°Y-X cut wafer. It is spin-coated with two layers of PMMA with different density, followed by a coatable conductive polymer AR-PC 5091 (Electra 92), which is water soluble and can be removed with water before developing the resist. This polymer is used to avoid the electrical charging of the substrate and the subsequent drifting effect during the E-beam writing process, which are common for insulating materials such as LiNbO₃. The parameters for the spin-coating of the resists on the substrate are:

1. PMMA spin-coating
 - PMMA 495K, 30 s at 5000 rpm
 - Baking for 90 s on a hot plate at 190 °C
 - PMMA 950K, 30 s at 5000 rpm
 - Baking for 90 s on a hot plate at 190 °C
2. Elektra spin-coating
 - Elektra 92, 60 s at 2000 rpm
 - Baking for 120 s on a hot plate at 90 °C

The exposure of the resist in the E-beam system is done at 10 kV with an aperture of 30 μm and a basis dose of 100 μC cm⁻². After exposure, the Elektra coating is dissolved in DI water and the resist is developed in a MIBK:IPA 1:3 solution.

3.2.2 Metallisation and lift-off

After the lithography step, the sample is subsequently cleaned in a O₂ plasma at 600 W with 55 sccm for 13 s to ensure the correct adherence of the deposited metal to the substrate. The metal deposition is done in a E-beam vapour deposition system. The metal layer consist of either 5 nm Ti followed by 50 nm Al or 5 nm Cr followed by

50 nm Au. The Cr/Au combination is used when the post-processing of the membrane could damage the Al IDTs so a more inert material is used. The lift-off process is then completed by dissolving the PMMA resist in acetone and using an ultrasound bath to remove any metal and resist residues. The substrate has to be as clean as possible for the transfer of the (Al)GaAs membrane.

3.3 Epitaxial lift-off and transfer

The epitaxial lift-off (ELO) technique is based on the high selectivity ($\sim 10^7$) of the HF acid etchant between GaAs and $\text{Al}_x\text{Ga}_{1-x}\text{As}$ for $x \geq 0.6$ [22, 59]. This process was first developed by Yablonovitch and coworkers in 1987 [22] and is often used for optoelectronic applications such as the release of thin-film III–V solar cells on larger scales [60, 59, 61]. New applications also include incorporating InAs/InP QDs as a quantum emitter on top of integrated photonic circuits (IPCs), i.e. etched thin film LiNbO_3 due to its strong opto-electric effect and its strong $\chi^{(2)}$ optical nonlinearity [62], or on a more classical silicon photonic chip, compatible with CMOS technology [63].

To enable ELO, the QDs membrane is grown on top of a sacrificial layer consisting of $1\ \mu\text{m}$ $\text{Al}_{0.75}\text{Ga}_{0.25}\text{As}$ for the etched GaAs QDs provided by our partners in Linz and of $100\ \text{nm}$ AlAs for the self-assembled InAs QDs produced at the TU München. A piece of the QD wafer is cut along the compact directions. Its size is around $3 \times 3\ \text{mm}^2$. The upper side of the wafer is covered with *Apiezon* wax and linked to a thread of the same wax, which is done by melting the wax on the sample on a hot plate. The role of the wax is to support the film after the lift-off and to help with its transfer [23]. The sample is then left overnight (12 h) for the AlAs layer or 24 h for $\text{Al}_{0.75}\text{Ga}_{0.25}\text{As}$ in HF 10%. Once the etching is completed, the film is rinsed in water and kept in that environment before transferring it on the clean SAW-chip. During the placement of the membrane on the substrate, a water droplet at the bottom of the membrane is used to carefully position it without damage but also to draw the membrane to the surface to ensure a good bonding [23]. The sample is then left to dry overnight or on a hot plate at $30\text{--}40\ ^\circ\text{C}$ for 2–3 h to get rid of any water present at the interface. After drying, the *Apiezon* wax is slowly diluted in toluol by dropping the solvent drop by drop with a pipette on the sample. The sample is then carefully cleaned with acetone and IPA.

3.3.1 Palladium adhesion layer

The bonding present between the transferred (Al)GaAs membrane and the LiNbO_3 substrate is characterised as a van der Waals bonding [23]. While still being moderately strong, the bonding relies on surface interactions which might be detrimental for efficient mechanical transduction between the SAW travelling on the substrate and the epilayer. To ensure a strong mechanical bond, a Pd adhesion layer can be used. This metal is chosen because it reacts easily with compound semiconductors at low temperatures ($\leq 200\ ^\circ\text{C}$). Yablanovitch and coworkers have shown that, after the transfer of a GaAs membrane on such a Pd layer, a solid-state topotaxial reaction forms the compound Pd_4GaAs at the interface even without an annealing step at $200\ ^\circ\text{C}$ [64]. The formation

of this new phase ensures a strong metallurgic bond, which withstands most clean room processes such as spin coating, lithography, etching, etc [64]. The Pd layer has also the advantage of screening the electric field of the SAW so that only the mechanical interaction between the QD and the SAW is present.

The palladium layer is produced on the LiNbO_3 using a typical photolithography process with a positive resist S1813 prior to ELO. The resist is spin coated on the SAW-chip at 5000 rpm for 30 s and then baked at 115°C on a hot plate for 2 min. The sample is exposed to UV light through a simple squared mask of $3\times 3\text{ mm}^2$ for 30 s and then developed for 10 s in $\text{D351:H}_2\text{O}$ 1:5. An O_2 plasma at 500 W with 55 sccm for 20 s cleans any organic residues from the developed resist and a metal layer of 5 nm Ti followed by 50 nm Pd is deposited in a E-beam vapour deposition system. After dissolving the resist in acetone, the LiNbO_3 substrate is thoroughly cleaned in an ultrasound bath to be ready for the transfer of the QD membrane. The ELO and transfer happens in the same way as described previously but a last annealing step at 200°C for 1 h is included to ensure the formation of the Pd_4GaAs phase after the dissolution of the *Apiezon* wax.

3.3.2 Confirmation of the Pd-GaAs interdiffusion

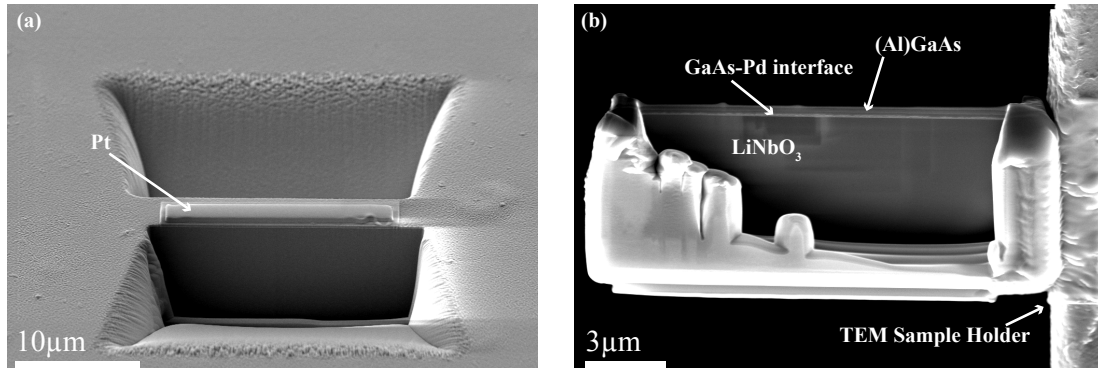


Figure 3.3: (a) Scanning electron microscope image of the two cavities etched by the focused ion beam with the strip of $(\text{Al})\text{GaAs-Pd-LiNbO}_3$ in between protected by a layer of Pt deposited in the FIB. (b) Lamella of the $(\text{Al})\text{GaAs-Pd-LiNbO}_3$ sample thinned using the focused ion beam and attached to the TEM grid.

To ensure that the method we used succeeded in forming the Pd_4GaAs compound and to have a better look at the interface between the epilayer and the Pd adhesion layer, we used a focused ion beam (FIB) system to cut a lamella from a test sample which could be subsequently examined in a transmission electron microscope (TEM). This process was performed by Maximilian Gnedel of the Lehrstuhl für Experimentalphysik 1 at Augsburg University. The first step consists in the deposition of a Pt precursor which is activated by the ion beam, leaving a line of amorphous Pt protecting the region of interest. Secondly, the lamella is isolated by using the ion beam to mill two deep holes on each side. This step of the process is shown in Figure 3.3(a) where both milled holes can be seen surrounding the lamella protected by the amorphous Pt. The lamella is further separated from the substrate by the ion beam and attached to a

micromanipulator by depositing Pt at the intersection. From the micromanipulator, the lamella is transferred to a TEM sample holder or a grid using the same Pt-deposition and ion beam etching technique. The lamella is then thinned down by using the ion beam to mill its edges. The finished lamella is presented in Figure 3.3(b) with the TEM sample holder on the right hand side of the SEM image. The different layers are already visible with the amorphous Pt on top, followed by the (Al)GaAs membrane. At the interface, the Pd layer is clearly seen in a much lighter contrast as the other layers on top of the LiNbO_3 substrate and is indicated in the image.

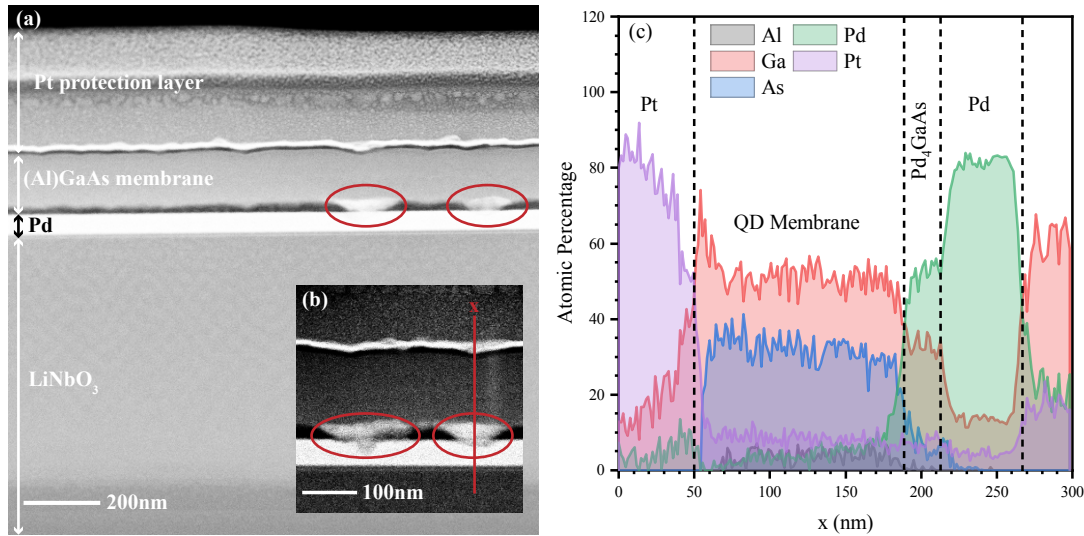


Figure 3.4: (a) Transmission electron microscope image of the lamella showing the different layer, the Pt protection layer, the (Al)GaAs membrane, the Pd adhesion layer and the LiNbO_3 substrate. (b) Transmission electronic microscope image of the lamella at the position where the EDX analysis is done. (c) Position dependent element composition of the lamella along the line in (b) done by EDX analysis.

The resulting analysis in TEM is presented in Figure 3.4. In the TEM images, all the layers are clearly resolved: the Pt amorphous protection layer, followed by the (Al)GaAs membrane, the Pd adhesion layer and the LiNbO_3 substrate. Importantly, we can assess the quality of the Pd-GaAs interface: the Pd_4GaAs compounds can be identified at several positions (red ellipses) and shows that the bonding is successful. Some defects are also present where the contact with the membrane was not well established. Figure 3.4(c) show an energy dispersive X-ray (EDX) spectroscopy analysis along the line plotted in Figure 3.4(b) which quantify the composition percentage of each element. The different regions are easily identified in the plot. This analysis confirms the interdiffusion of Ga and Pd and thus the formation of the anticipated Pd_4GaAs phase [64]. Looking closely at the SEM image in Figure 3.3(b), we can see that the membrane is well bonded but presents some amount of defects. The bonding is thus definitely successful where the contact was well established between the membrane and the Pd layer. Knowing that we transferred a large membrane, $\approx 3 \times 3 \text{ mm}^2$, the presence of some defects due to dirt or imperfect contact was expected.

3.4 Post-processing of the (Al)GaAs membrane

A post-processing of the (Al)GaAs membrane is often necessary due to the irregular shape of the as-transferred membrane. An as-transferred membrane is shown in Figure 3.5(a) and the jagged edges and some defects such as the hole in the centre of the membrane can be clearly seen. To ensure a constant interaction length between the SAW and the membrane and to avoid unwanted losses by scattering and reflections at the edges, the membrane is etched in a rectangular shape. Additionally, more complex post-processing of the epilayer opens the possibilities for the functionality of the hybrid. As an example, the fabrication of more complex structures such as photonic or phononic resonators and integrated circuits is also possible using E-beam lithography. This was achieved here by the fabrication of ring resonators in a GaAs membrane containing InAs dots.

3.4.1 Photolithography and chemical etching

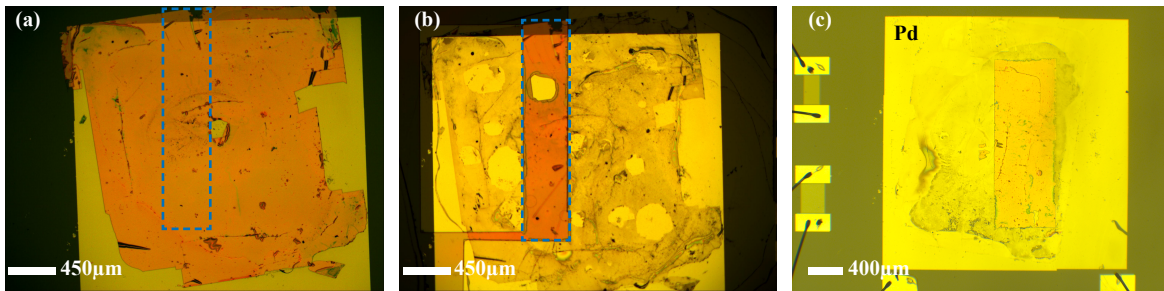


Figure 3.5: Microscope pictures of transferred (Al)GaAs membranes before (a) and after (b-c) chemical etching of the membrane in a rectangular shape. The rectangular shape conserved in (b) is shown in the initial membrane in (a) by the blue rectangle.

The first step to achieve the rectangular isolation of a semiconductor membrane, such as the one displayed in Figure 3.5(a), is a photolithography with a negative resist AZ-nLOF-2020. The resist is spin coated on the sample at 3000 rpm for 30 s and then baked at 110 °C on a hot plate for 60 s. The region of interest is then exposed through a simple rectangular mask to UV light for 7 s. This rectangular region is highlighted in Figure 3.5(a) by the blue rectangle and corresponds to the isolated region in Figure 3.5(b), also highlighted by a blue rectangle. The development is done in AZ 826 Mir for 60 s. The membrane not protected by the resist is then etched using a solution of $\text{H}_2\text{O}_2:\text{H}_2\text{SO}_4:\text{H}_2\text{O}$ in volume proportion of 1:8:200. This anisotropic etching solution is suitable for this system due to its low selectivity between GaAs and AlAs and their ternary alloys. The etch rate of $\sim 250 \text{ nm min}^{-1}$ means that the sample only needs to stay 60 s in the solution. The resist can then be washed away with acetone. The result of such a post-processing is presented in Figure 3.5(b) and (c) for two different samples. The sample presented in Figure 3.5(a) and (b) is analysed in chapter 4 and the corresponding isolated region is highlighted by a blue rectangle in both images. The sample displayed in Figure 3.5(c) is studied in chapter 5 and shows the successful

isolation of a rectangular region with little to no defects. The IDTs exciting the surface acoustic waves can be seen on the left hand side. The black residues which can be observed beside the membrane could be residues of Pd_4GaAs [64]. The clear region where the palladium is clearly visible shows the positions where the semiconductor membrane did not bond successfully to the Pd layer.

Additionally, this etching technique can be applied to etch and isolate multiple smaller mesas. This was done by Pustiowski and coworkers to a transferred GaAs-based p-i-n doped membrane [24]. The membrane was etched to produce several photodiodes each containing a single layer of InAs QDs. By contacting the diodes at the top and the bottom, the QDs can be statically tuned by an electric field in addition to the dynamic modulation of the SAW.

3.4.2 Photonic devices

The ring resonators presented in this section and studied in Chapter 6 are much more complex than the previous mesa and require the use of E-beam lithography and reactive ion etching (RIE). The design and development of the production method was done in collaboration with Bruno Villa Piñeros of the University of Cambridge. Both these methods have a higher precision than the one used previously and the RIE results in extremely straight and smooth etched edges, which is of paramount importance for photonic devices such as ring resonators and waveguides. The epilayer used for this sample is a 350 nm-thick GaAs membrane with InAs dots in the centre, which was grown by our collaborators at the TU München. The membrane is transferred directly onto the free LiNbO_3 substrate without the Pd layer which could potentially bring optical losses and damage the confinement of the light inside the waveguide and ring resonator.

The resist used here is the negative resist ma-N2403 which withstands well the reactive ion etching. For the resist to adhere correctly to the substrate and the GaAs membrane, they must be treated with O_2 plasma and dried for at least 30 min in an oven at 200°C . An adhesion promoter is also necessary; the Surpass 4000 was used in combination with the ma-N2403 resist. Since LiNbO_3 is an insulator, the Elektra coating is used once again. Due to the presence of small features in the range of 100 nm, the EBL software must do a proximity correction where the larger form of the ring resonator is divided in many small rectangular exposition regions. The dose factor of each region is calculated by taking into account the backward scattered electrons coming from the exposure of the neighbouring regions. The exposure is done at 20 kV with an aperture of $10\ \mu\text{m}$ to increase the precision of the exposition. The basis dose is still kept at $100\ \mu\text{C cm}^{-2}$. The preparation process is summarized below:

1. O_2 Plasma
 - 500 W, 55 sccm O_2 , 20 s
2. Baking in oven
 - At least 30 min at 200°C

3. Surpass 4000

- Spin coating: 30 s at 3000 rpm
- DI water rinse
- IPA rinse
- N₂ drying

4. ma-N2403

- Spin coating 30 s at 3000 rpm
- Baking 60 s at 90 °C on a hot plate

5. Electra 92

- Spin coating 60 s at 2000 rpm
- Baking 120 s at 90 °C on a hot plate

After the exposure, the Elektra is dissolved with water and the resist is developed in ma-D532 for 45 to 60 s. A hard bake after the development is necessary to harden the resist for the RIE. This is done for 2 min on a hot plate at 90 °C.

After the development of the resist, the samples were taken to Toshiba's facilities in Cambridge where a conventional reactive ion etching process was used to etch the ring resonators. Finally, the resist is stripped by using acetone. The SEM images displayed in Figure 3.6 show that the fabrication was quite successful and promising for a first attempt at this complex fabrication. In Figure 3.6(a), a ring resonator with a 6 μm diameter is shown and it displays the necessary smooth edges, and the gap with the access waveguide on the left hand side is well defined. The grating coupler displayed in Figure 3.6(b) shows the desired apodization of the grating and proves that the lithography and etching of small structures in GaAs-LiNbO₃ hybrids is successful. The optical and optomechanical characterisation of these devices is presented in Chapter 6.

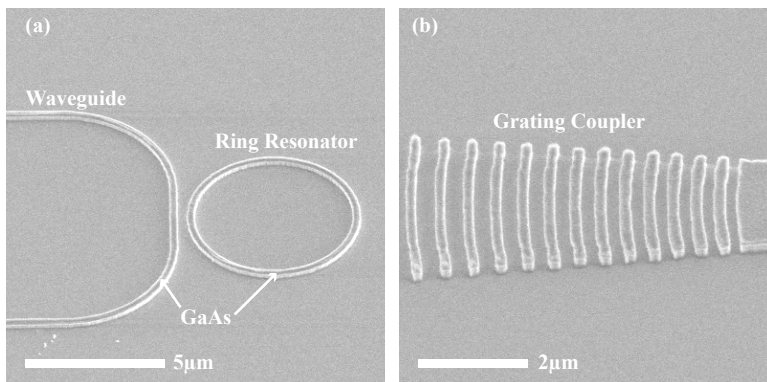


Figure 3.6: Scanning electronic microscope images of the devices after etching and stripping of the resist. (a) Ring resonator and waveguide and (b) grating coupler.

Conclusion

In this chapter, the sample fabrication was introduced and the successful heterointegration of semiconductor quantum dots on lithium niobate was demonstrated. The developed technology creates a solid foundation for the fabrication of advanced LiNbO_3 -III-V hybrids which are studied in the remainder of this thesis. The semiconductor membrane can be transferred inside an increasingly complex SAW-chip design, from delay lines to SAW resonators or can be process into complex photonic or phononic circuit and resonators.

Analysis of the SAW Propagation in Fused (Al)GaAs-LiNbO₃ Hybrids

The previous chapter already established the technique to successfully transfer semiconductor QDs membrane onto a LiNbO₃ SAW-chip in order to enhance the optomechanical coupling between QDs and surface acoustic waves compared to the monolithic devices. From there, we want to systematically study the coupling between the transferred QDs and the SAW. For this purpose, we analyse the propagation and coupling of the SAW across and to one of this transferred epilayer before moving towards more complex systems. In this chapter, the coupling of SAWs to the QDs inside a transferred semiconductor membrane is analysed using finite element simulations. The FEM simulations show the localisation of the acoustic field inside the semiconductor membrane which leads to a larger optomechanical coupling of the dots to the SAWs compared to the one computed for the monolithic device. To confirm the simulation results, a hybridised sample was fabricated and the coupling of the SAW to the epilayer was quantified by measuring the SAW signal transmitted across the hybridised delay line and the optomechanical response of the dots. Using a Split-52 IDT design [21], we are able to measure both signals simultaneously and over a large range of frequencies, from 150 MHz to 600 MHz. As the frequency of the SAW increases, we observe a clear increase of the QDs modulation amplitude. Our findings confirm the localisation of the SAW's acoustic field inside the semiconductor membrane due to acoustic wave guiding. This in turn increases the optomechanical coupling parameter with the increasing frequency.

The main results of this chapter were published in the Journal of Physics D: Applied Physics under the title "Multi-harmonic quantum dot optomechanics in fused LiNbO₃-(Al)GaAs hybrids" [51].

4.1 Finite element simulation of QD-SAW coupling

We quantify the coupling of the QDs to the SAW in (Al)GaAs-LiNbO₃ hybrid devices, employing finite element modelling (FEM) simulations using a commercially available software, Comsol Multiphysics [13]. The simulation is performed in a 2D unit cell

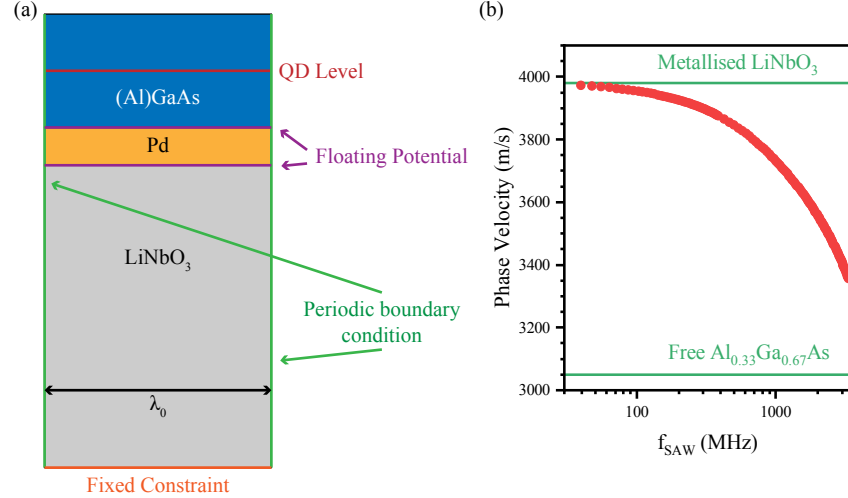


Figure 4.1: (a) Geometry of the unit cell used for the finite element method simulation of the pressure at the QD level. (b) Computed SAW phase velocity inside the hybrid structure as a function of the SAW frequency.

displayed in Figure 4.1 (a), which corresponds to the heterostructure. Each layer is represented: LiNbO₃ in grey, 50 nm-thick Pd in yellow and 150 nm-thick Al_{0.33}Ga_{0.67}As in blue. The QD level is indicated by a red line in the middle of the (Al)GaAs membrane. The side borders of the unit cell (in green) are under mechanical and electrical periodic boundary condition and the lower boundary (in orange) is set as fixed. The Pd layer is treated as a non-piezoelectric material and electrical floating boundary condition (in purple) are applied above and below the layer. The width of the unit cell is swept and fixes the wavelength of the SAW solution, indicated by λ_0 in Figure 4.1(a). For each wavelength, the eigenfrequencies of the unit cell are computed and the one for the SAW solution is selected. From this solution, the phase velocity of the wave inside the hybrid structure can be extracted for each SAW frequency, as well as the hydrostatic pressure at the position of the dots in the centre of the (Al)GaAs membrane (red line). The material parameters used for this simulation at room temperature and at 10 K are presented in Appendix A. Figure 4.1(b) shows the dispersion of the wave phase velocity extracted from the simulation at 10 K as a function of the SAW frequency in the hybrid structure in a semi-logarithmic scale. At low frequency, the thickness of the layer is much smaller than the wavelength of the SAW and the velocity is close to the one for a metallised LiNbO₃ surface $c_{0,mLNO,10K} = 3980 \text{ m s}^{-1}$. As the frequency increases, the SAW is localised closer to the surface and the (Al)GaAs membrane acts as a dispersive overlayer and the phase velocity rapidly decreases towards the phase velocity of SAW in pure Al_{0.33}Ga_{0.67}As, $c_{0,AGA,10K} = 3050 \text{ m s}^{-1}$.

To quantify the coupling of the QDs to the SAW, the optomechanical coupling parameter $\gamma_{OM} = \frac{\partial(\Delta E_{QD})}{\partial u_z}|_{z=0}$ is computed. This is done by extracting the derivative of the hydrostatic pressure at the position of the dots on the vertical displacement at the surface of the epilayer $\frac{\partial p(QD)}{\partial u_z(z=0)}$ from the simulation and multiplying it with the deformation potential coupling strength $\frac{dE_{gap}}{dp} = 150 \text{ } \mu\text{eV MPa}^{-1}$ [21, 65]. The obtained

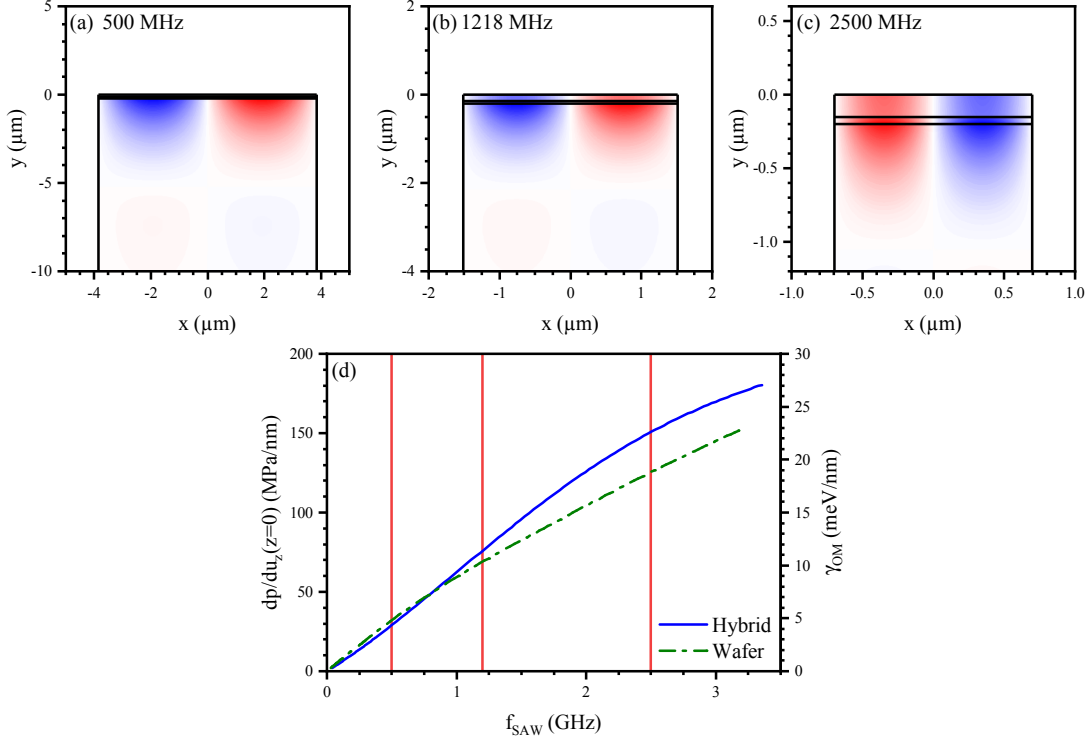


Figure 4.2: (a-c) Colour plots of the pressure per nm vertical displacement resulting from the SAW inside the unit cell with a membrane thickness of 150 nm for a SAW frequency of 500 (a), 1218 (b) and 2500 MHz (c). The value ranges are -11 to 11 MPa nm^{-1} , -56 to 56 MPa nm^{-1} and -138 to 138 MPa nm^{-1} , respectively. (d) Pressure per nm of vertical displacement at the position of the QDs and optomechanical coupling parameter as a function of the frequency of the SAW for the QD sample before and after ELO transfer onto LiNbO_3 .

data are plotted in Figure 4.2.

In Figure 4.2(a-c), the calculated hydrostatic pressure profile is plotted for three different frequencies, 500 MHz (a), 1218 MHz (b) and 2500 MHz (c). These profiles show an increased localisation of the acoustic field inside the membrane for higher frequencies. This is further highlighted by looking at $\frac{\partial p}{\partial u_z}$ and γ_{OM} plotted in Figure 4.2(d) for the hybrid layer structure (blue line) and for the original QD wafer structure (green dotted line). The optomechanical coupling parameter for the original wafer was calculated in the same manner as for the hybrid system but using the layer structure presented in chapter 3 Figure 3.1(b). The red vertical lines show the three different frequencies for which the pressure profiles are plotted in Figure 4.2(a-c). For low frequencies $f_{SAW} \leq 1$ GHz, both quantities increase linearly with f_{SAW} and are similar between the hybrid structure and the original wafer structure. In this regime, the thickness of the membrane is small compared to the acoustic wavelength and, therefore, the substrates directly induce the hydrostatic pressure within the QD membrane and the QD's modulation simply follows the linear increase of $\frac{\partial p}{\partial u_z}$ at the surface of the LiNbO_3 substrate or of the GaAs substrate in the case of the original structure. Additionally, the calculated

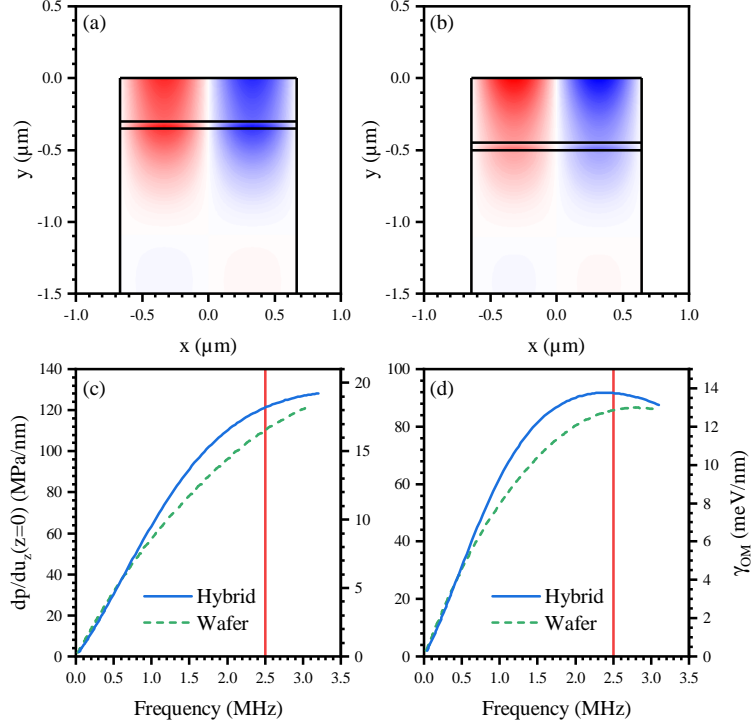


Figure 4.3: (a-b) Colour plots of the pressure per nm vertical displacement for a constant frequency of 2500 MHz and two membrane thickness of 300 nm (a) and 450 nm (b). The value ranges are -175 to 175 MPa nm^{-1} and -148 to 148 MPa nm^{-1} , respectively. (c-d) Pressure per nm of vertical displacement at the position of the QDs and optomechanical coupling parameter for the QD sample before and after ELO transfer onto LiNbO_3 for two membrane thickness of 300 nm (c) and 450 nm (d).

values for γ_{OM} for this hybrid device are in the same range as the one achieved in a previous work for a SAW directly excited on a similar $(\text{Al})\text{GaAs}$ heterostructure [21]. For the hybrid, $\gamma_{OM} = 1.45$ meV nm^{-1} is extracted at $f_{SAW} = 180$ MHz compared to $\gamma_{OM} = 1.8$ meV nm^{-1} for the sinusoidal SAW at $f_{SAW} = 182.7$ MHz reported in [21].

At high frequencies $f_{SAW} > 1$ GHz, the linear dependence of $\frac{\partial p}{\partial u_z}$ and γ_{OM} on f_{SAW} is broken and the quantities gradually saturate in the hybrid layer structure as seen in Figure 4.2(d). This is due to the transition from a LiNbO_3 -dominated regime towards an acoustic waveguiding regime. In the latter, the acoustic field shifts from the high velocity material, LiNbO_3 , into the material with a lower phase velocity, in this case the $(\text{Al})\text{GaAs}$ membrane. The SAW becomes then fully localised in the membrane and the optomechanical coupling of the QD, γ_{OM} , is therefore enhanced compared to the monolithic device (depicted in chapter 3 Figure 3.1(b)). This is shown in Figure 4.2(d). Additionally, the FEM simulations in Figure 4.2(d) predict $\gamma_{OM} > 25$ meV nm^{-1} for $f_{SAW} \approx 3$ GHz. As it is clear from the plot in Figure 4.2(d), this value is larger than the one predicted for SAWs excited directly on the initial wafer structure before epitaxial lift-off. Additionally, the advantage of the LiNbO_3 substrate is the higher electromechanical coupling coefficient K^2 , which means that the conversion of the rf power into mechanical power is more efficient on LiNbO_3 . Therefore, while at lower

frequencies the coupling is comparable between the hybrid and the monolithic device, the absolute vertical displacement achievable in the hybrid structure is larger than the ones achievable for the monolithic device and so the SAW-QD coupling is likely to be larger in the hybrid device.

This localisation of the acoustic field inside the membrane can be enhanced for a given frequency when the (Al)GaAs layer thickness is increased as it is shown in Figure 4.3 for two membrane thickness, 300 and 450 nm respectively. The two pressure profiles in Figure 4.3(a) and (b) clearly show the increased localisation of the field inside the membrane for the same high frequency $f_{SAW} = 2500$ MHz and the two different membrane thickness. Additionally, $\frac{\partial p}{\partial u_z}$ and γ_{OM} , plotted in Figure 4.3(c) and (d) for the two membrane thickness respectively, show the same localisation of the pressure inside the membrane and enhancement of the QD modulation above a certain frequency threshold. However, the absolute value of the optomechanical coupling parameter γ_{OM} saturates to lower values for the thicker membranes than for the thinner membrane presented in Figure 4.2. This is due to the confinement of the field in the membrane as, for thin membranes, the acoustic fields are confined within a smaller length scale compared to thick membranes. Furthermore, the data for the 450 nm-thick membrane in the hybrid structure decreases and reaches the value for the original wafer structure in the higher frequencies range, $f_{SAW} > 2.5$ GHz. For such high frequencies, the QD position, which is in the centre of the membrane, becomes too deep for the SAW wavelength and the pressure maximum of the acoustic wave becomes localised above it. Therefore, the pressure and thus the optomechanical coupling of the dot steadily decrease until the dot is positioned deeper than one acoustic wavelength and the SAW can no longer modulate the QD emission line.

4.2 Sample geometry

To confirm the predicted enhancement of the optomechanical coupling parameter, γ_{OM} , of QDs to SAWs and additionally to analyse the coupling of the SAW to the epilayer, a hybridised sample is fabricated using the fabrication techniques presented in chapter 3. The sample studied in this chapter is shown schematically in Figure 4.4(a). Two delay lines composed of three Ti/Al (5 nm/50 nm) IDTs (IDT 1-3) were patterned onto an oxygen-reduced 128° rotated Y-cut $\text{LiNbO}_{(3-x)}$ substrate using electron beam lithography. The geometry of the IDTs is a Split-52 geometry which was developed by F. Schülein [21]. The finger geometry of this IDT's period is presented in Figure 4.4(a). It consists in five fingers, two for each polarity and a neutral floating finger which is present to avoid the perturbation of the wave propagation in the IDT. This IDT geometry was chosen for its specific electrical properties which are presented in the next section. The left delay line (IDT 1-IDT 2) is kept bare, while a 50 nm-thick Pd adhesion layer is deposited in the right delay line (IDT 2-IDT 3). On top of this layer, an (Al)GaAs membrane is transferred. This 150 nm-thick membrane consists of a 140 nm-thick $\text{Al}_{0.33}\text{Ga}_{0.67}\text{As}$ layer passivated by two 5 nm-thick GaAs layers on each side. In the centre of this membrane, a layer of GaAs QDs was fabricated by the droplet etching and filling technique explained in chapter 3 by our collaborators at the

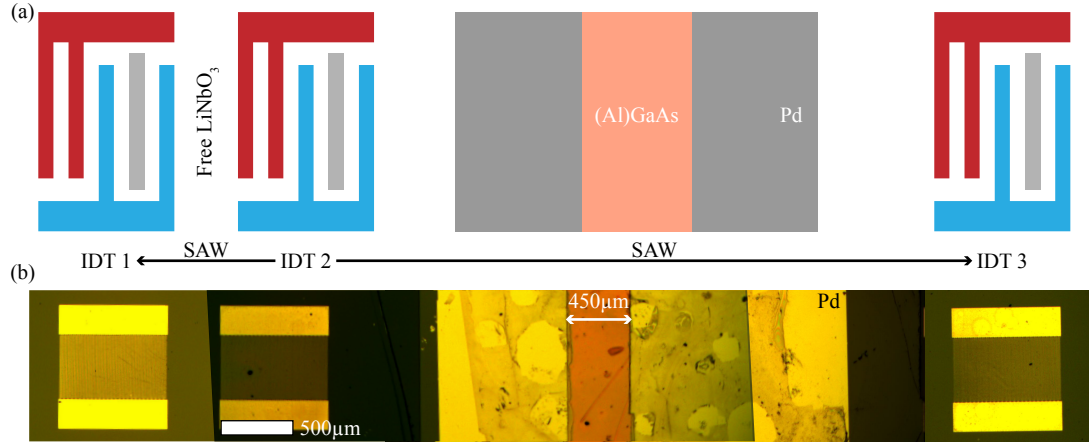


Figure 4.4: (a) Schematic depiction of the device showing the IDT1-IDT2 free LiNbO₃ surface delay line and the IDT2-IDT3 delay line containing the epilayer on top of the Pd adhesion layer. The arrows show the SAW propagation direction which is aligned with the X axis of the LiNbO₃ substrate. (b) Microscope picture of the studied sample.

Johannes Kepler Universität Linz [54]. The transfer was achieved by epitaxial lift-off, dissolving the 1 μm-thick Al_{0.75}Ga_{0.25}As sacrificial layer below the QD membrane in a dilute HF solution. After the transfer onto the Pd adhesion layer, the epilayer was post-processed into a rectangular shaped mesa with a lateral size of 450 μm by wet chemical etching. This ensures a constant interaction length of the SAW and the membrane and avoids unwanted losses by scattering and reflections (see chapter 3). A micrograph of the final device is displayed in Figure 4.4(b). All three IDTs are visible, surrounding the palladium layer and the (Al)GaAs membrane whose lateral length of 450 μm is indicated. This double delay line geometry is inspired from SAW-based sensors, where the signal emitted by the centre IDT is picked up by the external IDTs. The delay line IDT1-IDT2 contains a free LiNbO₃ surface and serves as a reference. The second delay line IDT2-IDT3 line contains the active layer and its signal is compared to the reference signal of the IDT1-IDT2 delay line [66].

4.3 Electrical characterisation

The Split-52 IDT geometry shown in Figure 4.4(a) is deliberately chosen because it enables the excitation of not only the 1st but also the 2nd, 3rd and 4th SAW harmonics [21]. In contrast, symmetrical geometries, such as Split-1 or Split-2 IDTs, cannot excite the 2nd and 4th harmonics. The calculated frequency response of this IDT design is presented in Figure 4.5(a) and is calculated using the discrete sources method described in chapter 1 [31, 27]. The fundamental harmonic is given by the period of the design, in this case $\lambda_0 = 26.6 \mu\text{m}$, which gives a fundamental frequency $f_1 = 150 \text{ MHz}$ for a SAW velocity $c_{0,LNO} = 3990 \text{ m s}^{-1}$ on the free LiNbO₃ surface along the X-direction. The other three harmonics are clearly observed at 300, 450 and 600 MHz, respectively, with the characteristic $\frac{\sin X}{X}$ form around f_n due to the finite length of the transducer.

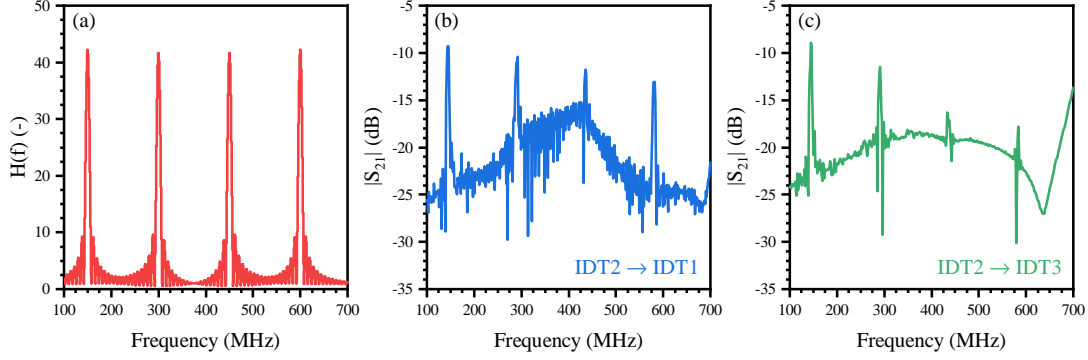


Figure 4.5: (a) Frequency response function of the Split-52 IDT calculated using the discrete source method. (b-c) Transmission scattering parameter S_{12} measured using a vector network analyzer (b) from IDT 2 to IDT 1 across the free LiNbO_3 surface and (c) from IDT 2 to IDT 3 across the transferred (Al)GaAs membrane and the Pd adhesion layer.

These tailored frequency characteristics allow for the characterisation of the SAW's propagation and coupling across and to the epilayer at different frequencies.

The fabricated sample is characterised at room temperature by a vector network analyser for both delay lines. The magnitude of the measured transmission scattering parameter $|S_{21}|$ is plotted in Figure 4.5(b) and (c) for the SAW transmission on free LiNbO_3 (IDT 2 to IDT 1) and across the membrane (IDT 2 to IDT 3), respectively. In both cases, the fundamental SAW mode is detected at $f_1 = 145$ MHz for a fundamental period of $\lambda_0 = 27.52 \mu\text{m}$ and at $f_2 = 292$ MHz, $f_3 = 436$ MHz and $f_4 = 582$ MHz for the harmonics. This result is already a positive indication that the wave is still propagating across the QD membrane even at higher frequencies, where the SAW is more sensitive to surface perturbations. A closer look at the measurement shows that the harmonics match in frequency for both delay lines even though the (Al)GaAs layer should act as an additional dispersive acoustic overlayer, which should impact the SAW velocity. Additionally, the magnitude of the transmission of the higher harmonics 3 and 4 is strongly reduced by the presence of the epilayer in the hybridised delay line compared to the free delay line. This can be intuitively explained by the additional mechanical losses of the wave introduced by the membrane. As the frequency increases and thus the wavelength decreases, the SAW is localised closer to the surface and is more sensitive to scattering at the edges of the membrane and to attenuation within the epilayer.

4.4 Optomechanical characterisation

To have a better understanding and to quantify the coupling of the SAW to the membrane, a full optomechanical characterisation was performed by detecting the spectral response of the QDs as a function of the frequency f_{rf} applied to IDT 2. When the SAW couples into the membrane, the QDs are strained by the mechanical wave and their emission spectrum is modulated by the deformation potential coupling [19, 21, 67]. In the time-integrated spectra measured here, this modulation leads to the observation of

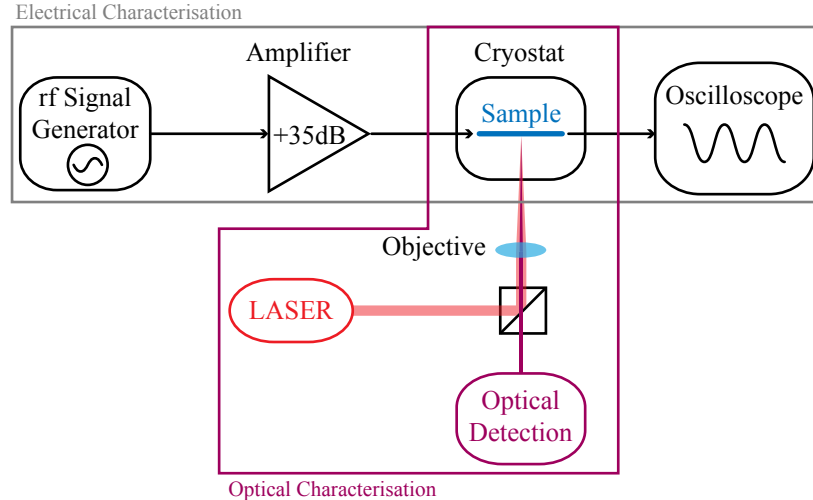


Figure 4.6: Schematic of the electrical setup that enables the simultaneous measurement of the transmitted power across the delay line with the optomechanical response of the QD’s emission.

a broadening of the emission line due to the modulation of the semiconductor’s bandgap by the hydrostatic pressure accompanying the wave [13]. Therefore, the broadening of the emission line scales linearly with the amplitude of the SAW so that this spectral broadening provides a direct measurement of the SAW amplitude or pressure at the dot’s position [68, 67]. Additionally, the Pd adhesion layer effectively short-circuits any electric field coming from the LiNbO_3 substrate and, therefore, the Stark effect modulation, which becomes dominant at high SAW amplitudes, is strongly suppressed [24, 68].

The setup used for the optomechanical measurements is schematically described in Figure 4.6. The optical measurement is performed in a conventional micro-photoluminescence ($\mu\text{-PL}$) setup and the sample is mounted in a liquid helium flow cryostat at 10 K. The QD is excited by an externally triggered pulsed diode laser at a wavelength of 660 nm and focused on the sample by a microscope objective to a diffraction limited spot of $\sim 1.5 \mu\text{m}$ diameter. The surface density of the QDs is $< 1 \mu\text{m}^{-2}$, which allows for the detection of individual QDs emission. The emission of individual QDs is then collected by the same objective, dispersed by a 0.5 m grating monochromator and detected by a liquid N_2 cooled silicon charge-coupled device (CCD). Because the laser pulse repetition rate is set to $f_{\text{laser}} \neq n \cdot f_{\text{rf}}$, the measured spectra are time-integrated spectra. More details on the optical setup are available in chapter 2. In parallel to the optical detection, the SAW transmission across the hybridised delay line (IDT 2 to IDT 3) is measured. The rf signal generator is used to apply rf pulses of a variable frequency f_{rf} at a constant power P_{rf} amplified to 28 dBm at IDT 2. The rf signal is modulated and the repetition rate of the modulation is fixed to 50 kHz with a ON/OFF duty cycle of 1:19. This modulation is optimised to suppress the spurious heating of the sample. The rf signal transmitted through the membrane is picked up by IDT 3 and detected in the time domain by a digital oscilloscope. The transmitted SAW signal

is quantified by a fast Fourier transform (FFT) analysis of the time domain signal and compared to the input power P_{rf} .

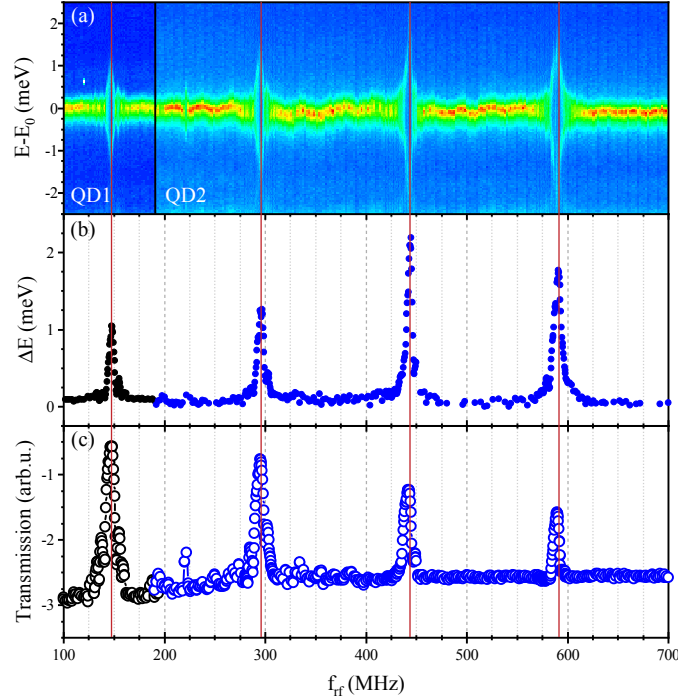


Figure 4.7: (a) False colour plot of the time-integrated emission line of two individual QDs as a function of the driving frequency f_{rf} covering all four harmonics of the Split-52 IDT. QD1 is measured from 100 to 190 MHz and QD2 from 190 to 700 MHz. (b) Spectral modulation (ΔE) due to the deformation potential coupling of QD1 and QD2 extracted through the fit of the spectrum. (c) SAW power transmission across the delay line through the QD membrane as a function of the driving frequency.

The result of such an optomechanical measurement is presented in Figure 4.7(a) for two QDs emission lines. The emission line of QD1 was measured for a range of frequencies close to the fundamental resonance of the IDT, $100 \leq f_{rf} \leq 190$ MHz, and the emission of QD2 was measured across the rest of the frequency range of the IDT, $190 \leq f_{rf} \leq 700$ MHz. The emission intensity is plotted in a false-colour representation as a function of the relative photon energy ($E - E_0$) and the applied rf frequency f_{rf} . It is clear that when the IDT is driven at a frequency far from one of its resonances, the IDT reflects the electrical input power and no SAW is generated on the sample. The emission line is unperturbed and maintains its lorentzian form. As the driving frequency approaches one of the resonances, a larger fraction of the input power P_{rf} is converted to a SAW and the emission line broadens and reaches a maximum at the resonance of the IDT. The four harmonics can be clearly seen in the QDs emission at $f_1 = 148$ MHz, $f_2 = 297$ MHz, $f_3 = 444.5$ MHz and $f_4 = 591$ MHz. The resonances are shifted towards higher frequencies compared to the one measured in Figure 4.5 due to an increase of the SAW's phase velocity at low temperatures.

To quantify the measured optomechanical response, the data is fitted by the follow-

ing function:

$$I(E) = I_0 + f_{rf} \frac{2A}{\pi} \int_0^{1/f_{rf}} \frac{w}{4 \cdot (E - (E_0 + \Delta E \cdot \sin(2\pi \cdot f_{rf} \cdot t)))^2 + w^2} dt \quad (4.1)$$

This function corresponds to a time-integrated spectrum of a Lorentzian line of constant width (w) and amplitude (A), whose centre emission energy (E_0) is sinusoidally modulated in time with an amplitude ΔE . The result of this fit is presented in Figure 4.7(b) for the whole frequency range, the black symbols correspond to the modulation of QD1 and the blue symbols to QD2. Additionally, the transmission across the delay line is plotted in Figure 4.7(c). The data is plotted as black and blue circles and is recorded simultaneously with the optical data from QD1 and QD2, respectively. The observed transmission peaks faithfully reproduce the maxima of the dynamic spectral broadening of the QD emission lines in the optical data, which is highlighted by the red lines across the plots. Just like in the room temperature VNA characterisation in Figure 4.5, the amplitude of the transmission decreases with the increasing frequency. This is once again expected due to increased scattering losses at the edges of the (Al)GaAs membrane. With the increased frequency, the wavelength of the SAW decreases and the deformation is localised closer to the surface. The wave becomes then much more sensitive to any perturbation of the surface of the LiNbO₃ substrate. However, this trend is not followed by the amplitude of the QD emission line modulation ΔE plotted in Figure 4.7(b). The modulation actually increases with f_{rf} with only a slight decrease for the highest resonance at f_4 .

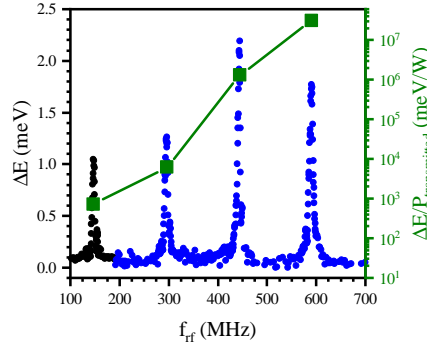


Figure 4.8: Spectral modulation (ΔE) due to the deformation potential coupling of QD1 and QD2 extracted through the fit of the spectrum and its peak value divided by the power transmitted at this point as a function of the driving frequency f_{rf} .

This interesting observation is even more highlighted when the maximum of the spectral broadening extracted from the plot is divided by the transmitted acoustic power in units of W, $\Delta E/P_{transmitted}$. This data is plotted in Figure 4.8 on a semilogarithmic scale with ΔE as a reference. This way, the reduction of the acoustic power detected at IDT 3 can be taken into account. The obtained $\Delta E/P_{transmitted}$ shows a strong increase of the coupling efficiency of the SAW to the QD with the increasing frequency. This observation confirms the analysis performed using the FEM simulations. Additionally,

this is extremely promising for the future of such hybrid devices as it is a first proof that the coupling between SAW and QDs can be increased by transferring them onto a strong piezoelectric substrate such as LiNbO_3 .

Conclusion

In conclusion, the finite element simulation of $(\text{Al})\text{GaAs-LiNbO}_3$ hybrid structures showed the localisation of the acoustic field inside the semiconductor membrane with increasing SAW frequencies. The FEM modelling predicted a large optomechanical coupling parameter $\gamma_{OM} > 25 \text{ meV nm}^{-1}$ for thin membranes at SAW frequencies $f_{SAW} \approx 3 \text{ GHz}$. Furthermore, we fabricated a LiNbO_3 - $(\text{Al})\text{GaAs}$ hybrid device and proved the successful coupling of the acoustic field inside the semiconductor membrane. The SAW excited on the LiNbO_3 substrate can be detected by the second IDT of the delay line across the membrane. Additionally, the simultaneous measurement of the QD's optomechanical response showed an enhancement of the QD's coupling to the acoustic field for increasing frequencies. The observation of the enhanced optomechanical coupling of the dots to the acoustic field in our hybrid device is a successful first step towards the design and fabrication of more complex opto-acoustic systems.

Quantum Dots and Surface Acoustic Wave Resonators

Additionally to the transfer of the QD membrane on a strong piezoelectric substrate, we want to increase the sound-matter coupling further by confining the acoustic field modulating the QDs. For this purpose, the epitaxial membrane is embedded in a SAW resonator cavity. In this chapter, the resonator is characterised by the quality factor of its cavity before and after the transfer of the (Al)GaAs epilayer. The coupling of the QDs to the phononic modes of the SAW cavity is analysed and the clear existence of standing waves through the localisation-specific response of the QDs is shown. QDs positioned in the centre of the cavity are also shown to react to either odd or even index number modes f_n and additionally to the combination of neighbouring modes $\frac{f_{(n+1)}+f_n}{2}$. This indicates the possibility of frequency mixing in two-phonons events by QDs inside the cavity. This complex behaviour of the phonon-QD coupling is further highlighted by the dependence of the QD response amplitude to the applied rf power P_{rf} . Finite element method simulation is used to determine that the origin of this complex behaviour is indeed not the classical linear deformation potential coupling.

The main results of this chapter were published in the Applied Physics Letters under the title "A hybrid (Al)GaAs-LiNbO₃ surface acoustic wave resonator for cavity quantum dot optomechanics" [69].

5.1 Samples geometry

The samples presented in this chapter were prepared using the epitaxial lift-off technique described in Chapter 3. A microscope image of the two final devices, resonators R1 and R2, are shown in Figure 5.1. The SAW-resonators are patterned by E-beam lithography onto an oxygen-reduced 128° rotated Y-cut LiNbO_(3-x) substrate. The SAW cavity is defined by two acoustic Bragg-reflectors made of metallic electrodes, short-circuited in the case of R1 and floating in the case of R2. The difference between both reflector geometries is explained in Chapter 1. The resonator is aligned along the X-direction of the crystal which is indicated in Figure 5.1(a). Apart from the electrical connection of

the electrodes in the Bragg reflector, the two resonators are nominally identical, with the same aperture $A = 350 \mu\text{m}$, mirror separation $d = 4522 \mu\text{m}$ and number of fingers in the reflectors $N_r = 150$. The nominal acoustic design wavelength and frequency are chosen to be $\bar{\lambda}_n = 13.3 \mu\text{m}$ and $\bar{f}_n = 300 \text{ MHz}$ for both devices. The electrodes inside the Bragg reflector are therefore separated by a pitch $p = \bar{\lambda}_n/2 = 6.65 \mu\text{m}$ and have a width of $a = \bar{\lambda}_n/4 = 3.325 \mu\text{m}$ for a chosen metallisation ratio $a/p = 1/2$. The SAW inside the cavities is excited by applying an electrical rf signal of frequency f_{rf} and power P_{rf} to a split-1 IDT containing 41 fingers (N_{IDT}) and having the same pitch and metallisation ratio as the reflectors. The IDT is patterned in the same lithographic step as the Bragg mirrors with a Ti (5 nm)/Al (50 nm) metallisation and placed close to one of the Bragg mirrors. The design parameters of both resonators are summarised in table 5.1.

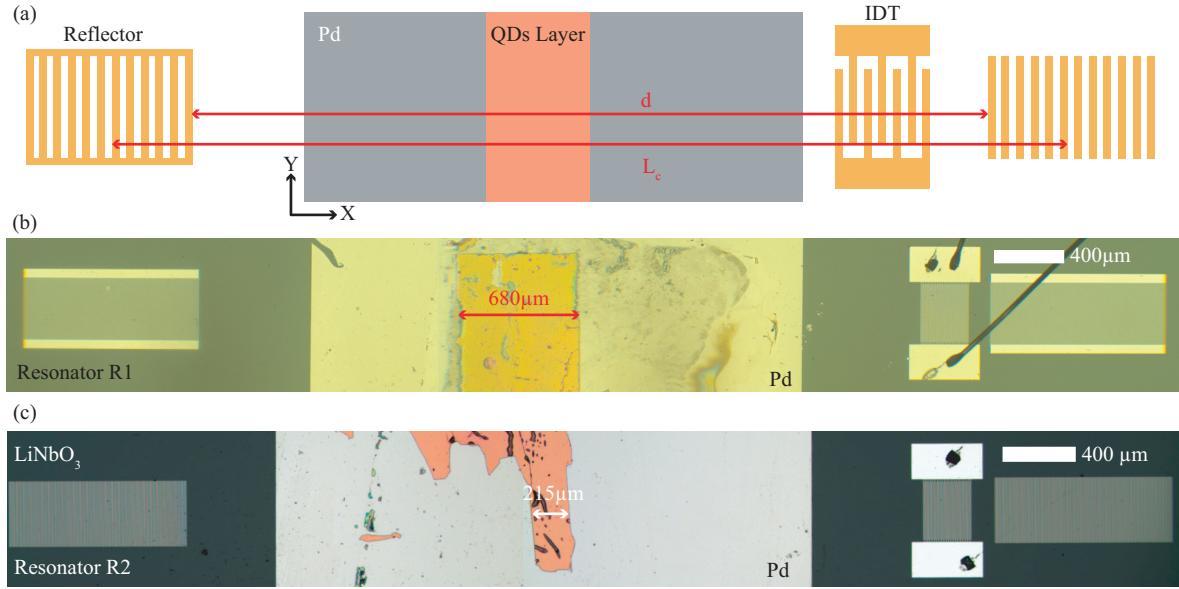


Figure 5.1: (a) Schematic depiction of the devices showing the two Bragg reflectors defining the SAW cavity and enclosing the IDT, Pd adhesion layer and the semiconductor layer. (b) and (c) Microscope pictures of the two resonators R1 and R2, respectively.

A	N_r	a	d	\bar{f}_n	$\bar{\lambda}_n$	N_{IDT}
$350 \mu\text{m}$	150	$3.325 \mu\text{m}$	$4522 \mu\text{m}$	300 MHz	$13.3 \mu\text{m}$	41

Table 5.1: Design parameters for the resonators R1 and R2.

Following a first characterisation of the resonators using a vector network analyser, the heterointegration of a QD membrane in each device is done using the epitaxial lift-off and transfer technique followed by an etching of the membrane described in chapter 3. The same GaAs QDs wafer as in chapter 4 is used. As a reminder, this semiconductor membrane was grown by molecular beam epitaxy on top of a $1 \mu\text{m}$ -thick $\text{Al}_{0.75}\text{Ga}_{0.25}\text{As}$

sacrificial layer. The 150 nm-thick membrane consists of a 140 nm $\text{Al}_{0.33}\text{Ga}_{0.67}\text{As}$ layer passivated by two 5 nm-thick GaAs layers on each side. In the centre of this membrane, a layer of GaAs QDs was fabricated by the droplet etching and filling technique explained in chapter 3 [54]. This wafer was grown by our collaborators in Linz. The epitaxial lift-off and transfer of the (Al)GaAs structure was performed by selectively etching the sacrificial layer in a dilute HF solution [23, 22, 70, 51]. The membrane was subsequently transferred onto the Pd adhesion layer where a strong mechanical bond forms at the interface between the metal and the III-V semiconductor as already explained previously [64]. The (Al)GaAs membrane is subsequently patterned to a rectangular form by wet chemical etching in order to avoid unwanted reflection and scattering of the SAW at the edges of the membrane and ensure a constant interaction length between the SAW and the membrane. A microscope image of the final devices is shown in Figure 5.1. It shows that the central part of the resonator is covered by a 3 mm long Pd adhesion layer with the epilayer on top of it and close to the centre of the cavity with a length of 700 μm and 215 μm for resonator R1 and R2, respectively. The length of the Pd layer, and consequently the length of the resonator cavity, was chosen to facilitate the transfer of the (Al)GaAs membrane after the epitaxial lift-off.

5.2 Electrical characterisation

The rf characterisation of the resonators was done by measuring the reflected signal emitted by the IDT inside the resonator using a vector network analyser at room temperature. In Figure 5.2(a), the modification in the reflection spectrum between the isolated IDT, in red, and the same IDT inside a SAW-cavity, in black, is presented. The IDT exhibits a broad reflection spectrum, emitting SAW in a wide frequency range. This is a direct result of its geometry and its small number of fingers as described by the discrete source model discussed in Chapter 1.

When the IDT is embedded inside the cavity, resonator modes are clearly resolved in the frequency range of the first stop band of the Bragg reflector, indicated by the grey rectangle in Figure 5.2(a). As shown in Chapter 1 Equation 1.25, the first stop band of the reflector is given by $\Delta f_{SB1} = 2f_{c1}|r_s|/\pi$, with $f_{c1} = v_{SAW}/(2p)$ being the centre frequency of the first stop band and p the pitch of the electrodes in the Bragg reflector [25, 6]. The centre frequency for both resonator is the designed to be the same at 300 MHz with $v_{SAW} = 3990 \text{ m s}^{-1}$ at low temperature. However, their stop bands differ from one another because of the connection of the electrodes in the reflectors which impacts the value of the reflection coefficient of the electrodes r_s as exemplified by the data in Table 1.2 and Equations 1.32 and 1.33 in Chapter 1. For the close-circuited electrodes in resonator R1, the mechanical contribution and electrical contribution to the reflection coefficient have opposite phase and thus its value is reduced to $|r_s| = |-0.02 + 0.8 \cdot (h/\lambda_0)| = 0.02 - 0.8 \cdot (50 \text{ nm}/13.3 \mu\text{m}) = 0.017$. The stop band is equal to $\Delta f_{SB1} = 2 \cdot 300 \cdot 0.017/\pi = 3.25 \text{ MHz}$. In the case of floating electrodes in resonator R2, the mechanical and electrical contributions are in phase and the reflection coefficient equals $|r_s| = |0.02 + 0.8 \cdot (h/\lambda_0)| = 0.02 + 0.8 \cdot (50 \text{ nm}/13.3 \mu\text{m}) = 0.023$. This results in a stop band equal to $\Delta f_{SB1} = 2 \cdot 300 \cdot 0.023/\pi = 4.39 \text{ MHz}$.

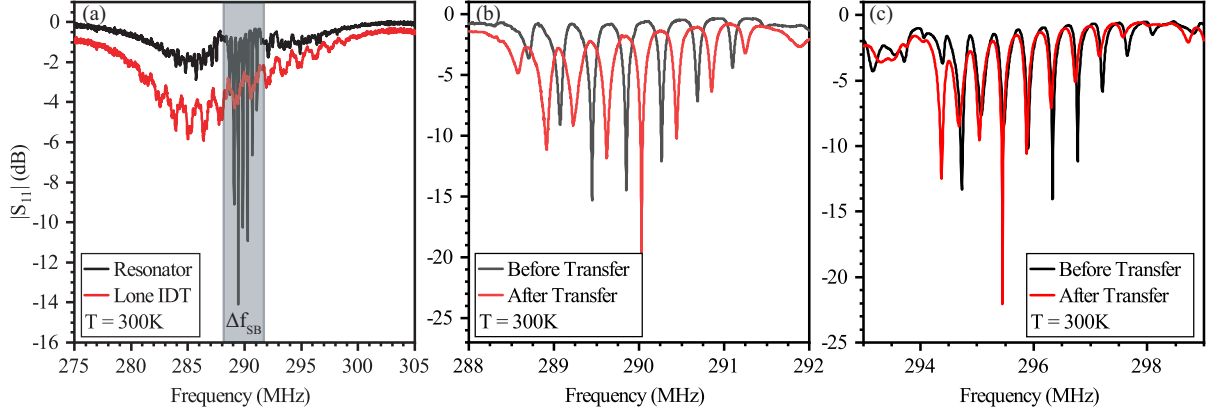


Figure 5.2: Reflected rf power $|S_{11}|$ at room temperature (a) for the isolated IDT (red line) and the IDT inside resonator R1 (black line), the stop band of the reflectors is indicated by the grey rectangle, (b) for the resonator R1 before (black line) and after (red line) transfer of the semiconductor membrane and (c) for the resonator R2 before (black line) and after (red line) transfer of the semiconductor membrane.

The effective length of the cavity for each resonator is also affected by the variation in the electrode reflection coefficient. The penetration length of the acoustic field into the mirror is given by $L_p = a/|r_s|$, where a is the width of the electrodes, which amounts to $196\ \mu\text{m}$ for R1 and $145\ \mu\text{m}$ for R2. The effective cavity length is then $L_c = d + 2 \cdot L_p$ and gives $4914\ \mu\text{m}$ for R1 and $4812\ \mu\text{m}$ for R2. The free spectral range (FSR) of the cavity modes can be derived from these values $FSR = v_{SAW}/(2L_c)$ and is equal to $406\ \text{kHz}$ for R1 and $415\ \text{kHz}$ for R2. Since the FSR is smaller than the width of the stop band of the reflectors, each resonator exhibits multiple modes as seen in Figure 5.2.

The pronounced phononics modes shown in Figures 5.2 (b) and (c) are present before and after the transfer of the epilayer and seem to conserve their quality factor even with the perturbation of the membrane. However, their number do vary. In the case of resonator R1, in Figure 5.2(b), 7 modes are clearly resolved before the transfer of the epilayer and their number increases to 8 after transfer. For resonator R2, in Figure 5.2(c), the number of modes changes from 9 to 8 after the epitaxial lift-off and transfer. To quantify the quality of the resonator modes, the complex response S_{11} of the resonators is fitted with a complex formula established by Manenti et al. [6, 7]. There, each SAW resonator mode is modelled like a resonant RLC circuit and is fitted by the following equation:

$$S_{11}(f) = \frac{(Q_e - Q_{i,n})/Q_e + 2iQ_{i,n} \cdot (f - f_{0,n})/f}{(Q_e + Q_{i,n})/Q_e + 2iQ_{i,n} \cdot (f - f_{0,n})/f} \quad (5.1)$$

where $Q_{i,n}$ and $Q_{e,n}$ denote the internal and external quality factor of mode n and its coupling to the external circuit, respectively. $f_{0,n}$ is the resonance frequency of the n -th mode. The fit of one of the modes is displayed in Figure 5.3. Each mode of the resonators reflection spectrum is fitted independently by fitting their real and imaginary parts with the ones of the function as displayed in Figure 5.3(a). The resulting fit of

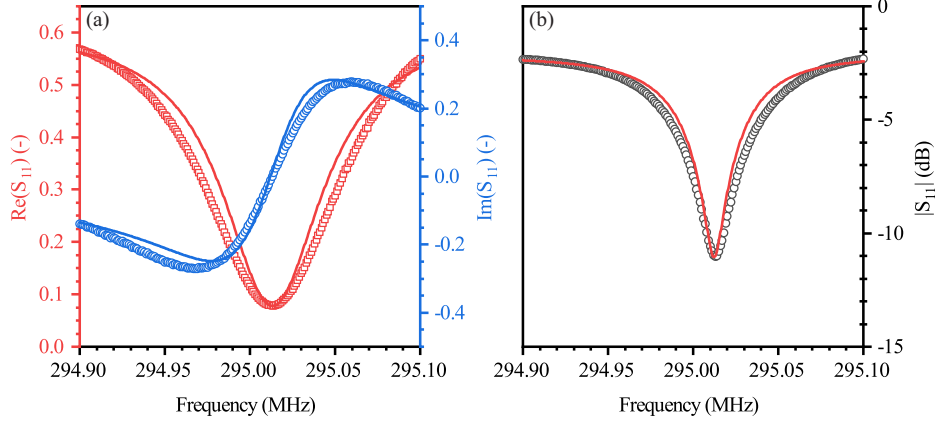


Figure 5.3: Example of the complex fit of the scattering parameter S_{11} for one mode of the resonator. (a) Fit of the real part (red) and imaginary part (blue) of the complex scattering parameter S_{11} . (b) Fit of the magnitude of the complex scattering parameter S_{11} in dB.

the magnitude is displayed in Figure 5.3(b) in the decibel scale, typically used to plot the complex scattering parameter S_{11} . The key parameters obtained from the fits are summarised in Table 5.2 for resonator R1 and in Table 5.3 for resonator R2. This includes the absolute mode index n_{abs} , the centre frequency of each mode f_n , the internal quality factor $Q_{i,n}$ and the frequency difference between the modes $\Delta f = f_{n+1} - f_n$.

Resonator R1 has a mean $\bar{Q}_i = 3800 \pm 1300$ and $\bar{f}_n = 290$ MHz. The given values are the mean of the distribution and their standard deviation from the mean calculated from the values in Table 5.2. Before transfer, the modes in resonator R1 are separated by a free spectral range $FSR_{empty} = 407 \pm 19$ kHz, which corresponds to a cavity round trip time $T_c = \frac{1}{FSR} = 2.46 \pm 0.11$ μs and a cavity length $L_c = \frac{v_{SAW}}{2FSR} = 4900 \pm 23$ μm . All of these values agree well with the theoretical ones calculated in the previous paragraph. After the heterointegration of the QD membrane in the centre of the cavity, the centre frequency remains constant at $\bar{f}_n = 290$ MHz. Mainly, the perturbation results in the reduction of the free spectral range to $FSR_{hybrid} = 392 \pm 32$ kHz, which translates in an increase of the cavity round trip time to $T_{c,hybrid} = 2.55 \pm 0.21$ μs and therefore an additional time of $\Delta T_c \simeq 90$ ns. More importantly, the internal quality factors remain high with $\bar{Q}_i = 3000 \pm 1300$, which is of highest relevance for strong phonon-exciton coupling. These changes can be reproduced by using the SAW velocity calculated by finite element modelling in Chapter 4. From the FEM simulation, we obtain a phase velocity at $f_{SAW} = 300$ MHz of $v_{SAW,LNO} = 3990$ m s^{-1} on bare LiNbO_3 which is in agreement with the literature [25, 26, 28]. By short-circuiting the surface with the Pd layer and adding the (Al)GaAs heterostructure, which is an acoustically slow material, the phase velocity reduces to $v_{SAW,LNO+Pd} = 3830$ m s^{-1} and $v_{SAW,LNO+Pd+(Al)GaAs} = 3800$ m s^{-1} in the Pd-coated and fully heterointegrated regions, respectively. Based on these calculated phase velocities, the cavity round trip time is given by

$$T_c = 2 \cdot \frac{4900 \pm 23 \mu\text{m}}{3990 \text{ m s}^{-1}} = 2.47 \pm 0.012 \mu\text{s}$$

Bare SAW resonator before ELO and transfer of the QD membrane								
n	1	2	3	4	5	6	7	
n_{abs}	709	710	711	712	713	714	715	
f_n (MHz)	288.66	289.03	289.43	289.84	290.26	290.69	291.1	
$Q_{i,n}$	2116	2404	3044	3784	4651	4860	5618	
Δf (MHz)	0.375	0.394	0.417	0.421	0.422	0.414		
Hybrid SAW resonator after ELO and transfer of the QD membrane								
n	1	2	3	4	5	6	7	8
n_{abs}	728	729	730	731	732	733	734	735
f_n (MHz)	288.51	288.83	289.21	289.62	290.04	290.45	290.86	291.25
$Q_{i,n}$	1481	1712	2187	2745	3119	3863	4174	5056
Δf (MHz)	0.324	0.383	0.411	0.415	0.409	0.410	0.391	

Table 5.2: Table summarising the key fit parameters f_n , $Q_{i,n}$ and $\Delta f = f_{n+1} - f_n$ for the electrical spectrum of the SAW resonator R1 before and after the heterointegration of the QD membrane in the SAW cavity.

for the bare resonator and, for the heterointegrated resonator, we obtain

$$T_{c,hybrid} = 2 \cdot \left(\frac{(4900 \pm 23 - 3000) \mu\text{m}}{3990 \text{ m s}^{-1}} + \left(\frac{(3000 - 680) \mu\text{m}}{3830 \text{ m s}^{-1}} \right)_{\text{Pd}} + \left(\frac{680 \mu\text{m}}{3800 \text{ m s}^{-1}} \right)_{\text{Full Stack}} \right) = 2.52 \pm 0.012 \mu\text{s}$$

yielding a change of $\Delta T_c \simeq 50$ ns. All the calculated values are close to and in the range of the error found for the experimental data. Furthermore, the reduction of the effective phase velocity in the hybridized region gives rise to a spectral shift of the mode spectrum of $\Delta f_n = 10.4$ MHz to lower frequencies. According to these calculations, the absolute mode index then changes from $n_{abs} = n + 708$ for the bare resonator to $n_{abs,eff} = n + 727$, for the hybrid device. These mode numbers are summarized in table 5.3.

The same analysis is performed for resonator R2, and we find a mean $\bar{Q}_i = 2900 \pm 700$ MHz and $\bar{f}_n = 296$ MHz at room temperature. It seems like the average quality factor of resonator R1 is larger than the one of resonator R2, but, in view of the large standard deviation, it is safe to assume that both resonators have a similar cavity quality factor. The shift of the centre frequency could be attributed to variations in the fabrication parameters but also to the connection of the electrodes in the Bragg mirrors which leads to another cavity length and other resonant frequencies. Before transfer, the free spectral range amounts to $FSR_{empty} = 415 \pm 27$ kHz and corresponding to a cavity round trip time $T_c = 2.41 \pm 0.16 \mu\text{s}$ and a cavity length $L_c = \frac{v_{SAW}}{2FSR} = 4800 \pm 31 \mu\text{m}$. Once again, all of these values agree well with the theoretical ones calculated previously with a theoretical cavity length $L_c = 4812 \mu\text{m}$ and $FSR = 415$ kHz.

Bare SAW resonator before ELO and transfer of the QD membrane					
n	1	2	3	4	5
n_{abs}	708	709	710	711	712
f_n (MHz)	294.4	294.76	295.14	295.56	295.99
$Q_{i,n}$	4705	2412	2469	2310	2827
Δf (MHz)	0.358	0.387	0.421	0.424	0.432
n	6	7	8	9	
n_{abs}	713	714	715	716	
f_n (MHz)	296.42	296.85	297.28	297.71	
$Q_{i,n}$	2781	2939	2897	2727	
Δf (MHz)	0.429	0.431	0.434		
Hybrid SAW resonator after ELO and transfer of the QD membrane					
n	1	2	3	4	5
n_{abs}	727	728	729	730	731
f_n (MHz)	294.38	294.74	295.13	295.54	295.96
$Q_{i,n}$	2302	1979	2291	2483	2666
Δf (MHz)	0.359	0.398	0.409	0.419	0.423
n	6	7	8		
n_{abs}	732	733	734		
f_n (MHz)	296.39	296.81	297.22		
$Q_{i,n}$	2700	2694	2840		
Δf (MHz)	0.419	0.414			

Table 5.3: Table summarising the key fit parameters f_n , $Q_{i,n}$ and $\Delta f = f_{n+1} - f_n$ for the electrical spectrum of the SAW resonator R2 before and after the heterointegration of the QD membrane in the SAW cavity.

After the transfer of the QD membrane, the centre frequency remains approximately constant at $\bar{f}_n = 295.8$ MHz, and the free spectral range is reduced to $FSR_{hybrid} = 406 \pm 22$ kHz. The cavity round trip time increases to $T_{c,hybrid} = 2.46 \pm 0.13$ μ s, resulting in a time difference between the two round trip of $\Delta T_c \simeq 50$ ns. The internal quality factors remain high with $\bar{Q}_i = 2500 \pm 300$. Again, these changes can be reproduced by using finite element modelling and the same phase velocities as for resonator R1. In this case, the hybrid layer has a width $w_{hybrid} = 215$ μ m, and the cavity round trip time is given by

$$T_c = 2 \cdot \frac{4800 \pm 31 \text{ } \mu\text{m}}{3990 \text{ m s}^{-1}} = 2.41 \pm 0.016 \text{ } \mu\text{s}$$

for the bare resonator and, for the heterointegrated resonator, we have

$$T_{c,hybrid} = 2 \cdot \left(\frac{(4800 \pm 31 - 3000) \mu\text{m}}{3990 \text{ m s}^{-1}} + \left(\frac{(3000 - 215) \mu\text{m}}{3830 \text{ m s}^{-1}} \right)_{\text{Pd}} + \left(\frac{215 \mu\text{m}}{3800 \text{ m s}^{-1}} \right)_{\text{Full Stack}} \right) = 2.47 \pm 0.016 \mu\text{s}$$

and we find that $\Delta T_c \simeq 60$ ns. All the calculated values are once again comparable to the experimentally determined ones. The reduction of the effective phase velocity in the hybridized region causes a spectral shift of the mode spectrum of $\Delta f_n = 10.5$ MHz to lower frequencies. According to these calculations, the absolute mode index then changes from $n_{abs} = n + 707$ of the bare resonator to $n_{abs,eff} = n + 726$, for the hybrid device. These mode numbers and the other key parameters are summarised in table 5.3.

Similar considerations for the change of the phase velocity due to the contribution by the IDT inside the cavity could also be made but, since the resonator and the IDT are fabricated in a single step, an analogous analysis is not possible.

In conclusion, the electrical characterisation of the resonators at room temperature was used to study the impact of the heterointegration of the (Al)GaAs QD membrane inside two different cavities on their phononic properties. The change in FSR and effective SAW velocity are well reproduced by using the finite element modelling introduced in Chapter 4 and the quality factor of the cavity modes remained high after heterointegration. The latter is an important prerequisite to ensure strong coupling of the QDs to the phononic cavity.

5.3 Optomechanical characterisation

Next, we investigate the optomechanical coupling of single QDs to the phononic modes of the resonators. As discussed in Chapter 4, the dominant coupling mechanism is deformation potential coupling, i.e., the modulation of the semiconductor's bandgap by hydrostatic pressure or normal stress [13]. The Pd adhesion layer effectively short circuits any electric field induced in the LiNbO₃ substrate [51, 24]. Thus, Stark effect modulation, which becomes dominant at high SAW amplitudes [68], remains strongly suppressed. The optomechanical response is measured at low temperatures ($T = 10$ K) by time and phase averaged micro-photoluminescence spectroscopy [13].

The experimental setup is shown schematically in Figure 5.4. The optical part of the experiment (lower right part of Figure 5.4) is identical to the experimental setup used in Chapter 4 and described in more detail in Chapter 2. A repetition rate of 80 MHz is fixed for the pulsed diode laser with a wavelength 660 nm. In the studied frequency range or for the specific applied frequencies f_{rf} , the laser repetition rate and the electrical frequency are not commensurate, i.e. $f_{rf} \neq m \cdot 80$ MHz. Thus, the detected line shape is a time-average of the dynamic optomechanical modulation of the unperturbed Lorentzian QD emission line and the observed spectral broadening is a measurement of the amplitude of the optomechanical modulation [68, 51, 13]. The electrical part of the setup shown in Figure 5.4 allows to apply a rf voltage to

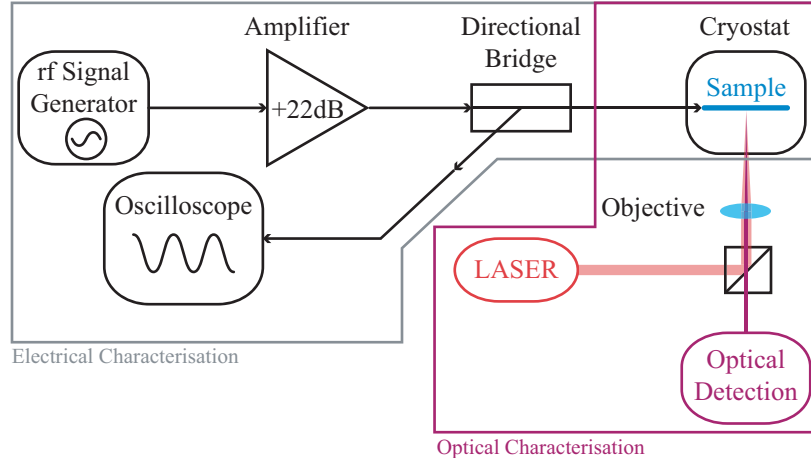


Figure 5.4: Schematic of the electrical and optical setup that enables the simultaneous measurement of the reflected power and the optomechanical response of the QD.

the IDT and to detect the reflected electrical power. To this end, the output of the rf signal generator is amplified and connected via a directional bridge to the sample inside the cryostat. The reflected electrical signal is sent from the directional bridge to an oscilloscope. Thus, the reflected power $P_{reflected}$ is measured simultaneously with the optomechanical modulation for any combination of electrical frequency (f_{rf}) and power (P_{rf}) and potential sources of errors such as temperature related drifts of the mode spectrum can be eliminated. Thanks to the confinement of the SAW in the cavity, lower rf powers were used compared to the experiments in Chapter 4. Therefore, the spurious heating of the sample by the SAW was low and the SAW and laser signals were not modulated but kept continuous.

5.3.1 Position dependent QD-resonator coupling and time-domain analysis

As a first characterisation, $P_{reflected}$ is measured and plotted as a function of f_{rf} in Figure 5.5 (a) and (d) for resonator R1 and R2, respectively. The rf frequency is then fixed to one of the modes of the resonator, highlighted by a red cross in the plots, $f_7 = 294.96$ MHz for resonator R1 and $f_5 = 300.25$ MHz for resonator R2, and the applied rf power is kept constant at $P_{rf} = 10$ dBm for R1 and $P_{rf} = 5$ dBm for R2. The position of the objective, and thus the position of the optical excitation and detection, is swept across the resonator axis X (see Figure 5.1(a)) using closed loop nano-positioning devices. At each step, a spectrum is taken with and without applying the SAW excitation. The measured spectra of two QDs detected during the measurement are presented in Figure 5.5 with (red) and without (black) SAW for each cavity.

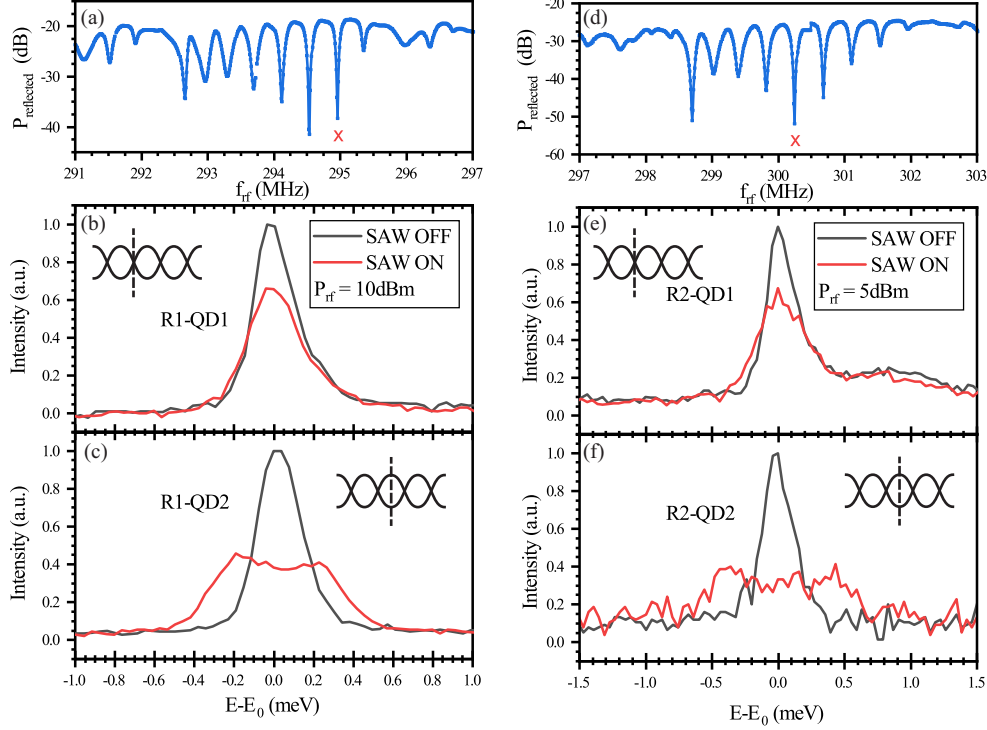


Figure 5.5: (a) Measured reflected power spectrum of the resonator R1. (b-c) Low temperature emission spectra of two QDs inside the SAW resonator R1 without (black lines) and with (red lines) $f_{\text{rf}} = 294.96$ MHz applied with $P_{\text{rf}} = 10$ dBm to the IDT. This applied frequency is resonant to the $n=7$ mode marked in the above measured reflected power spectrum of the resonator. QD1 (QD2) is located close to or at a node (an antinode) of the cavity field as shown by the schematic. (d) Measured reflected power spectrum of the resonator R2. (e-f) Low temperature emission spectra of two QDs inside the SAW resonator R1 without (black lines) and with (red lines) $f_{\text{rf}} = 300.25$ MHz applied with $P_{\text{rf}} = 5$ dBm to the IDT. This applied frequency is resonant to the $n=5$ mode marked in the above measured reflected power spectrum of the resonator. QD1 (QD2) is located close to or at a node (an antinode) of the cavity field as shown by the schematic.

R1-QD1 and R1-QD2 are separated by $\simeq 41 \mu\text{m} \simeq 3.1 \cdot \lambda_{\text{SAW}}$, whereas R2-QD1 and R2-QD2 are separated by $\simeq 21 \mu\text{m} \simeq 1.6 \cdot \lambda_{\text{SAW}}$ and, in both cases, the QDs exhibit completely dissimilar behaviour. While R1-QD2 (R2-QD2) shows a pronounced broadening when the SAW is generated, the line shape of R1-QD1 (R2-QD1), apart from a weak reduction of the overall intensity remains unaffected. These types of behaviours are expected for QDs positioned at an antinode (QD2) or node (QD1) of the acoustic cavity field. From the observed optomechanical responses, we infer that R1-QD1 (R2-QD1) and R1-QD2 (R2-QD2) are located at a node or antinode of the mode, respectively, as illustrated by the schematics in Figure 5.5. This shows that the position of the QD determinates its coupling to the modes of the resonator.

Next, we keep the laser position fixed, and the radio frequency f_{rf} is swept through a large range of frequencies, 275 – 315 MHz for R1 and 295 – 315 MHz for R2, at a

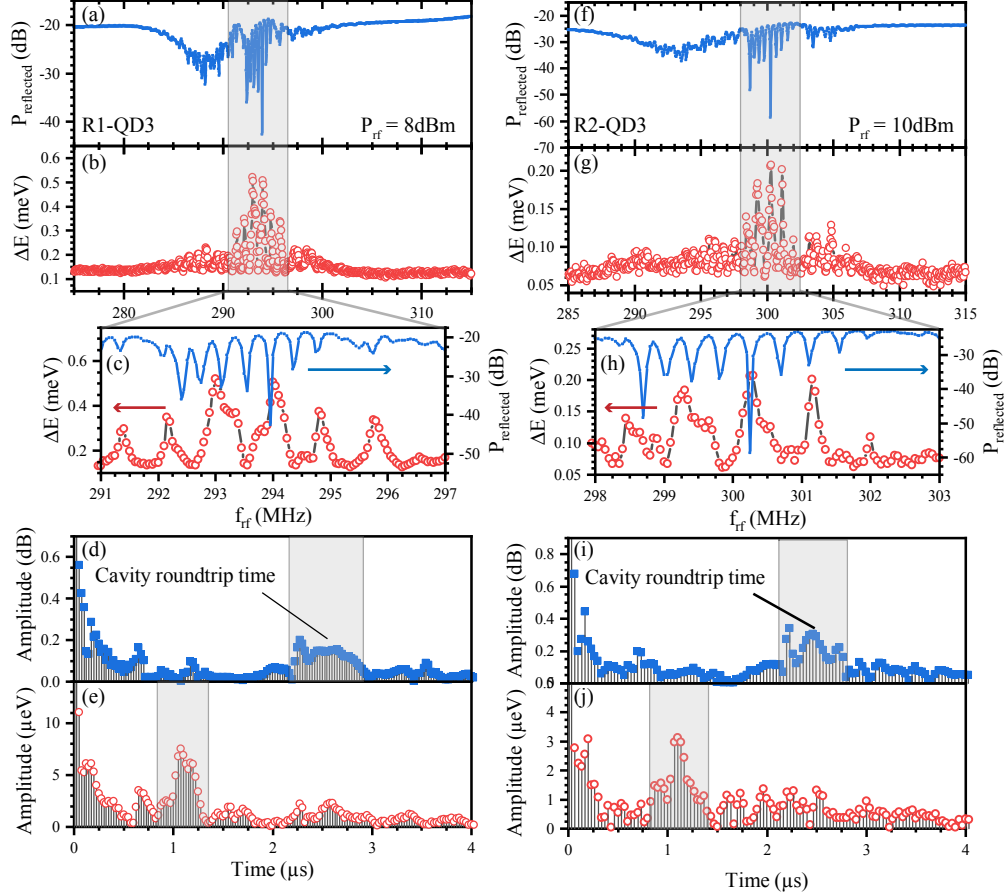


Figure 5.6: (a) Reflected power spectrum and (b) simultaneous optomechanical response of QD3 in resonator R1. (c) The same data plotted in the frequency range of the cavity modes (grey shaded area). (d, e) FFT of the data in (a) and (b) showing a clear signature at T_1 and $T_1/2$, respectively. (f) Reflected power spectrum and (g) simultaneous optomechanical response of QD3 in resonator R2. (h) The same data plotted in the frequency range of the cavity modes (grey shaded area). (i, j) FFT of the data in (f) and (g) showing a clear signature at T_2 and $T_2/2$, respectively.

constant power ($P_{rf} = 8$ dBm for R1 and $P_{rf} = 10$ dBm for R2), and the emission spectra of a single QD (R1/R2-QD3) is recorded. The data are fitted with the time-integrated modulated Lorentzian function presented in the previous chapter, Chapter 4 Equation 4.1. The important parameter ΔE , the optomechanical modulation amplitude due to the time-dependent deformation potential coupling, is plotted in Figure 5.6 (b) and (g) with the simultaneously measured reflected rf power in (a) and (f). In both cases, QD3 clearly exhibits a large optomechanical response at frequencies at which pronounced cavity modes are observed (grey shaded area). This pronounced coupling of the QDs to the resonator modes is a first direct evidence of cavity enhanced coupling between SAW phonons and the exciton transition of a single QD. However, the detected optomechanical response, $\Delta E(f_{rf})$ of R1/R2-QD3 exhibits noticeably less peaks than $P_{reflected}$, as illustrated by the zoom in plotted in Figures 5.6(c) and (h). Both optical

and electrical signals are fast Fourier transformed and plotted in Figure 5.6 (d), (e), (i) and (j) to obtain the time domain information from the measurement. A pronounced peak can be identified in the FFT of $P_{reflected}$ in (d) and (i) at $t = 2.55 \pm 0.025 \mu\text{s}$ for R1 and $t = 2.4 \pm 0.05 \mu\text{s}$ for R2. These times match exactly the cavity round trip time $T_1 = 2.62 \mu\text{s}$ (R1) and $T_2 = 2.48 \mu\text{s}$ (R2) derived from the measured FSR of the resonators. In contrast, the FFT of ΔE in (e) and (j) show a clear signal at $t = 1.1 \pm 0.025 \mu\text{s}$ for R1 and $t = 1.1 \pm 0.1 \mu\text{s}$ for R2, which corresponds to approximately the half of the cavity round trip time. This apparent halving of the round trip time, i.e., doubling of the FSR, in the dots' optomechanical response provides a first direct evidence that the coupling occurs only to every second cavity mode due to the localised nature of the QDs.

5.3.2 QD-resonator coupling

To investigate the mode index selective coupling in more detail, a more precise frequency sweep covering a smaller frequency span but with higher resolution is conducted to two different QDs inside the two resonators. These QDs are selected using the same method as for R1/R2-QD1 and 2 in Figure 5.5. The resonator X axis is swept and, for every QD along this axis, an optical spectrum is recorded with and without applying the SAW excitation fixed at the frequency of one of the modes. Once a QD reacting strongly to this mode is identified, its optomechanical response is investigated over the full frequency span and the coupling of the dot to the resonator's modes is studied. The results of the best fit of equation 4.1 for the SAW modulation ΔE are plotted in Figure 5.7 in the main panels as a function of the frequency shift relative to the centre mode $n = 5$.

As explained before, in the context of Figure 5.4, the magnitude of $P_{reflected}$ is measured simultaneously to the optomechanical modulation. It is plotted in the upper panels of Figure 5.7. From these electrical data, the quality factor of the resonators modes at low temperature can be extracted, $Q = \Delta f/f_0$. For resonator R1, we obtain a mean quality factor of $\bar{Q} = 3810 \pm 1480$ and, for resonator R2, $\bar{Q} = 4430 \pm 1560$. This corresponds to an increase of ≈ 1.25 for resonator R1 and ≈ 1.75 for resonator R2 compared to the room temperature values. From these numbers, the quality factor-frequency product ($Q \times f$) can be computed, which is an important Figure of merit commonly used to compare mechanical resonators [71]. Here, R1 possesses a quality factor-frequency product of $\bar{Q} \times f = (1.14 \pm 0.44) \cdot 10^{12}$ and R2 of $\bar{Q} \times f = (1.33 \pm 0.48) \cdot 10^{12}$. In the quantum realm, this product has to be compared to the thermal energy. Since, in our case, the SAW phonon energy of $\approx 1.25 \mu\text{eV}$ is less than $k_B T \approx 862 \mu\text{eV}$, the maximum number of coherent oscillations, i.e., number of coherent operations possible in this system, is limited by thermal decoherence and given by $Q \times f \times \frac{h}{k_B T}$ [72]. In our case, at $T = 10 \text{ K}$, the number of coherent oscillations is limited to $Q \times f \times \frac{h}{k_B T} \approx 6$ for both unloaded hybrid resonators and a single oscillation will be preserved even up to 50 K. These numbers prove the coherent nature of the SAW oscillation in our heterointegrated devices up to 50 K.

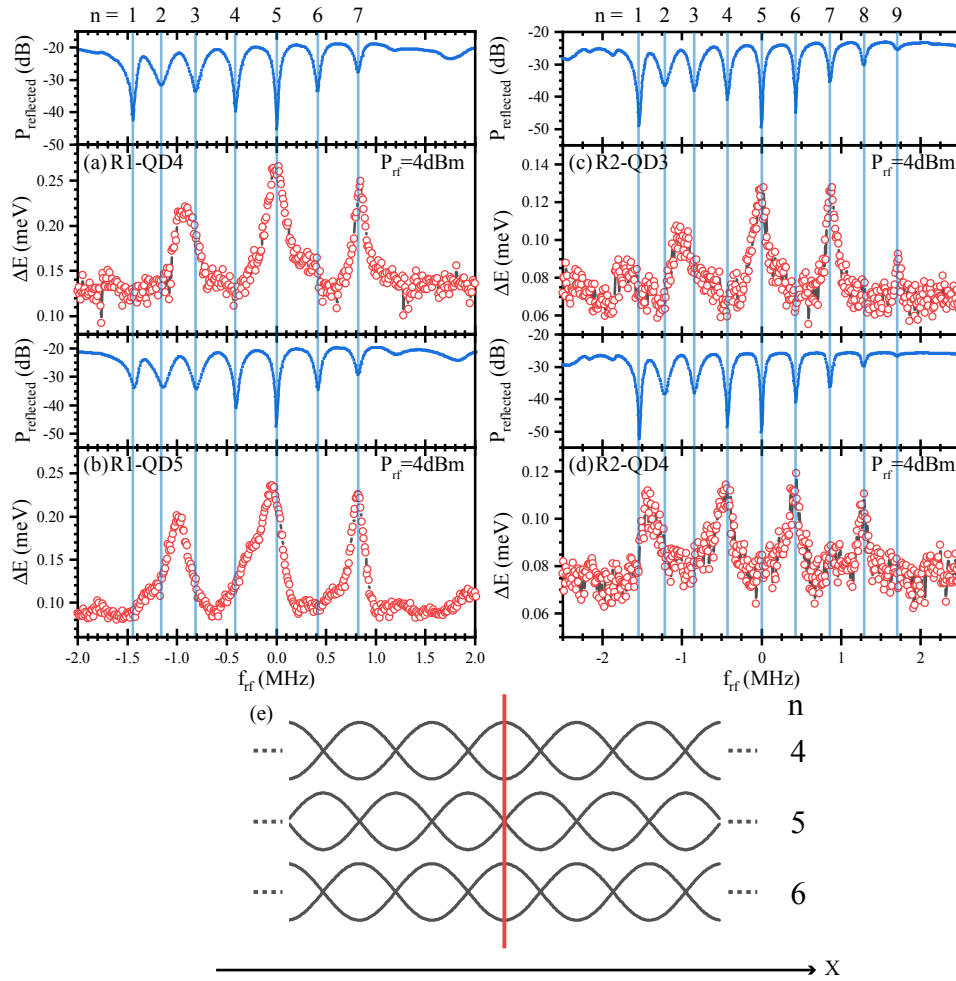


Figure 5.7: Frequency dependent optomechanical response of QD4 (a) and QD5 (b) in resonator R1 and QD3 (c) and QD4 (d) in resonator R2 measured at 10K. Upper panels: Reflected rf power. Main panels: Optomechanical response of the dots. (e) Schematic of the acoustic field in the centre of the resonator for the modes 4, 5 and 6 detected in the experimental data above.

Looking at the QDs optomechanical response, the quality factor of the resonances of the QDs to the modes decreases to a detected averaged quality factor of $\bar{Q}_{QD} = 1820 \pm 560$ for R1 and $\bar{Q}_{QD} = 1730 \pm 420$ for R2. This change in quality factor compared to the electrically detected one can be attributed to the formation of imperfections during the heterointegration of the epilayer, such as inhomogeneous bonding, surface roughness and misalignment of the etched edges. Taking a closer look at the spectra of QD4 and 5 in resonator R1 and QD3 in resonator R2 in Figure 5.7(a), (b) and (c), the strong optomechanical response is restricted to the modes with odd index number $n = 5, 7, 9$. In contrast, R2-QD4 couples to modes with an even index number $n = 4, 6, 8$, see Figure 5.7(d). The mode index selective coupling of the QDs can be explained by their relative position inside the SAW cavity. As shown in the schematic in Figure 5.7(e), odd and even index number modes have alternating nodes and antinodes

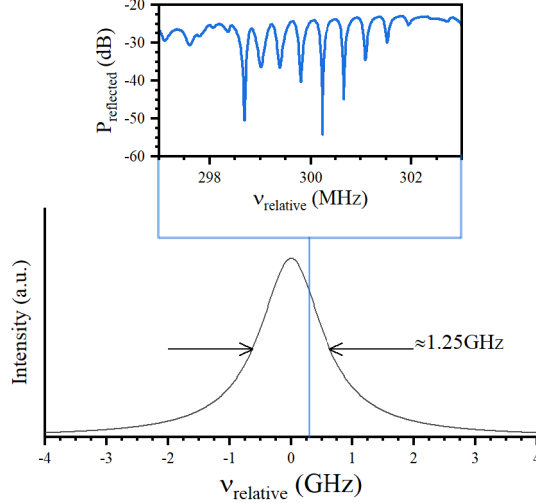


Figure 5.8: Schematic showing the linewidth of the measured QDs in comparison to the electrically measured phononic spectrum of the resonator.

at the centre of the cavity and this behaviour extends to several wavelengths away from the centre ($\lambda_0 \approx 13.3 \mu\text{m}$) due to the large index number of the modes in both resonator ($n + 727$ for R1 and $n + 726$ for R2). In both devices, the QDs membrane overlaps with the centre of the resonator. The measured quantum dots are positioned close to the cavity centre and are specifically selected for their strong optomechanical response to a specific mode with an odd or even index number. Therefore, we can assume that they are positioned on the antinode of this mode, e.g. a mode with an odd index number 5, and thus on the node of the adjacent modes, with even index numbers 4 and 6. The QD is then selectively coupled to modes with either an even or an odd mode index. This alternative behaviour also explains the half cavity round trip time observed in the FFT of the QDs response in Figure 5.6 since these central QDs spectra possess a FSR double the one of the electrical spectra.

This simple model applies to modes $n \geq 4$, but a more complex and unexpected behaviour is observed for modes $n \leq 3$. In the case of R1-QD4, R1-QD5 and R2-QD3 in Figure 5.7(a), (b) and (c), a strong optomechanical resonance is observed for a frequency $(f_3 + f_2)/2$ and not for f_1 and f_3 as could be expected. Similarly, R2-QD4 presents a resonance at $(f_2 + f_1)/2$ and not at f_2 in Figure 5.7(d). In the case of linear optomechanical coupling, these resonances should not appear in the QDs spectra and a response should only be detected when the driving rf-signal is in resonance with the frequency of the odd (R1-QD4, R1-QD5 and R2-QD3) or the even (R2-QD4) mode index. Additionally, when f_{rf} is detuned from the cavity resonances, no optomechanical response should be detected due to the cavity efficient reflection of the phonons injected by the IDT. Even if we consider a finite amount of acoustic power generated by the IDT in the form of propagating waves, the optomechanical response for those off-resonance frequencies should not be as pronounced as for rf frequencies in resonance with the modes of the resonators. This is not the case for the QDs presented in Figure 5.7 where the off-resonance optomechanical response is as strong as the in-resonance ones.

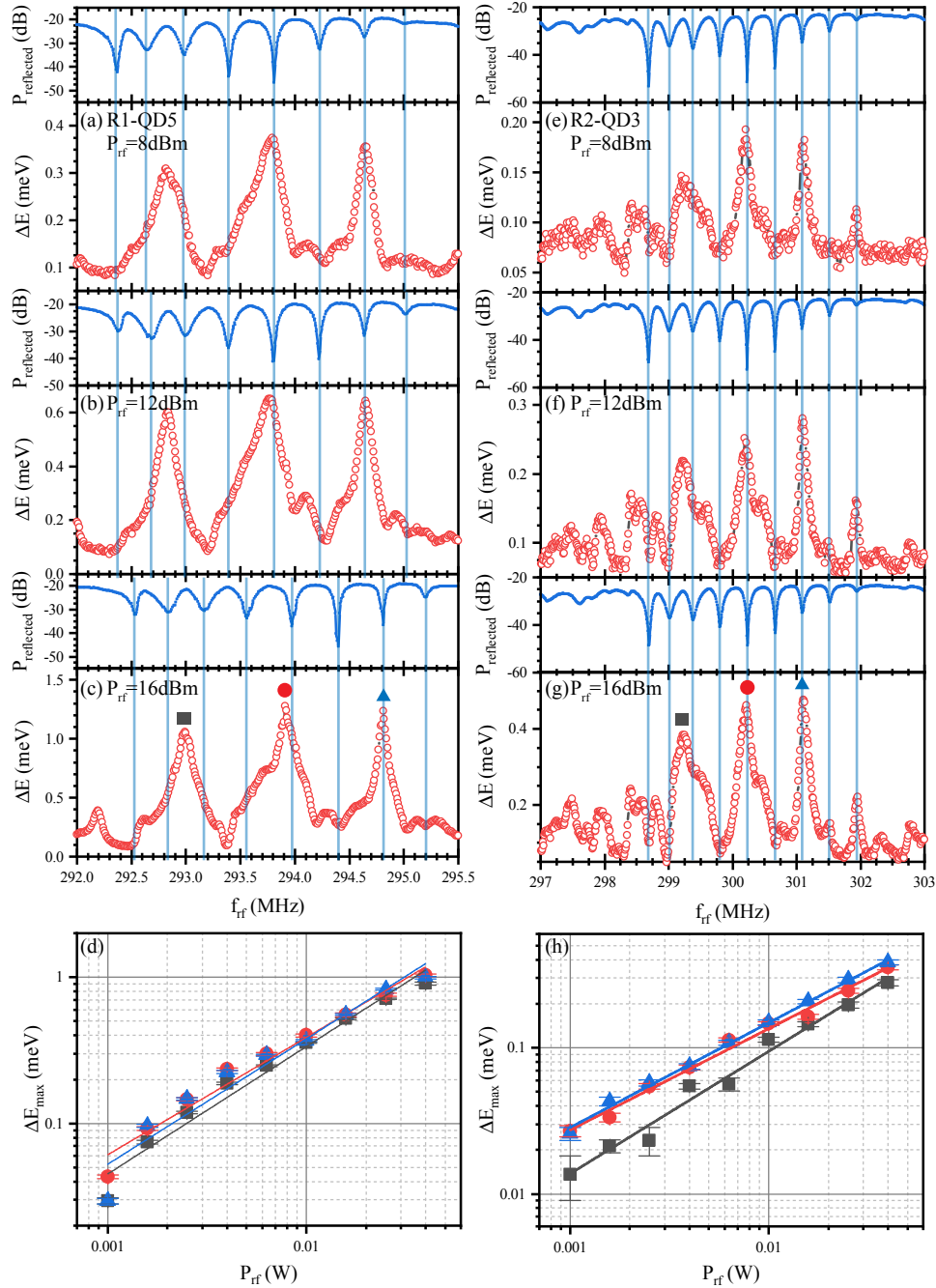


Figure 5.9: (a-c) Frequency dependent optomechanical response of QD5 in resonator R1 for three values of P_{rf} 8 (a), 12 (b) and 16 dBm (c). Upper panels: reflected rf power. Main panels: optomechanical response of the dots. (d) Amplitudes of three selected peaks (marked by the corresponding symbols in (c)) as a function of P_{rf} . (e-g) Frequency dependent optomechanical response of QD3 in resonator R2 for three values of P_{rf} 8 (a), 12 (b) and 16 dBm (c). Upper panels: reflected rf power. Main panels: optomechanical response of the dots. (h) Amplitudes of three selected peaks (marked by the corresponding symbols in (g)) as a function of P_{rf} .

These special features cannot arise from a simple linear coupling mediated by the deformation potential. Since this behaviour is observed for different QDs at different positions in the cavities and, in particular, in two different devices, we can exclude the possibility that this behaviour is caused e.g. by the presence of local imperfections in the membrane. However, one plausible explanation is non-linear frequency conversion. The optomechanical response is observed in the centre between two electrically detected modes and, therefore, this peak could arise from the conversion of two off-resonant phonons of the same frequency f_{OP} to two cavity phonons, the frequencies of which match the two adjacent modes f_n and f_{n+1} . We then have $2f_{OP} = f_n + f_{n+1}$. Due to the optical linewidth of the QD being at least three orders of magnitude larger than the FSR, this type of frequency mixing could be possible. Specifically, in the case of R1-QD4, R1-QD5 and R2-QD3, a possible frequency mixing process is the conversion of two SAW phonons with frequency $f_{OP} = (f_3 + f_2)/2$ to a pair of cavity phonons, the first of frequency $f_n = f_2$ and a second of frequency $f_{n+1} = f_3$. We are considering the plausibility of such processes due to the observation and demonstration in our group of the sum and difference frequency generation of two propagating SAW fields by a single QD in the resolved sideband regime [73]. In our system, the optical linewidth of the QD is $\Gamma_{QD} \sim 1.25$ GHz [74], which is one order of magnitude larger than the SAW frequency. Therefore, it fully covers the entire phononic mode spectrum as shown in Figure 5.8, where the entire resonator's phononic spectra can be reduced to a thin blue line inside the frequency spectrum of the QD. This confirms, that the frequency mixing between different f_n by the QD's optical transition could indeed be possible.

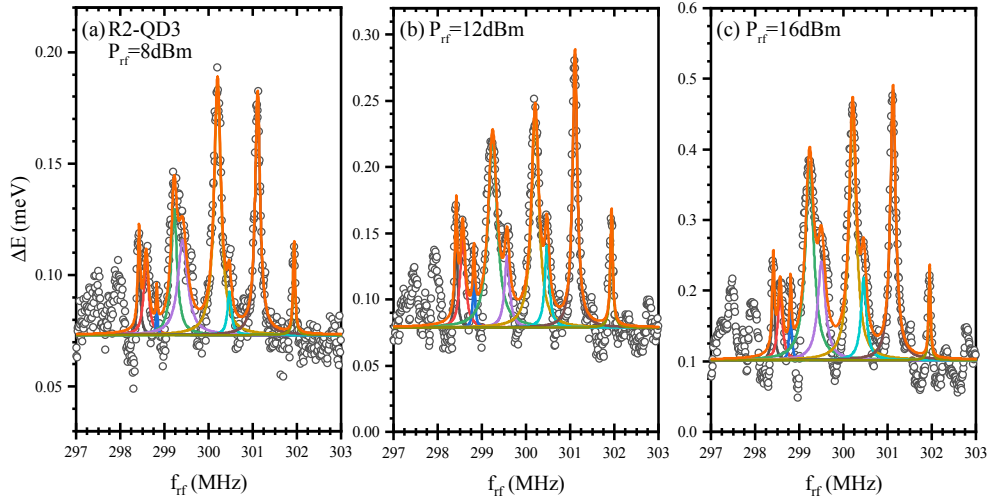


Figure 5.10: Frequency dependent optomechanical response of QD3 in resonator R2 for three values of P_{rf} 8 (a), 12 (b) and 16 dBm (c). The QD optomechanical response is fitted with a combination of several Lorentz peak functions. The amplitudes of the peaks are displayed in Figure 5.9 (h).

If the process behind the presence of frequency mixing peaks is indeed a two-phonon process, the optomechanical modulation of the quantum dot should have a quadratic dependence on the applied strain modulation amplitude which is proportional to $P_{rf}^{1/2}$.

Therefore, the optomechanical modulation should be proportional to P_{rf}^1 . To investigate this, the optomechanical response of R1-QD5 and R2-QD3 is measured for $P_{rf} = [0 : 2 : 16]$ dBm. The optomechanical spectra are plotted in Figure 5.9 (a-c) and (e-g) for three different P_{rf} , 8, 12 and 16 dBm. The simultaneously measured reflected power is plotted as a reference in the upper panels of the figure and does not show significant changes for different P_{rf} in the case of R2. On the other end, the electrical spectrum of R1 shows some pronounced changes. The two resonators were measured in two different cryostats and, thus, we assume that these changes are due to a possible grounding problem in this specific cryostat and not due to any backaction or transduction from the QD to the acoustic domain. As P_{rf} increases, the optomechanical modulation ΔE of the QDs increases. In addition, new features appear, which were not present at low power in Figure 5.7. For example, at 16 dBm in Figure 5.9(c) and (g), the spectrum of R1-QD5 presents side peaks at frequencies $(f_1 + f_2)/2$, $(f_4 + f_5)/2$ and $(f_6 + f_7)/2$, whereas R2-QD3 presents features at frequencies $(f_3 + f_4)/2$ and $(f_5 + f_6)/2$. Those features cannot be explained by a simple linear coupling mediated by the deformation potential.

To complete the analysis, the f_{rf} -scans were fitted for each P_{rf} as displayed in Figure 5.10 for R2-QD3 at three different powers, 8, 12 and 16 dBm. From the fits, it is easy to see the different features appearing with the increasing P_{rf} . The maximum of the optomechanical modulation ΔE_{max} is extracted from the fits for the three main peaks of the QDs spectra, $(f_3 + f_2)/2$ (black), f_5 (red) and f_7 (blue). Both data are plotted as symbols in a double logarithmic representation as a function of P_{rf} in Figure 5.9 (d) and (h) to identify the power law dependencies using the linear fits of the data present in the plots. For R1-QD5, $(f_3 + f_2)/2$ exhibits a power law dependence with a slope $m_1 = 0.87 \pm 0.1$ while f_5 has a slope $m_2 = 0.8 \pm 0.1$ and f_7 , $m_3 = 0.86 \pm 0.1$. In the case of R2-QD3, the slopes are $m_1 = 0.85 \pm 0.1$, $m_2 = 0.7 \pm 0.1$ and $m_3 = 0.75 \pm 0.1$ for $(f_3 + f_2)/2$, f_5 and f_7 , respectively. These exponents are greater than $\Delta E_{max} \propto P_{rf}^{1/2}$ observed in similar hybrid devices for propagating SAWs, which would be expected for the linear deformation potential coupling [24, 51]. However, it is also less than $\Delta E_{max} \propto P_{rf}^1$, expected for Stark-effect modulation, which however, can be excluded in our device due to the palladium layer shielding the electric field of the SAW. Thus, a nonlinear coupling due to sum and difference frequency generation processes remains as a plausible origin for the observed and reproducible optomechanical coupling in both devices. Moreover, the fact that $m > 1/2$ is found for all optomechanical features, shows that both devices are not in the linear regime and nonlinear frequency mixing can occur for any SAW frequency inside the reflection band of the resonators Bragg mirrors.

5.4 FEM simulation

In order to see if there could still be a possibility of a mechanical explanation for the specific features of the optomechanical modulation of the QDs in the SAW resonator devices, finite element simulations are conducted using Comsol Multiphysics. Due to the large size of the resonator in units of λ_{SAW} , the calculation time and necessary resources are quite substantial. To reduce them, the model is limited to a 2D geometry

with a slightly smaller wavelength and larger frequency than the one in the experimental part of this chapter but still close enough to stay comparable. The cavity size is also kept small thus reducing the number of modes but with at least three to verify the frequency mixing. The creation of the model was accomplished as part of a scientific stay at the University of Valencia, Spain, in collaboration with PhD student André Bilobran.

5.4.1 Geometry of the resonators model

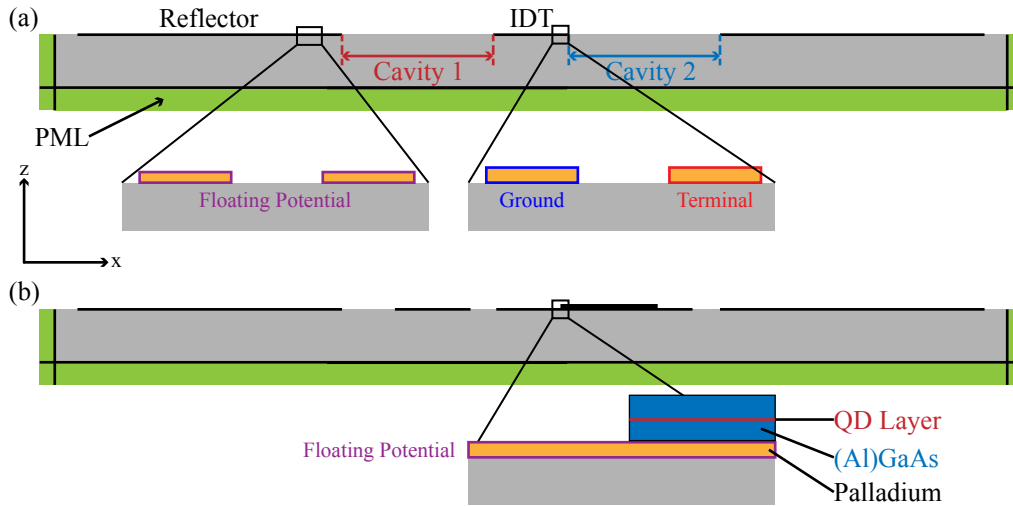


Figure 5.11: Geometry of the SAW resonator used for the FEM simulation in Comsol Multiphysics (a) for the unloaded and (b) hybridised device.

The two geometries used to model the resonators in Comsol Multiphysics are presented in Figure 5.11. In (a), the free LiNbO_3 model or bare resonator design is depicted. The resonator consists of two Bragg reflectors and an IDT forming two cavities: cavity 1 and cavity 2. In (b), the hybridised design is shown with the addition of the Pd adhesion layer and the $\text{Al}_{0.33}\text{Ga}_{0.67}\text{As}$ epilayer placed in cavity 2. The number of electrodes in the IDT is fixed to $N_{IDT} = 15$. The boundary conditions on the electrodes are either put to ground (blue) or to a terminal boundary condition (red). The terminal boundary condition enables the user to fix the input power and frequency applied to the IDT and to calculate classical electrical parameters such as, in our case, the reflective scattering parameter S_{11} . At the boundary of the reflectors' electrodes, a floating potential condition is applied (purple), which is separate for each reflector. If the floating potential group option is selected, each electrode is given its own potential and the reflector acts as an open-circuit assembly of electrodes. On the other hand, if the option is not selected, all the electrodes in the group are given the same potential and act as a short-circuited reflector. This way, resonators R1 and R2 can both be treated in a simulation. The number of electrodes is fixed at $N = 100$ which is sufficient to obtain strong reflection and keep the SAW inside the cavity. To artificially increase the cavity size while reducing the size of the model, the thickness of the

reflector electrodes is smaller than the ones for the IDT as illustrated in the zooms in Figure 5.11(a). Contrary to the reflector, the improved precision is needed at the IDT to compute the scattering parameter correctly.

The LiNbO_3 and $\text{Al}_{0.33}\text{Ga}_{0.67}\text{As}$ are taken as piezoelectric materials and the same material parameters as the ones for the simulation in Chapter 4 are used (see Appendix A). Just like in those simulations, the palladium layer edges are defined by a floating potential boundary condition (purple). An addition to the model in Chapter 4 is the perfectly matched layer (PML) at the end and bottom of the LiNbO_3 substrate (green areas). These layers are placed there to attenuate the incoming waves coming through the reflectors towards the sides of the substrate and the bulk waves possibly coming from the IDT towards the bottom of the substrate. The presence of these PMLs allows for the simulation of an infinite substrate which is closer to reality. This way, any type of reflection from the border which would interfere with the results and produce artificial deformation can be avoided.

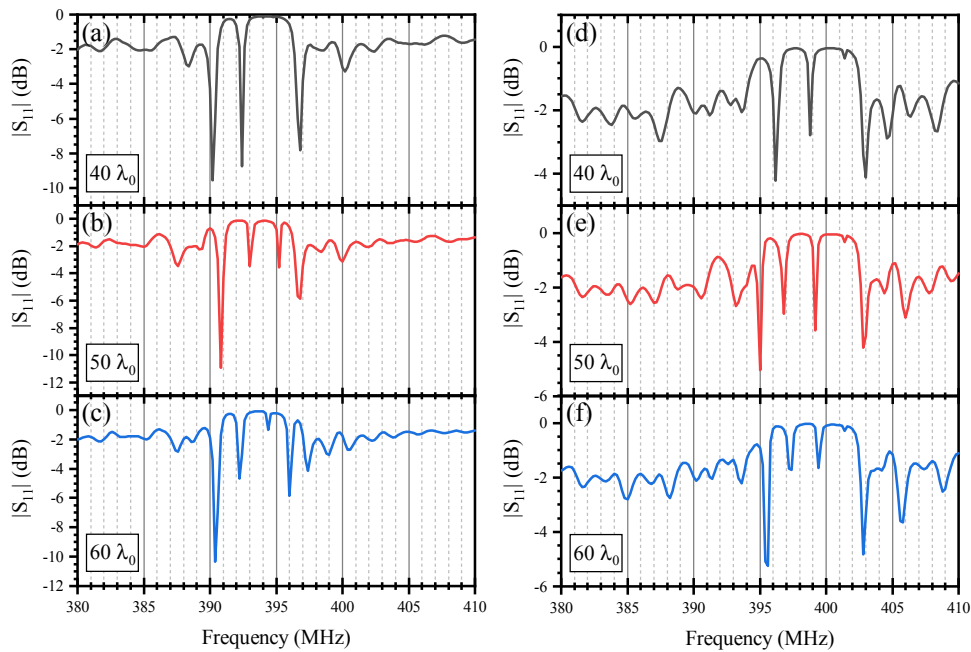


Figure 5.12: Reflective scattering parameter S_{11} of the resonator model, calculated at the terminal of the electrodes of the IDT with Comsol Multiphysics. The length of the cavity 1 (left cavity) is fixed at $10\lambda_0$ and the cavity 2 (right cavity) is varied between $40\lambda_0$ in (a) and (d), $50\lambda_0$ in (b) and (e), and $60\lambda_0$ in (c) and (f). The floating potential condition on the reflectors is close-circuited for (a-c) and open-circuited (d-f).

The study in this case is no longer an eigenfrequency characterisation but a frequency study. Here, the frequency of the input signal at the terminal is swept through a fixed range and the steady state solution is calculated for each frequency. To compute the hydrostatic pressure at the position of the QD and, thus, its resulting optomechanical response mediated by the deformation potential coupling, a boundary (red) is introduced at the centre of the $\text{Al}_{0.33}\text{Ga}_{0.67}\text{As}$ layer as seen in Figure 5.11(b).

5.4.2 Bare resonators

As a first simulation, the SAW resonator model with a bare LiNbO₃ substrate without the Pd and (Al)GaAs layers is modelled for the two different floating potential conditions and different cavity 2 (right cavity) lengths. The cavity 1 (left cavity) is fixed at $10\lambda_0$ and the length of cavity 2 is varied: $40\lambda_0$, $50\lambda_0$ and $60\lambda_0$. The calculated electrical spectra for each case are presented in Figure 5.12. As expected, the average FSR decreases with increasing cavity length and, moreover, the centre frequency is larger for the resonator with open-circuited reflectors compared to the short-circuited reflectors. The FSR goes from 2.2 MHz for a cavity 2 length of $40\lambda_0$ to 2 MHz for $50\lambda_0$ and 1.8 MHz for $60\lambda_0$. This confirms the observations made for the experimental resonators in Section 5.2.

5.4.3 Hybridised resonators

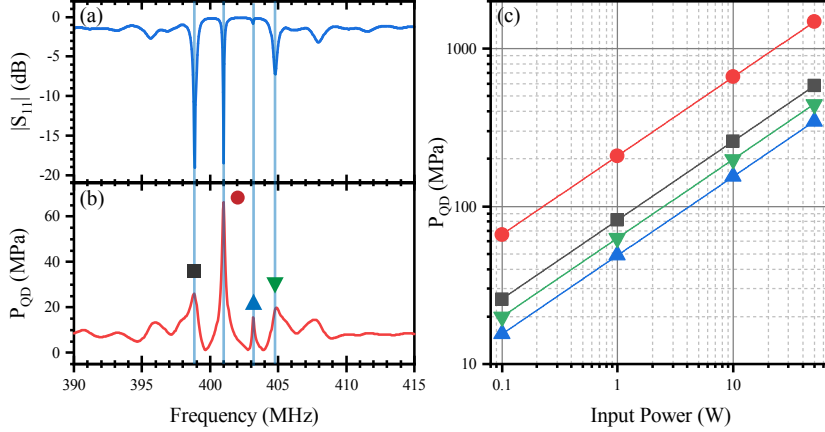


Figure 5.13: (a) Magnitude of the reflective scattering parameter $|S_{11}|$ calculated at the terminal of the IDT inside the resonator with short-circuited reflectors. (b) Hydrostatic pressure calculated at the level of the QDs P_{QD} at a randomly selected position in the membrane along the SAW propagation axis. (c) Maximal hydrostatic pressure at the frequencies of the resonator modes, indicated by the symbol in (b), plotted in a double logarithmic scale as a function of the input power applied to the IDT with the linear fit of the dependence.

For the simulation of the hybridised resonator, the length of cavity 2 is set to $50\lambda_0$. This length is a good compromise between getting a sufficiently large number of modes while keeping the computing resources and time for the simulation small. Frequency sweeps are conducted for four different input powers applied through the terminal boundary condition of the IDT: 0.1, 1, 5 and 50 W. The hydrostatic pressure at the position of the QD in the centre of the membrane is calculated for each power. The magnitude of the reflective scattering parameter $|S_{11}|$ is calculated at the terminal of the IDT inside the resonator. It is plotted in Figure 5.13(a) for a resonator with short-circuited reflectors. Additionally, the hydrostatic pressure at the level of the QDs

and for a randomly selected lateral position along the resonator axis is plotted in Figure 5.13(b). The four modes of the resonator present in the electrical spectrum are faithfully reproduced in the pressure spectrum.

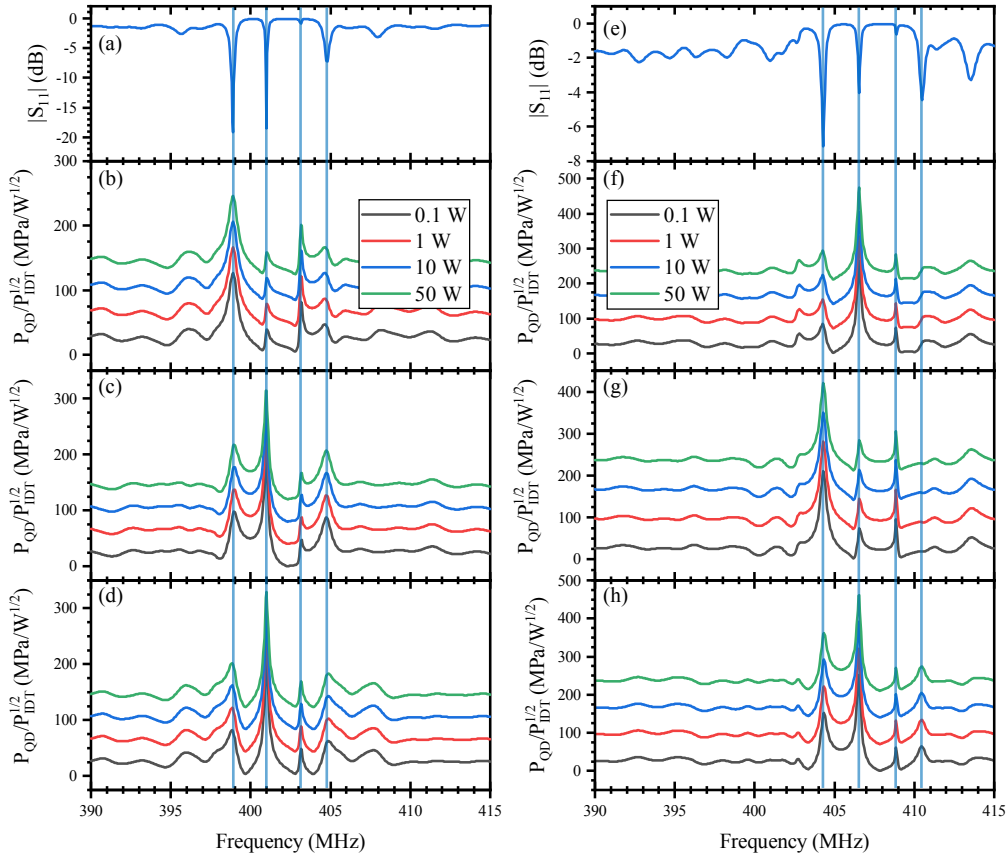


Figure 5.14: (a) and (e) Reflective scattering parameter S_{11} calculated at the terminal of the IDT inside the resonator for short-circuited reflector (a) or open-circuited reflectors (e). (b-c) Hydrostatic pressure divided by the square root of the input power $|P_{QD}|/P_{IDT}^{1/2}$ for a short-circuit geometry for four different input powers: 0.1, 1 10 and 50 W separated by a constant offset and for a QD at the following positions: the centre of the cavity (b), the centre of the (Al)GaAs membrane (c) and a randomly selected position in the membrane (d). (f-h) Hydrostatic pressure divided by the square root of the input power $|P_{QD}|/P_{IDT}^{1/2}$ for an open-circuit geometry for four different input powers: 0.1, 1 10 and 50 W separated by a constant offset and for a QD at the following positions: the centre of the cavity (f), the centre of the (Al)GaAs membrane (g) and a randomly selected position in the membrane (h).

The dependence of the pressure on the input power is analysed by extracting the maximum pressure at the frequencies of the mode, indicated by the symbol in Figure 5.13(b). The data is plotted in a double logarithmic scale as a function of the input power applied to the IDT in Figure 5.13(c) to identify the power law dependence by using the linear fits of the data present in the plots. The slope is exactly equal to 0.5 for all four fits. We conclude that the amplitude of the pressure increases with the square

root of the input power which is proportional to the amplitude of the surface acoustic wave as expected. Therefore, to ease the comparison between the cases, the hydrostatic pressure is divided by the square root of the input power $|P_{QD}|/P_{IDT}^{1/2}$. In Figure 5.14, the reflective scattering parameter $|S_{11}|$ spectrum for both resonator geometries is presented and compared to $|P_{QD}|/P_{IDT}^{1/2}$ calculated at three different lateral positions inside the (Al)GaAs membrane along the resonator axis: in the centre of the cavity (b,f), in the centre of the membrane (c,g) and at a randomly selected position (d,h). The spectra of $|P_{QD}|/P_{IDT}^{1/2}$ are plotted with a constant offset for each input power to facilitate the comparison.

The data in Figure 5.14 confirms that the coupling of the QDs to the resonator modes is dependent on their location. Additionally, it clearly shows that all the mechanical response curves are identical. This means that, in this model, the input of more power does not change the mechanical spectrum of the hydrostatic pressure or its dependence to the square root of the input power. All in all, the simulation demonstrates a clear linear behaviour for the hydrostatic pressure inside the hybridised resonator. This is in contrast to the experimental observations where we see the emergence of frequency mixing peaks and a power dependence of the QDs' optomechanical response greater than 0.5. From this, we can conclude that the optomechanical coupling of the QDs and the SAW resonator does not follow the linear behaviour presented by these simulations. Therefore, frequency mixing and non-linear processes are still a plausible explanation for the observed experimental behaviour.

Conclusion

In this chapter, we demonstrate the successful coupling of QD's excitons to the phononic modes of a SAW cavity. Even after the transfer of the (Al)GaAs layer inside the cavity, the quality factor of the resonator remains high, $Q \sim 2500 - 3000$, ensuring the coherent behaviour of the SAW field. The coupling between the QDs and the modes is proven to be index dependent as the localisation of the dots in the standing wave pattern of the SAW influences their coupling to the resonator modes. The frequency-dependent response of the QD's emission shows a complex behaviour with the presence of frequency mixed peaks in the optomechanical response. Additionally, the power dependent amplitude of the QD's response does not follow a classical $P_{rf}^{1/2}$ or P_{rf}^1 power dependence and display an exponent $1/2 < m < 1$. The finite element simulations performed in 2D show that these features do not have a mechanical origin. With all these observations, we come to the conclusion that a non-linear frequency conversion is a plausible cause for this complex behaviour.

Perspective: Quantum Dots and Photonic Structures on LiNbO_3

The previous chapters focused on the transfer of simple QD membranes on increasingly complex SAW-chip configurations. In this chapter, the transferred epilayer is patterned into more complex photonic structures: ring resonators and their access waveguides. The interaction between the SAW, the QDs and the resonators is then measured and analysed. This project was developed with Bruno Villa, PhD student at the Toshiba Research Lab in Cambridge as part of the SAWtrain european network. The design of the photonic structures was realised by Bruno Villa and the result of his simulations is briefly presented here. The fabrication was done in Augsburg with only the last step, the reactive ion etching, done at the Toshiba Research Lab facilities. First optical characterisations of the system were done at the Toshiba Research Lab facilities, especially the characterisation of the waveguide and the grating couplers. These results are presented in Bruno Villa's PhD thesis [75]. Further experiments were done in Augsburg and focussed on the interaction between the SAW, the QDs and the ring resonator and are presented in this chapter. The measurements show that the QDs can be tuned in and out of resonance with the ring resonator mode. Additionally, the emergence of phononic resonances is presented and the non-linear behaviour of these modes is analysed.

6.1 Ring resonator: whispering gallery mode cavities

The ring resonators are whispering gallery mode cavities where the optical modes are confined within the cavity by total internal reflections from the curved surface of the resonator. The resonator is made of a material with a larger refractive index than its surrounding and the light is then confined to the edge of the resonator [77]. Generally, a ring resonator is made of a looped optical waveguide supporting transverse modes. These transverse modes can be separated in transverse electric (TE) modes and transverse magnetic (TM) modes. In TE modes, there is no electric field in the direction of

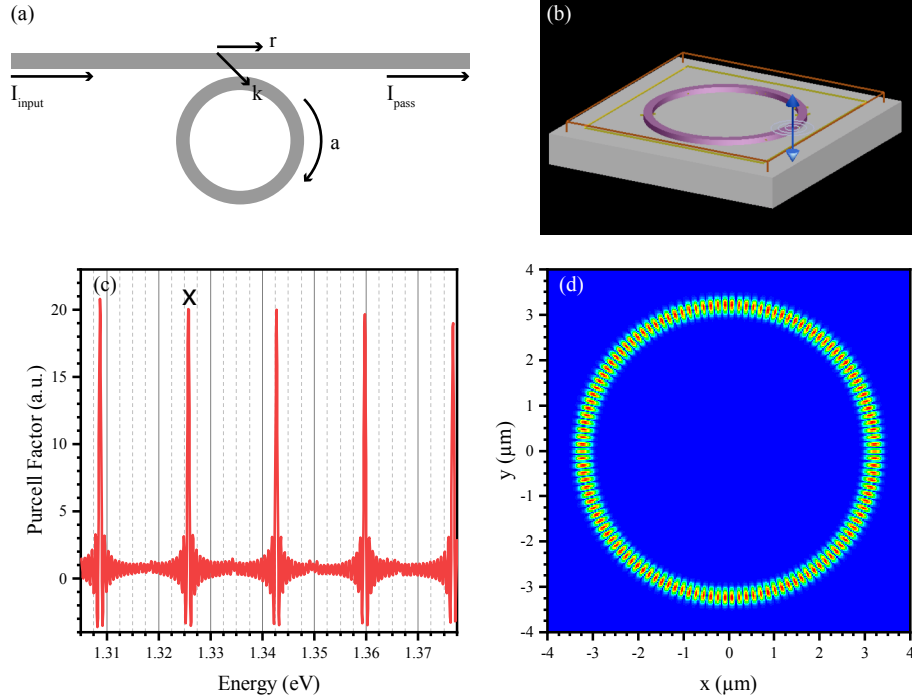


Figure 6.1: (a) Schematic depiction of a ring resonator and its access waveguide, adapted from [76]. (b) Geometry of the FDTD simulation of a GaAs ring resonator on a LiNbO_3 substrate with a diameter of $6\ \mu\text{m}$. (c) Purcell enhancement factor of the dipole computed inside a ring resonator of $6\ \mu\text{m}$ diameter by FDTD simulation. (d) False colour plot of the mode profile, magnitude of the electric field, inside the ring resonator for the mode indicated by the cross in (c).

propagation of the electromagnetic wave. The electric field variation is then contained in the plane perpendicular, i.e. transverse, to the wave propagation. In the case of TM modes, it is the magnetic field which has no component in the propagation direction of the wave and is confined in the transversal plane. To achieve resonance, an integer number of optical wavelengths in the circumference of the ring is necessary. This leads to the following expression for the modes of the ring [76, 77]:

$$m\lambda_{res} = 2\pi R n_{eff} \quad (6.1)$$

where λ_{res} is the wavelength of the resonant mode, m is the mode order and is an integer, R is the radius of the ring resonator and n_{eff} is the effective refractive index of the mode. The profile of such an optical mode is plotted in Figure 6.1(d) and the order of the mode can be easily concluded from the number of nodes and antinodes presented by the electric field in the mode profile. The modes' quality factor of such ring resonators have been experimentally demonstrated to be large in the range of $1 \times 10^5 - 1 \times 10^6$ [78, 79, 80]. However, these resonators are difficult to excite directly by direct illumination of a part of the ring with a laser. For this purpose, an access waveguide is necessary, as illustrated in Figure 6.1(a). In this scheme, the ring

resonator couples to the waveguide with the self-coupling coefficient r and the cross-coupling coefficient k since the waveguide not only provides access to the resonator but also an additional path for the light to escape the resonator. Thus, r^2 and k^2 are the power splitting ratios of the coupler and they are assumed to satisfy $r^2 + k^2 = 1$ when neglecting losses in the coupling section. a is the single-pass amplitude transmission which includes both the propagation loss in the ring and the loss in the couplers. The coupling between the waveguide and the resonator is characterised by a and r such that, when $r > a$, the system is undercoupled and the light field does not fully build up inside the resonator. For $r = a$ or when the coupled power is equal to the power loss in the ring $1 - a^2 = k^2$, the system is critically coupled and the transmission through the waveguide drops to zero since all the input light couples into the resonator and is dissipated there. Usually, this is the condition in which the system should be operated. For $r < a$, the system is overcoupled and the waveguide damps the light field build inside the resonator [76]. The Q-factor of the modes is also influenced by the coupling to the waveguide such that [76]:

$$Q = \frac{2\pi^2 R n_g \sqrt{ra}}{\lambda_{res}(1 - ra)} \quad (6.2)$$

where n_g is the group index, taking into account the dispersion of the light inside the waveguide and resonator with $n_g = n_{eff} - \lambda_0 \frac{dn_{eff}}{d\lambda}$. This quality factor is called the loaded quality factor which takes into account the coupling of the resonator to the waveguide, in contrast to the unloaded quality factor which characterises the bare resonator.

The ring resonators considered in this chapter can also be modelled using a finite-difference time domain (FDTD) simulation with a commercially available software, Lumerical. The geometry used for this simulation is presented in Figure 6.1(b). The substrate in grey is LiNbO₃ with a refractive index of 2.2 and the ring is made of GaAs (purple) with a refractive index of 3.4 and a diameter of 6 μm and cross-section of $350 \times 350 \text{ nm}^2$. A dipole serves as a source with an energy E in the range of the QDs present in the GaAs membrane, $1.3 \leq E \leq 1.38 \text{ eV}$. The time evolution of the dipole pulsed emission is computed by the software. From there, the spectrum of the resonator is computed by Fourier transform of the time evolution of the electric field $\mathbf{F}(t)$ along with the quality factor of the modes. The average quality factor is 4.4×10^5 , which confirms the high optical qualities of this kind of resonator. The Purcell enhancement factor defines the degree of enhancement of the emission of an emitter inside a cavity and is defined as the ratio between the decay rates outside and inside the cavity [81]. The Purcell factor of the dipole inside the cavity is plotted as a function of its emission energy in Figure 6.1(c). From this spectrum, the position of the modes and their high optical quality can be seen. The Purcell factor reaches high values of ~ 20 . This simulation confirms that the ring resonator qualities can be achieved on a GaAs/LiNbO₃ platform. The magnitude of the electrical field inside the ring resonator is plotted in Figure 6.1(d) for the mode indicated by a cross in 6.1(c). In this case, the number of antinodes for the magnitude of the electric field is 126, which indicates a mode order of $m = 63$.

6.2 Design and fabrication

A schematic depiction of the fabricated devices is presented in Figure 6.2(a). There, we can see that the photonic structures are composed of a ring resonator and an access waveguide situated below the ring which optically pump the resonator. An excitation laser can be coupled from the top by the grating couplers at both ends of the waveguide. The photonic structures are fabricated from a GaAs membrane containing InAs QDs which was transferred on the LiNbO₃ substrate by epitaxial lift-off. Surface acoustic waves can be excited by IDTs that were patterned on the LiNbO₃ substrate before the transfer.

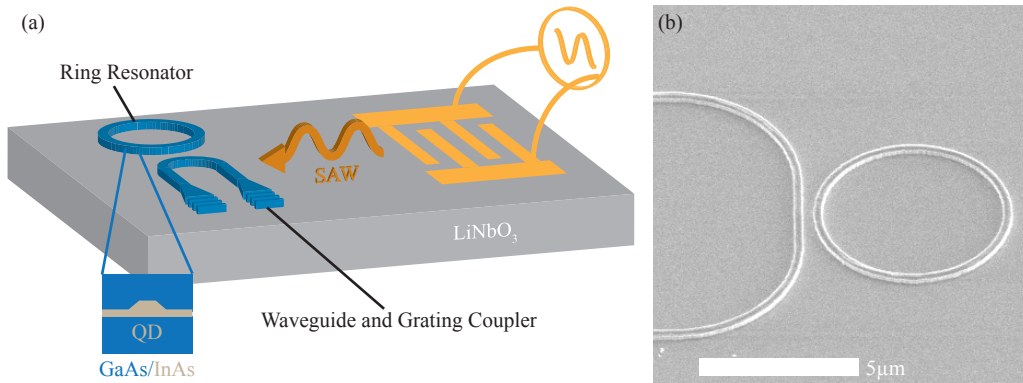


Figure 6.2: (a) Schematic depiction of the device, where the ring resonator and the waveguide coupling to the resonator are made of a GaAs QD membrane transferred on top of a LiNbO₃ SAW-chip. (b) Scanning electron microscope image of a ring resonator patterned on a LiNbO₃ substrate with a diameter of 6 μm.

The thickness of the GaAs membrane has to be chosen to ensure that the waveguide and the ring resonator only carry the fundamental TE and TM modes and to maximize the Q-factor of these modes. Additionally, the gap between the ring and the waveguide, the geometry parameter of the waveguide taper and the apodization parameters of the grating couplers have to be computed. All of the simulations to determine these design parameters on LiNbO₃ were realised by Bruno Villa, PhD student at Toshiba Cambridge, using Comsol Multiphysics at an optical wavelength of 940 nm which is in the range of the QD's emission wavelength. The details of the procedure can be found in his thesis [75].

The target dimension extracted from the simulations for the waveguide is a cross-section of $350 \times 350 \text{ nm}^2$ which fixes the thickness of the transferred GaAs membrane. For the ring dimensions, the thickness will be fixed but the width can be anything from 350 nm up to a full disk. In the end, the electron beam mask used for these experiments contains rings with a width of 350 nm with different diameters, 6, 12 and 24 μm, and disks with two different diameters, 12 and 48 μm. The optimum gap value between the access waveguide and the ring resonator varies depending on the ring width and radius but is consistently between 210 and 300 nm. To take into account possible fabrication imperfections, the gap in the mask is varied between these two values with multiple

structures which cover this range. The waveguide taper present before the grating coupler must be designed to reduce the size mismatch between the Gaussian mode of the exciting laser and the waveguide mode and to avoid conversion to higher order modes which are supported in wider waveguides. The final dimensions are fixed to a $10\ \mu\text{m}$ long expansion region starting from the $350\ \text{nm}$ -wide waveguide and ending in a $3\ \mu\text{m}$ wide waveguide before the grating coupler. The geometry of the grating coupler is chosen to enable the coupling of the free-space Gaussian beam laser perpendicularly in and out of the waveguide. Therefore, the coupler is apodized with a grating periodicity $\Lambda(z)$ varying linearly along the length of the structure as described by the following equation:

$$\Lambda(z) = \frac{\lambda_0 - \lambda_{offset}}{(F_0 - R_z) \cdot n_{GaAs} + (1 - F_0 + R_z) \cdot n_{air}} \quad (6.3)$$

where the light propagates along the z axis, the grating starts at $z = 0$, F_0 is the initial fill factor of the grating, R_z is the apodization rate and n_{GaAs} and n_{air} are the refractive index of GaAs and air, respectively. The parameters are fixed to $R_z = 0.05\ \mu\text{m}^{-1}$, $\lambda_{offset} = 140\ \text{nm}$ and $F_0 = 0.8$. Finally, the U-bend geometry of the waveguide is chosen so that the separation between the input and output grating couplers is fixed to $10\ \mu\text{m}$ which is the maximal separation for input and collection spots in the optical system in the laboratory at the Toshiba Research Lab in Cambridge.

The QDs used in this chapter were grown by molecular beam epitaxy by our collaborators in TU München and they are InAs QDs positioned in the centre of a $350\ \text{nm}$ -thick GaAs membrane on top of a $100\ \text{nm}$ AlAs sacrificial layer. The growth process and complete layer structure are described in chapter 3. The semiconductor membrane is transferred by epitaxial lift-off on top of a LiNbO_3 substrate by selectively etching the sacrificial layer in a diluted HF solution. In the two previous chapters, the epilayer is transferred on a Pd adhesion layer. Here, we omit the Pd layer to avoid potential optical losses and a reduction of the confinement of the light in the semiconductor membrane. Therefore, the GaAs membrane is directly transferred on the LiNbO_3 substrate and the bonding is limited to van der Waals interactions. The bonding is still sufficiently strong for successful post-processing of the membrane using electron beam lithography and reactive ion etching to produce the photonic structures. The details of the fabrication process are described in chapter 3 and the successful result of the post-processing is shown in a scanning electron microscope image in Figure 6.2(b), where we can see that the desired small features of the ring resonator and waveguide structures were achieved.

To excite the surface acoustic wave on the LiNbO_3 substrate, interdigitated transducers (IDT) are patterned by E-beam lithography before the transfer of the semiconductor membrane. The metals deposited are $5\ \text{nm}$ Cr and $50\ \text{nm}$ Au in order to resist the reactive ion etching used to pattern the QD epilayer. The geometry of the IDT determines the spectrum of SAW frequencies which can be excited. For this sample, we want to couple the QDs to the ring resonator cavities with different SAW frequencies. For this purpose, the geometry of the IDT is based on the one developed at the Universität Augsburg by Matthias Weiß [13]. By combining a chirp and a Split 5-2 geometry, not only a first band of frequencies can be excited, given by the chirp, but also the

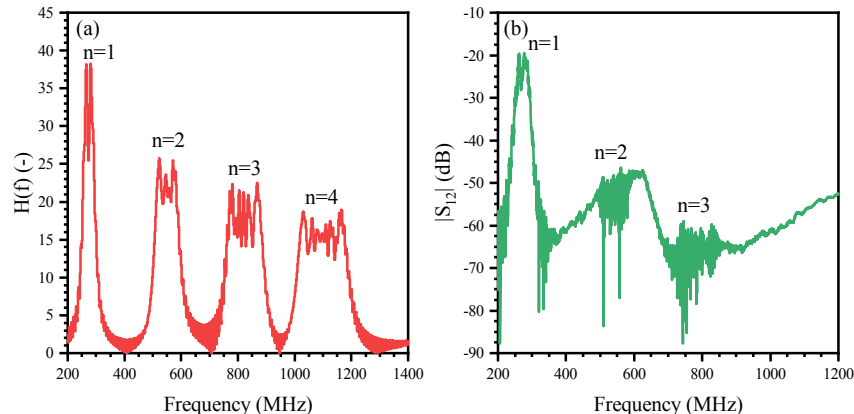


Figure 6.3: (a) Simulated frequency response of the chirped split 5-2 IDT geometry. (b) Amplitude of the transmission scattering parameter $|S_{12}|$ of the chirped Split-52 delay line measured with a vector network analyzer.

2nd, 3rd and 4th harmonics of this band. In Figure 6.3 (a), the frequency response of the IDT was computed using an impulse model described in chapter 1. All four bands can be seen: the first with $250 \leq f_{SAW} \leq 300$ MHz and then the 2nd, 3rd and 4th with $500 \leq f_{SAW} \leq 600$ MHz, $750 \leq f_{SAW} \leq 900$ MHz and $1 \leq f_{SAW} \leq 1.2$ GHz, respectively. In Figure 6.3(b), the vector network analyser measurement of the transmission scattering parameter amplitude $|S_{12}|$ for the fabricated IDTs is plotted and the three first bands can clearly be resolved. The 4th band is not seen which can be attributed to fabrication imperfection and mass loading. However, a large range of frequencies between 250 and 900 MHz can still be excited.

The characterisation of the grating coupler and waveguide transmission was performed at the Toshiba Research Lab with Bruno Villa and is available in his PhD thesis [75]. In this work, the sample was studied in a confocal optical set up and, therefore, the QDs emission was measured by directly exciting and collecting the emission from the QDs positioned in the ring resonator.

6.3 Photonic mode: SAW tuning of QD in/out of resonance

One of the interesting possibilities with QDs in photonic cavities is to be able to tune the QD's emission line in and out of resonance with the cavity. This can be achieved dynamically using surface acoustic wave as it was previously demonstrated by Weiß and co-workers in Augsburg for a cavity in a 2D photonic crystal [82] and, later, by Bruno Villa and co-workers in Cambridge for a QD embedded in a micro-pillar cavity [83]. To observe this kind of modulation, we selected a QD close to a resonator mode and record its emission spectra in a time-resolved optical measurement, while dynamically tuning the system with a SAW.

The optical measurement is performed with the sample mounted in a closed-looped

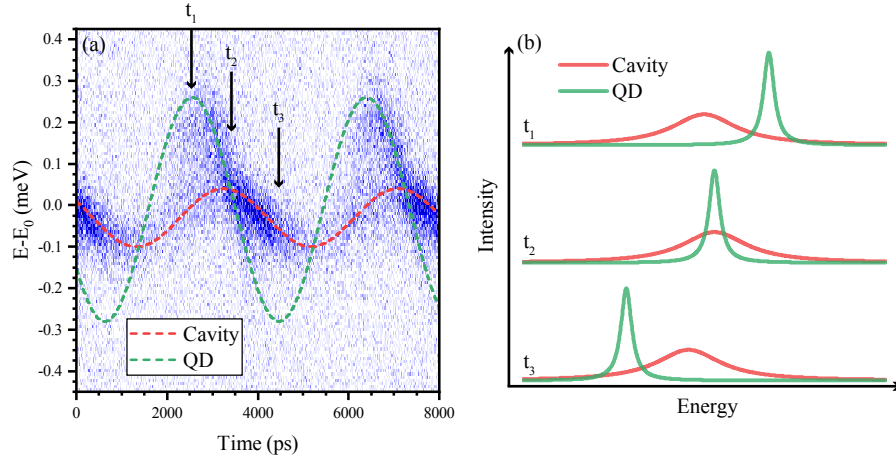


Figure 6.4: (a) Time-resolved and spectrally resolved measurement showing the temporal modulation of a QD in and out of the ring resonator cavity mode by a surface acoustic wave for an applied rf signal at the IDT with $f_{rf} = 260$ MHz and $P_{rf} = 10$ dBm. (b) Schematic of the tuning of the cavity (red) and QD (green) emission energy by the SAW at three different time stamps indicated in (a).

cryostat in a conventional confocal micro-photoluminescence (μ -PL) setup at 5 K. The optical excitation is done by a continuous wave diode laser at a wavelength of 840 nm and focused on the sample by a microscope objective mounted in the cryostat. The emission of individual QDs is then collected by the same objective, filtered to a specific wavelength by a 0.75 m grating monochromator. The signal exiting the monochromator is detected by a single-photon avalanche diode, recording its time evolution. The wavelength is controlled and swept by the position of the grating in the monochromator and for each wavelength the time evolution of the QD's emission is recorded. In this way, a spectrally-resolved and time-resolved measurement is obtained. More details on the time-resolved spectroscopy are available in Chapter 2. The excitation and detection of the QDs emission in the ring resonators is performed under normal incidence by a microscope objective and not via the waveguide and grating couplers. The extracted emission intensity is therefore not so large and reflects the emission losses from the ring resonator. The SAW is also excited by applying a continuous signal of frequency $f_{rf} = 260$ MHz and power $P_{rf} = 10$ dBm.

The spectrally- and time-resolved measurement of the QD's modulation in and out of the cavity mode is presented in Figure 6.4(a). We can see two signals oscillating with the SAW frequency f_{rf} . Both signals are overlaid with sinusoidal dotted lines as a guide for the eyes. The equation for the modulation follows a sinusoidal function with the same period as the SAW. The oscillation of larger amplitude (green dotted line) is attributed to the QD and the smaller amplitude to the cavity mode being modulated by the SAW (red dotted line). Both systems are tuned by the SAW but present different phases. When the QD's emission is tuned into resonance with the resonator mode, the emission intensity is enhanced by the Purcell effect. The tuning of the QD's emission in and out of resonance with the resonator mode is schematically depicted in Figure

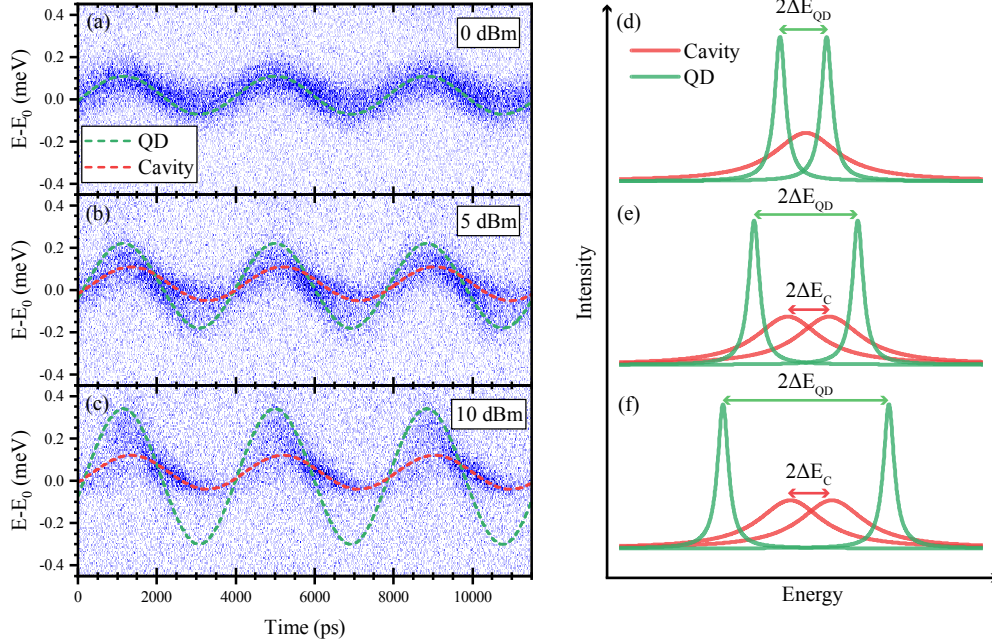


Figure 6.5: (a-c) False colour plot of the time-resolved and spectrally resolved measurement showing the temporal modulation of a QD in and out of the ring resonator cavity mode by a surface acoustic wave with $f_{rf} = 260$ MHz and three different applied rf powers P_{rf} : 0 (a), 5 (b) and 10 dBm (c). (d-f) Schematic of the cavity (red) and QD (green) tuning amplitude by the surface acoustic wave for the three different applied rf power P_{rf} : 0 (d), 5 (e) and 10 dBm (f).

6.4(b) for the three time stamps indicated in Figure 6.4(a). At time stamp t_1 , the QD is detuned from the resonator mode and the emission is suppressed. When the QD is tuned in resonance with the cavity at time t_2 , the radiative decay rate of the QD is increased and the intensity of the emission increases strongly as seen in the false colour plot in Figure 6.4(a). As both the QD's emission and the resonator mode are further modulated by the SAW, the QD is detuned from the cavity and the emission intensity decreases, which can be seen at time t_3 . One interesting observation is the asymmetry of the emission enhancement. This enhancement at resonance is only observed for the descending slope of the SAW modulation. This asymmetry was also observed by Weiß and coworkers for a QD embedded in a 2D photonic crystal cavity [82].

To ensure that the identification of both signals is accurate, the evolution of the modulation as a function of the applied P_{rf} is studied. Time-resolved data for three different powers are plotted in false colour plots in Figure 6.5. We can see the same modulation as in Figure 6.4 for $P_{rf} = 10$ dBm in Figure 6.5(c). For a lower power, $P_{rf} = 5$ dBm, we can see that the QD modulation is reduced while the cavity mode modulation has stayed quite constant. The asymmetry of the Purcell enhancement is still present but the Purcell suppression of the QD's emission is less pronounced compared to the measurement at $P_{rf} = 10$ dBm. The QD's emission can be resolved at all times, which is not the case in Figure 6.5(c). At the lowest power, $P_{rf} = 0$ dBm in Figure 6.5(a), only one signal is visible which means that the QD's emission is in

constant resonance with the cavity mode and both modulations are weak. From this, we can conclude that the modulation of the cavity is quite low and does not depend as much on the SAW amplitude as the QD's emission modulated by the deformation potential coupling. These differences in amplitude are schematically summarized in Figure 6.5(e-f), where the extrema of the tuning of the cavity mode and the QD's emission are plotted. In Figure 6.5(d), at low power, the QD is tuned inside the cavity mode width. As the power increases to 5 and 10 dBm, in Figure 6.5(e) and (f), the QD modulation gets much larger than the one of the cavity.

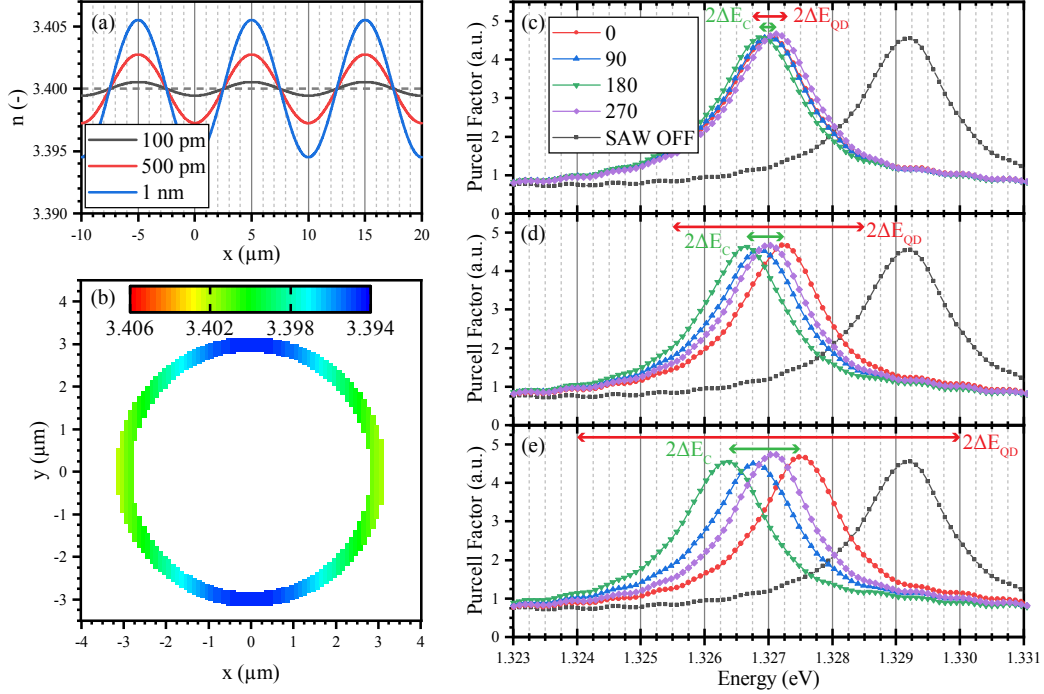


Figure 6.6: (a) Value of the refractive index n as a function of the position along the SAW propagation path x . The refractive index is modulated by the SAW through the elasto-optic effect for three different vertical displacement of the SAW at the surface of the substrate: 100 pm, 500 pm and 1 nm. (b) False colour plot of the refractive index value inside a ring resonator of 6 μm diameter for a vertical displacement of the SAW of 1 nm and a phase of 0° . (c-e) Purcell enhancement factor of the dipole computed inside a ring resonator of 6 μm diameter by FDTD simulation. This shows the modulation of one of the modes by a surface acoustic wave with a vertical displacement of 100 pm (a), 500 pm (b) and 1 nm (c) at the surface of the substrate. The equivalent modulation of the QD, ΔE_{QD} , is indicated by the red double arrows.

To confirm our observations, we have to look into more details at how the cavity is tuned by the surface acoustic wave. In this context, a finite-difference time domain (FDTD) simulation of the ring resonator modulated by the SAW is performed, using the commercially available software Lumerical. The largest contribution of the SAW modulation of the ring resonator modes is due to the elasto-optic effect in GaAs, in which the refractive index n of GaAs is modified by the strain produced by the acoustic

field, such that:

$$\Delta \left(\frac{1}{n^2} \right)_{ij} = p_{ijkl} S_{kl} \quad (6.4)$$

where p_{ijkl} is the fourth rank elasto-optic tensor and S_{kl} is the strain tensor [84, 85, 86]. The elasto-optic tensor parameters taken for this simulation are presented in Appendix A. We only take into account the elasto-optic effect as, per our calculation, the electro-optical effect in GaAs influence on n is weak. To calculate the change in refractive index in the ring resonator, the maximal strain associated with a specific surface vertical displacement of the SAW is calculated using the same FEM simulation presented in chapter 4. The strain is then multiplied by the elasto-optic tensor to compute the maximum possible change in refractive index in GaAs due to the SAW. The refractive index is then modelled as a sinusoidal modulation on a neutral refractive index of 3.4 along the path of a SAW with a wavelength of 10 μm . The result of this calculation of the refractive index n is plotted in Figure 6.6(a) for three different surface vertical displacement: 100 pm, 500 pm and 1 nm. The ring is modelled on top of a LiNbO_3 substrate by many rectangular slices each with a specific refractive index taken from the computation of the sinusoidal modulation of n by the SAW. The phase of the SAW is then manipulated by changing the refractive index value taken by the rectangular pieces from the model. An example of such a structure is presented in Figure 6.6(b) for a phase of 0° and a surface vertical displacement of 1 nm. The colour code shows the value of the refractive index n inside the ring resonator structure while the edge of the ring shows the rectangular pieces used to construct the model. An optical dipole is placed inside the ring to optically excite the resonator modes with a wavelength range encompassing the QDs emission wavelengths. The time evolution of the dipole emission is computed by the software. From this time evolution, the Purcell enhancement factor of the dipole inside the ring is computed and shows at which energy the ring resonator modes are present and their quality factor.

The result of this simulation is presented in Figure 6.6(c-e) for three different vertical surface displacements of the SAW: 100 pm (c), 500 pm (d) and 1 nm (e). For each displacement, the simulation is run for a complete phase cycle of $[0 : 90 : 270]^\circ$, equivalent to the measured time modulation of the cavity modes by the SAW. Additionally, the unperturbed cavity is also plotted (black), where each rectangular unit has the unmodulated refractive index of $n = 3.4$. For each simulation, the unperturbed ring resonator presents a static shift of the mode to higher energies compared to the SAW modulated simulations. For a displacement of 100 pm, the cavity modulation, ΔE_C (green double arrow), is quite small and falls under the spectral resolution of the simulation, $\Delta E_C \leq 0.1 \text{ meV}$. For the same vertical displacement, the dots are expected to exhibit a modulation of approximately $\Delta E_{QD} \approx 0.3 \text{ meV}$ (red double arrow), based on the FEM simulation presented in chapter 4 for a membrane thickness of 300 μm . As the displacement is increased to 500 pm, the modulation increases to $\Delta E_C \approx 0.25 \text{ meV}$ and to $\Delta E_C \approx 0.55 \text{ meV}$ for a vertical displacement of 1 nm. In comparison, the predicted QD's modulation is in the range of $\Delta E_{QD} \approx 1.5 \text{ meV}$ for a displacement of 500 pm and $\Delta E_{QD} \approx 3 \text{ meV}$ for a displacement of 1 nm. These simulation results confirms that the

identification of both signals in Figure 6.4 and 6.5 is correct with a lower modulation of the ring resonator mode than for the QD.

6.4 Observation of phononic modes

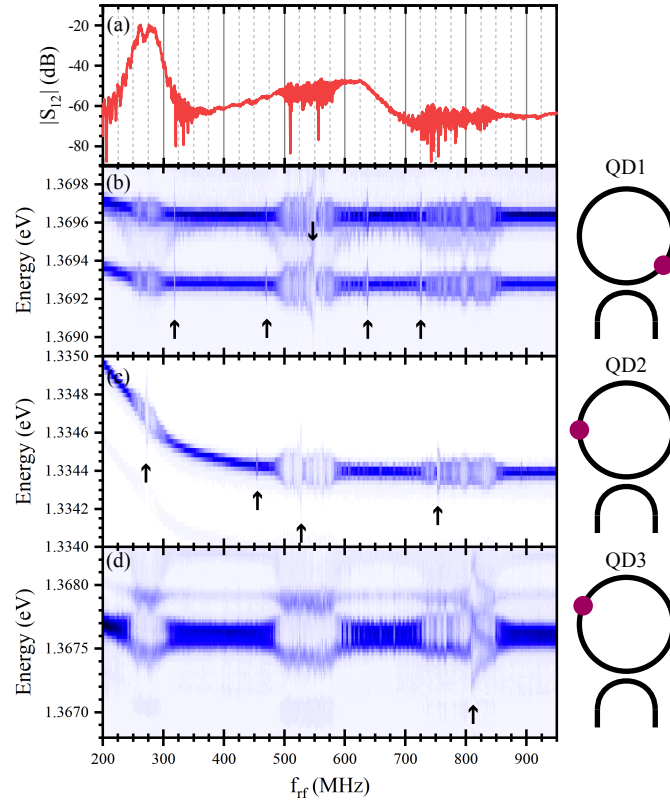


Figure 6.7: (a) Amplitude of the transmission scattering parameter $|S_{12}|$ of the chirped Split-52 delay line measured with a vector network analyzer. (b-d) False colour plot of the time-integrated spectrum of three QDs emission lines as a function of the applied rf frequency f_{rf} at a fixed $P_{rf} = 10$ dBm at three different positions in a ring resonator of $24 \mu\text{m}$ diameter. The positions of the dots are indicated in the schematics beside the colour plots. The possible phononic modes of the ring resonator are indicated by the arrows in the plots.

In this part of the chapter, the QDs are used not as two-level systems interacting with the photonic cavity but as a nanoscopic mechanical sensors. By observing their optomechanical response, we can determine how the SAW couples to the rings. The optomechanical response of the QDs in the ring resonator is characterised by measuring the optical response of the QD to the SAW emitted by the chirped IDT as a function of the applied frequency f_{rf} . The measurement is done in the same optical setup at 5 K presented in the previous section. The emission was however detected by a liquid N_2 cooled silicon charge-coupled device (CCD) and not a single-photon avalanche detector.

Due to the 840 nm diode laser being used in continuous wave mode, the measured spectra are phase averaged. By performing a sweep of f_{rf} in the range of 200 to 950 MHz, we expect to observe an optomechanical response of the dot only for the three bands of the chirped IDT, i.e. the QD's emission line will only show a broadening for the frequencies ranges emitted by the IDT: $n_1 = [250 : 300]$ MHz, $n_2 = [500 : 600]$ MHz and $n_3 = [750 : 900]$ MHz as shown in the VNA measurement of the IDTs transmission in Figure 6.7(a).

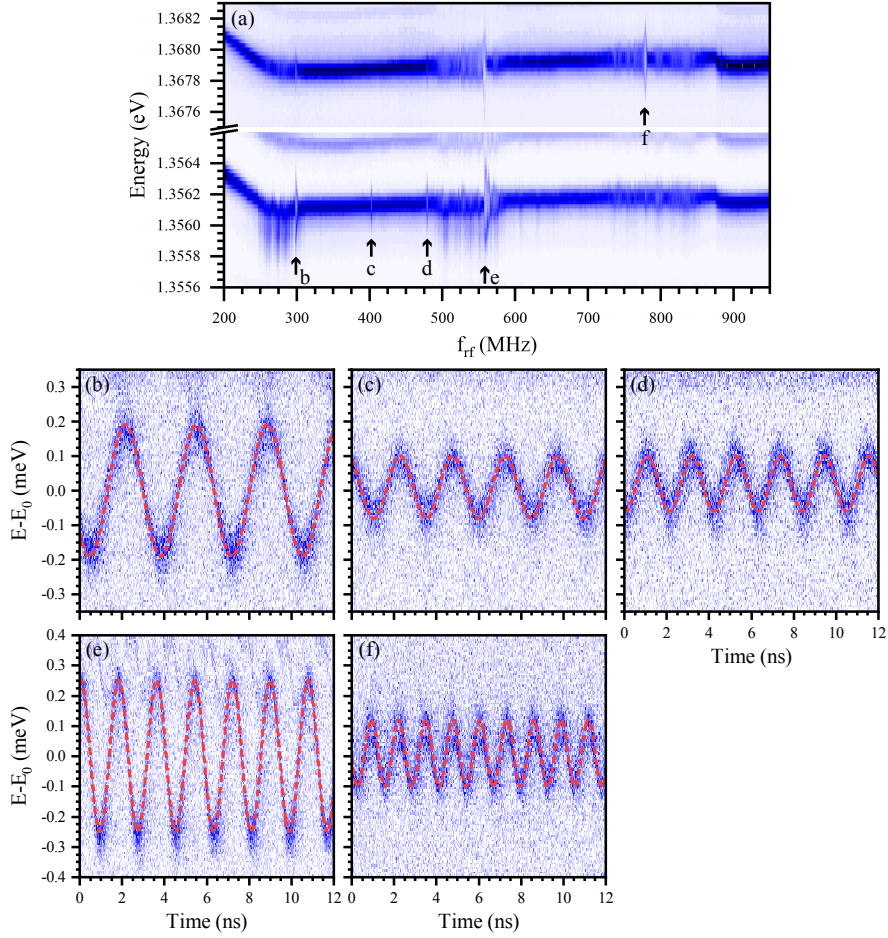


Figure 6.8: (a) False colour plot of the time-integrated spectrum of two QDs emission lines as a function of the applied rf frequency f_{rf} in a ring resonator of $24 \mu\text{m}$ diameter for $P_{rf} = 10 \text{ dBm}$. The phononic modes of the ring resonator are indicated by the arrows in the plots and the letter indicate the corresponding time-resolved plots. (c-f) False colour plots of the time-resolved and spectrally resolved measurement showing the temporal modulation of the QD emission line at the frequency of the phononic modes: 298.6 MHz (b), 402.6 MHz (c), 479 MHz (d), 558.4 MHz (e) and 779 MHz (f).

The result of such an optomechanical measurement with $P_{rf} = 10 \text{ dBm}$ for three QDs at three different positions on a ring resonator with a $24 \mu\text{m}$ diameter is plotted in a false colour plot in Figure 6.7(b-d). The position of the measured QDs is schematically depicted next to each data plot. As expected, the frequency bands are visible, but we

can also observe sharp broadening peaks of large amplitude inside and also outside of the frequency bands of the IDT plotted in Figure 6.7(a), which is highly unexpected. For QD1, positioned at -60° from the junction of the waveguide with the ring resonator, these peaks are present at the following frequencies: 318.4 MHz, 470 MHz, 547.8 MHz, 637.4 MHz and 725.6 MHz. These modes are indicated by arrows in the colour plot. For QD2, at 90° from the junction, the peaks are observed at 274 MHz, 454.2 MHz, 528 MHz and 753 MHz. One last peak is observed at 808.4 MHz for QD3, positioned at 120° from the junction. These sharp augmentations of the QD's modulation resemble the optomechanical response of the QDs to the mechanical modes of the SAW cavity presented in chapter 5. Therefore, we argue that these peaks arise from the presence of resonant modes of the SAW inside the ring resonators. This type of resonances were simulated and demonstrated in experiment for a gallium nitride (GaN)-on-sapphire ring resonator and SAW waveguide system by Fu and coworkers but on a larger scale than our system [87]. Their system is similar to the one presented here with a material with a slow phase velocity of the SAW on top of a material with a high phase velocity. In the work of Fu and coworkers, SAWs were guided and coupled to ring resonators by waveguides at a frequency of 200 MHz and wavelength of $25\ \mu\text{m}$. These modes are separated into Rayleigh-like modes, dominated by out-of-plane displacement, and Love-like modes, dominated by in-plane displacement.

To confirm that these phononic modes are indeed due to the presence of an acoustic wave confined in the ring resonator, time-resolved measurements are performed at the frequencies f_{rf} of the modes. The results of these measurements are plotted in Figure 6.8. In Figure 6.8(a), the time-integrated optomechanical response of two QDs inside a ring resonator of $24\ \mu\text{m}$ diameter is shown in a false-colour plot as a function of the applied frequency f_{rf} for an applied rf power of 10 dBm. The two QDs are measured simultaneously and located close to each other but separated spectrally. The arrows in the plot show the different resonant modes and the frequencies at which each time-resolved measurement plotted below is done: 298.6 MHz (b), 402.6 MHz (c), 479 MHz (d), 558.4 MHz (e) and 779 MHz (f). The QD's emission is clearly modulated in a sinusoidal fashion. Additionally, for each time-resolved plot, a sinusoidal best fit is plotted on top of the false-colour plot following the QD emission line's modulation. From these fits, the period of the modulation can be extracted and it follows exactly the period of SAW excited by the applied rf signal, $T = f_{rf}^{-1}$, for all the data plots.

From the work of Fu and coworkers, we know that phononic modes can be supported in ring resonators fabricated on an equivalent hybrid platform [87]. Additionally, we have proven that the modes we observe in the optomechanical response of the dots have the same sinusoidal shape and the same frequency as the SAW exciting them. In conclusion, we argue that they are indeed phononic modes confined to the ring resonator and excited by the SAW emitted by the chirped IDT.

6.4.1 Power dependence of the phononic modes: Duffing oscillator behaviour

The shape of a simple mechanical resonance should be symmetrical but a closer look at the mode presented in the last section shows that the peak form is asymmetric, as shown

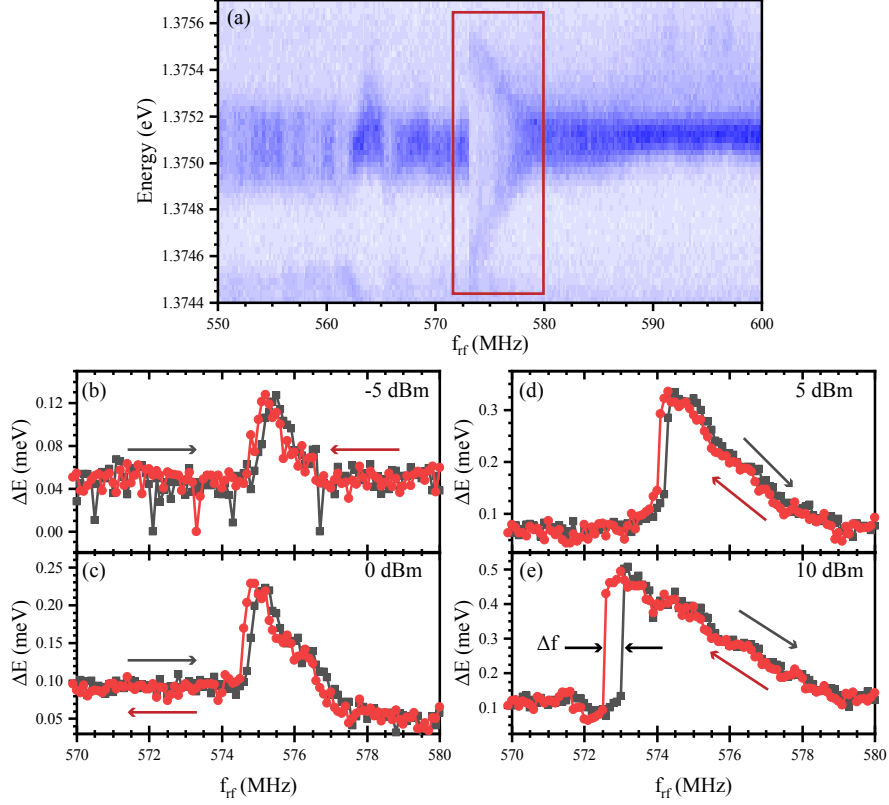


Figure 6.9: (a) False colour plot of the time-integrated spectrum of a QD's emission line as a function of the applied rf frequency f_{rf} in a ring resonator of $24 \mu\text{m}$ diameter for $P_{rf} = 10 \text{ dBm}$. The phononic mode analysed is indicated by the red rectangle in the plot. (b-e) Modulation of the emission line energy ΔE extracted from the fit of the time-integrated spectrum of the QD's emission line as a function of the applied rf frequency f_{rf} and for four different rf power P_{rf} : -5 dBm (b), 0 dBm (c), 5 dBm (d) and 10 dBm (e). f_{rf} is first increased (black square) and then decreased (red circles) and the direction of the frequency evolution is indicated by the arrows in the plots.

clearly in Figure 6.9(a) in the false colour plot of a QD's emission line. This type of asymmetry in the mechanical resonance is often observed in micro- or nano-electro-mechanical-system (MEMS/NEMS) resonators and their motion is then characterised by a nonlinear ordinary differential equations (ODE), the Duffing equation [88]. This equation of motion introduces non-linear damping terms such as cubic terms as shown in the following equation:

$$\frac{d^2u}{dt^2} + \mu \frac{du}{dt} + \lambda^2 u + k_2 u^2 + k_3 u^3 = K \cos(\omega t) \quad (6.5)$$

where u is the displacement of the oscillator, t is time, μ is the damping coefficient, λ^2 is the linear stiffness coefficient, K is the amplitude of the periodic driving force and ω its frequency. The quadratic and cubic terms with the coefficients k_2 and k_3 introduce the non-linearity in the motion of the resonator [88].

To confirm that the asymmetric shape of our phononic modes could be due to such non-linearities, a frequency and power sweep is done on one of the modes. The mode which is analysed is presented in Figure 6.9(a) in a time-integrated measurement of a QD emission line and indicated by a red rectangle. The measurement of the QD's emission line modulation by the SAW is done for different rf power $P_{rf} = [-5 : 5 : 10]$ dBm and, for each power P_{rf} , the applied frequency f_{rf} is increased and then decreased in the range $f_{rf} = [565 : 585]$ MHz. The modulation of the emission line energy ΔE is extracted by fitting the time-integrated spectra of the QD and is plotted in Figure 6.9(b), (c), (d) and (e) for the applied rf power $P_{rf} = -5, 0, 5$ and 10 dBm, respectively. The arrows in the plot show the direction of the frequency evolution with the black rectangle for increasing f_{rf} and the red circles for the decreasing f_{rf} .

The plots in Figure 6.9(b-e) show a typical frequency response of a Duffing resonator. As the driving force, here P_{rf} , increases, the resonance becomes broader and the frequency associated with the maximum amplitude of ΔE moves away from the resonator eigenfrequency f_0 , defined at lower power. The characteristic shark-fin shape of the resonance for the duffing oscillator can then be observed at higher driving power when the resonator is entering the non-linear regime. In this case, the equation has two stable solutions, which leads to the jump in the resonator response ΔE on the left side of the flank [88, 89, 90]. In this case, the frequency shifts to lower frequencies which indicates a softening of the effective elastic constant of the resonator. A clear hysteresis, Δf in Figure 6.9(e), can also be observed between the increasing frequency sweep and the decreasing one. This hysteresis is a characteristic of the non-linear behaviour of Duffing oscillators. In this case, the hysteresis Δf increases from 0.2 MHz to 0.5 MHz when the driving power increases from -5 dBm to 10 dBm.

All in all, the phononic modes detected in this ring resonator system show all the typical characteristics of a non-linear Duffing oscillator. The reason behind this non-linear behaviour is not yet understood and deserves further investigations to understand this phononic resonances at a more fundamental level.

Conclusion

In this chapter, the fabrication of complex photonic structures made from a transferred GaAs membrane on a LiNbO₃ substrate is proven to be successful. The influence of the SAW on the QDs and the ring resonators is analysed. The tuning of a QD in and out of resonance with the cavity mode is shown and the modulation of both signals by the SAW is identified using FDTD simulations of the ring resonator. The presence of phononic modes excited by the SAW is shown in the resonators and they are proven to have the same frequency as the exciting SAW and to modulate the QDs in the same sinusoidal manner as the SAW. The phononic modes also show a non-linear behaviour which is highlighted by an analysis of their frequency response with increasing applied rf power. The resonance displays a shark-fin shape at higher driving power and a frequency hysteresis which are typical for Duffing oscillator. The origin for the presence of these modes and their non-linear behaviour has to be further investigated.

Conclusion and Perspectives

This work was focussed on the optomechanical modulation of semiconductor QDs by surface acoustic waves and the possibility to enhance this interaction by transferring the QDs onto a strong piezoelectric substrate. The epitaxial lift-off technique used to integrate a III-V semiconductor QD membrane inside a LiNbO₃ SAW-chip was introduced. The fabrication was proven to be successful and the post-processing of the membrane into more complex structure such as ring resonators and waveguides was shown.

The coupling of the SAW to such a transferred epilayer was subsequently analysed first using finite element method simulations. These simulations showed that the acoustic field becomes localised inside the membrane as the SAW frequency increases. The optomechanical coupling parameter for the hybrid structure was calculated and was shown to be larger than the one of monolithic structure for higher frequencies. An optomechanical coupling parameter of $\gamma_{OM} > 25 \text{ meV nm}^{-1}$ was calculated for thin membranes at SAW frequencies of $f_{SAW} \approx 3 \text{ GHz}$. Secondly, a LiNbO₃-(Al)GaAs hybrid device was fabricated and the successful coupling of the acoustic field inside the semiconductor membrane was proven. The Split-52 delay line enabled the excitation and the detection of SAWs across the membrane at varying frequencies and the simultaneous measurement of the optomechanical response of the dots in the membrane showed an enhancement of the QD's coupling to the acoustic field for increasing frequencies.

To further increase the sound-matter coupling, the acoustic field modulating the QDs was confined by embedding the epitaxial membrane inside a SAW resonator cavity. The coupling of QD's excitons to the phononic modes of the SAW cavity was proven to be successful. Even after the transfer of the QD membrane inside the cavity, the quality factor of the resonator remained high at around $Q \sim 2500 - 3000$, which ensured the coherent behaviour of the acoustic field. The coupling between the QDs and the modes was shown to be index dependent as the localisation of the dots in the standing wave pattern of the SAW influenced their coupling to the resonator modes. Additionally, the frequency-dependent response of the QD's emission showed a complex behaviour with the presence of frequency mixed peaks in the optomechanical response. The dependence of the amplitude of the QD's optomechanical response on the input rf power did not follow a classical $P_{rf}^{1/2}$ or P_{rf}^1 power dependence and displayed an exponent $1/2 < m < 1$. In addition to the experiments, the finite element simulations performed in 2D showed no indication of a mechanical origin for these features and a non-linear frequency conversion was taken to be a plausible cause for this complex behaviour.

The fabrication of more complex photonic structures such as ring resonators by the post-processing of the QD membrane was demonstrated in collaboration with the Toshiba Research Lab in Cambridge. The SAW was used to tune the QD in and out of resonance with the optical cavity mode of the ring resonator. The modulation of both the QD's emission energy and the cavity mode was identified using FDTD simulations. The ring resonators also presented phononic modes which could be detected in the frequency-dependent response of the QDs. These modes were proven to have the same frequency and sinusoidal form as the SAW exciting them. The phononic modes showed a non-linear behaviour which was highlighted by an analysis of their frequency response with increasing applied rf power. The resonance displayed a shark-fin shape at higher driving powers and a frequency hysteresis which are typical for Duffing oscillator.

Based on the results presented in this work, there are possibilities to continue this work. To understand the possible non-linear frequency conversion in the SAW resonator-QD coupling, resonators with higher resonant frequencies can be used. In that case, when the frequency of the SAW phonons exceeds the optical linewidth and the QD is optically driven resonantly, the system is in the resolved sideband regime [20]. In this regime, the contribution of each phonon interaction can be identified in the emission spectrum and the frequency mixing can be confirmed [73]. Additionally, the SAW cavity can be fabricated by etching the SAW cavity into either the LiNbO₃ substrate or the transferred membrane in order to have a smaller mode volume and, thus, a higher coupling [91]. This additional processing of the LiNbO₃ substrate and the semiconductor membrane could be further used to incorporate optically active QDs into LiNbO₃/GaAs photonic circuits [62]. Finally, the investigation of GaAs ring resonators on top of a LiNbO₃ substrate as a phononic structure should be continued as it is not the only system having shown this type of non-linear Duffing oscillator behaviour [92].

Appendices

Materials Parameters

In this appendix, the material parameters of LiNbO_3 , GaAs and $\text{Al}_x\text{Ga}_{(1-x)}\text{As}$ used in the FEM and FDTD simulations presented in the previous chapters are presented. This starts by explaining the Voigt notation used to reduce the order of the material tensors. The rotation of the tensors to adapt to the 2D frame of reference for the simulation is also presented. Finally, the materials parameters used for the simulations presented in the main text.

A.1 Voigt notation

The Voigt notation provides an easy mean to reduce the order of the elastic tensors used to describe the elastic and piezoelectric properties of materials by using their symmetry. This reduces the complexity of the equations and makes it possible to write the stiffness tensor and piezoelectric tensor as matrices. The notation takes two interchangeable indices and replaces them with only one with the following rule:

$$(1, 1) \rightarrow 1 \quad (2, 2) \rightarrow 2 \quad (3, 3) \rightarrow 3 \tag{A.1}$$

$$(2, 3) \rightarrow 4 \quad (1, 3) \rightarrow 5 \quad (1, 2) \rightarrow 6 \tag{A.2}$$

$$\tag{A.3}$$

By applying this rule to the stress tensor T_{ij} , the 3×3 matrices can be reduced to 6-elements vectors:

$$T = \begin{bmatrix} T_{11} & T_{12} & T_{13} \\ \cdot & T_{22} & T_{23} \\ \cdot & \cdot & T_{33} \end{bmatrix} = \begin{bmatrix} T_1 & T_6 & T_5 \\ \cdot & T_2 & T_4 \\ \cdot & \cdot & T_3 \end{bmatrix} \Rightarrow T = \begin{pmatrix} T_1 \\ T_2 \\ T_3 \\ T_4 \\ T_5 \\ T_6 \end{pmatrix} \tag{A.4}$$

The same notation can be applied to the strain tensor S_{ij} . However, in this case, the elements with mixed indices have to be multiplied by two in order to respect the elasticity theory equations in the Voigt notation.

$$S = \begin{bmatrix} S_{11} & S_{12} & S_{13} \\ \cdot & S_{22} & S_{23} \\ \cdot & \cdot & S_{33} \end{bmatrix} = \begin{bmatrix} S_1 & S_6 & S_5 \\ \cdot & S_2 & S_4 \\ \cdot & \cdot & S_3 \end{bmatrix} \Rightarrow S = \begin{pmatrix} S_1 \\ S_2 \\ S_3 \\ 2S_4 \\ 2S_5 \\ 2S_6 \end{pmatrix} \quad (\text{A.5})$$

As stated previously in Chapter 1, the stiffness tensor possesses the symmetries $c_{ijkl} = c_{jikl}$ and $c_{ijkl} = c_{ijlk}$. The Voigt notation applies the mapping rule to the first two indices (i, j) and the last two indices (k, l) . The fourth-rank tensor transforms into a symmetric 6×6 matrix due to the major symmetry:

$$c = \begin{pmatrix} c_{11} & c_{12} & c_{13} & c_{14} & c_{15} & c_{16} \\ \cdot & c_{22} & c_{23} & c_{24} & c_{25} & c_{26} \\ \cdot & \cdot & c_{33} & c_{34} & c_{35} & c_{36} \\ \cdot & \cdot & \cdot & c_{44} & c_{45} & c_{46} \\ \cdot & \cdot & \cdot & \cdot & c_{55} & c_{56} \\ \cdot & \cdot & \cdot & \cdot & \cdot & c_{66} \end{pmatrix} \quad (\text{A.6})$$

In the case of the piezoelectric tensor e_{ijk} , the mapping rule is applied to the last two indices (j, k) leading to a 3×6 matrix with the first index i corresponding to the electric field:

$$e = \begin{pmatrix} e_{11} & e_{12} & e_{13} & e_{14} & e_{15} & e_{16} \\ e_{21} & e_{22} & e_{23} & e_{24} & e_{25} & e_{26} \\ e_{31} & e_{32} & e_{33} & e_{34} & e_{35} & e_{36} \end{pmatrix} \quad (\text{A.7})$$

Using the Voigt notation with the indices α and β , the definition of stress (equation 1.4) and the electric displacement (equation 1.5) for a piezoelectric material can be written as:

$$T_\alpha = c_{\alpha\beta} S_\beta - e_{\alpha i} F_i \quad (\text{A.8})$$

$$D_i = e_{i\alpha} S_\alpha + \epsilon F_i \quad (\text{A.9})$$

A.2 Rotation matrices

To adapt the material parameter tensors to the system of reference used in the FEM simulations, the matrices have to be rotated. In the case of LiNbO_3 , the 2D plane selected for the simulation is the XZ-plane and the material parameters are rotated by -38° around the X axis. For GaAs and $\text{Al}_x\text{Ga}_{(1-x)}\text{As}$, the rotation is a -45° rotation around the Z axis in order for the wave to propagate along the compact direction. The usual rotation matrices cannot be used for the Voigt notation of the tensors. To keep the reduced order given by the Voigt notation, the Bond rotation matrices are used, which allows the rotation of the stiffness tensor by a simple matrix multiplication [93]. For a clockwise rotation of an angle α around the Z axis, the Bond matrix K is given by:

$$K_Z = \begin{pmatrix} \cos(\alpha)^2 & \sin(\alpha)^2 & 0 & 0 & 0 & -2\cos(\alpha)\sin(\alpha) \\ \sin(\alpha)^2 & \cos(\alpha)^2 & 0 & 0 & 0 & 2\cos(\alpha)\sin(\alpha) \\ 0 & 0 & 1 & 0 & 0 & 0 \\ 0 & 0 & 0 & \cos(\alpha) & \sin(\alpha) & 0 \\ 0 & 0 & 0 & -\sin(\alpha) & \cos(\alpha) & 0 \\ \cos(\alpha)\sin(\alpha) & -\cos(\alpha)\sin(\alpha) & 0 & 0 & 0 & \cos(\alpha)^2 - \sin(\alpha)^2 \end{pmatrix} \quad (\text{A.10})$$

and, for a rotation α around the X axis, the matrix is given by:

$$K_X = \begin{pmatrix} 1 & 0 & 0 & 0 & 0 & 0 \\ 0 & \cos(\alpha)^2 & \sin(\alpha)^2 & -2\cos(\alpha)\sin(\alpha) & 0 & 0 \\ 0 & \sin(\alpha)^2 & \cos(\alpha)^2 & 2\cos(\alpha)\sin(\alpha) & 0 & 0 \\ 0 & \cos(\alpha)\sin(\alpha) & -\cos(\alpha)\sin(\alpha) & \cos(\alpha)^2 - \sin(\alpha)^2 & 0 & 0 \\ 0 & 0 & 0 & 0 & \cos(\alpha) & \sin(\alpha) \\ 0 & 0 & 0 & 0 & -\sin(\alpha) & \cos(\alpha) \end{pmatrix} \quad (\text{A.11})$$

With these matrices, the rotated stiffness tensor c_{rot} is given by:

$$c_{rot} = K \cdot c \cdot K^T \quad (\text{A.12})$$

For the piezoelectric and permittivity tensor, the usual rotation matrices are needed and the rotation around the X and Z axis are given by:

$$R_Z = \begin{pmatrix} \cos(\alpha) & -\sin(\alpha) & 0 \\ \sin(\alpha) & \cos(\alpha) & 0 \\ 0 & 0 & 1 \end{pmatrix} \quad R_X = \begin{pmatrix} 1 & 0 & 0 \\ 0 & \cos(\alpha) & -\sin(\alpha) \\ 0 & \sin(\alpha) & \cos(\alpha) \end{pmatrix} \quad (\text{A.13})$$

The tensors are then given by:

$$e_{rot} = (K \cdot e^T \cdot R^T)^T \quad (\text{A.14})$$

$$\epsilon_{rot} = R \cdot \epsilon \cdot R^T \quad (\text{A.15})$$

A.3 LiNbO₃ material parameters

LiNbO₃ has a trigonal crystal structure and belongs to the $3m$ point group. Its density is equal to $\rho = 4700 \text{ kg m}^{-3}$. The stiffness, piezoelectric and relative permittivity tensors at room temperature (300 K) are given by [94, 26]:

$$c = \begin{pmatrix} 203 & 53 & 75 & 9 & 0 & 0 \\ \cdot & 203 & 75 & -9 & 0 & 0 \\ \cdot & \cdot & 245 & 0 & 0 & 0 \\ \cdot & \cdot & \cdot & 60 & 0 & 0 \\ \cdot & \cdot & \cdot & \cdot & 60 & 18 \\ \cdot & \cdot & \cdot & \cdot & \cdot & 75 \end{pmatrix} \text{GPa} \quad (\text{A.16})$$

$$e = \begin{pmatrix} 0 & 0 & 0 & 0 & 3.7 & -2.5 \\ -2.5 & 2.5 & 0 & 3.7 & 0 & 0 \\ 0.2 & 0.2 & 1.3 & 0 & 0 & 0 \end{pmatrix} \text{C m}^{-2} \quad \epsilon = \begin{pmatrix} 43.6 & 0 & 0 \\ 0 & 43.6 & 0 \\ 0 & 0 & 29.2 \end{pmatrix} \quad (\text{A.17})$$

When the sample is cooled in the cryostat, the material parameters change with the decreasing temperature. The parameters at lower temperatures are linearly interpolated using experimentally determined temperature coefficients δ [95]. The parameter are then calculated by:

$$p = p_0 \cdot (1 + \delta \cdot (T - 300)) \quad (\text{A.18})$$

where p_0 is the parameter value at the temperature of reference, 300 K. The temperature coefficient used here are given in Table A.1.

By taking temperature inside the cryostat to be equal to 10 K and by rotating the tensors around the X axis for -38° to achieve the LiNbO₃-128° Y-X cut, the material parameters used in the 2D FEM simulations in Chapters for the simulations in Chapters 4, 5 and 6 are:

Parameter	$\delta (\times 10^{-4} \text{ K}^{-1})$	Parameter	$\delta (\times 10^{-4} \text{ K}^{-1})$
c_{11}	-1.74	e_{15}	1.47
c_{12}	-2.52	e_{22}	0.79
c_{13}	-1.59	e_{31}	2.21
c_{14}	-2.14	e_{33}	8.87
c_{33}	-1.53	ϵ_{11}	3.23
c_{44}	-2.04	ϵ_{33}	6.27
c_{66}	-1.43		

Table A.1: Temperature coefficient for the material parameter of LiNbO_3 [95].

$$c = \begin{pmatrix} 213 & 74.3 & 60.7 & 12.5 & 0 & 0 \\ \cdot & 204 & 94.1 & 10.1 & 0 & 0 \\ \cdot & \cdot & 233 & 8.49 & 0 & 0 \\ \cdot & \cdot & \cdot & 79.6 & 0 & 0 \\ \cdot & \cdot & \cdot & \cdot & 60.2 & -5.39 \\ \cdot & \cdot & \cdot & \cdot & \cdot & 82.7 \end{pmatrix} \text{ GPa} \quad (\text{A.19})$$

$$e = \begin{pmatrix} 0 & 0 & 0 & 0 & 4.24 & 0.264 \\ -1.77 & 4.15 & -1.54 & -0.0173 & 0 & 0 \\ 1.63 & -2.63 & 2.06 & 0.49 & 0 & 0 \end{pmatrix} \text{ C m}^{-2} \quad (\text{A.20})$$

$$\epsilon = \begin{pmatrix} 39.5 & 0 & 0 \\ 0 & 33.5 & -7.67 \\ 0 & -7.67 & 29.7 \end{pmatrix} \quad (\text{A.21})$$

A.4 GaAs material parameters

The cubic crystal structure of GaAs and point group $\bar{4}3m$ reduces the number of independent components for the stiffness tensor to only 3 and for the piezoelectric and relative permittivity tensor to only one. Its density is equal to $\rho = 5332 \text{ kg m}^{-3}$. The stiffness, piezoelectric and relative permittivity tensors at room temperature (300 K) are given by [43, 26]:

$$c = \begin{pmatrix} 118.8 & 53.8 & 53.8 & 0 & 0 & 0 \\ \cdot & 118.8 & 53.8 & 0 & 0 & 0 \\ \cdot & \cdot & 118.8 & 0 & 0 & 0 \\ \cdot & \cdot & \cdot & 59.4 & 0 & 0 \\ \cdot & \cdot & \cdot & \cdot & 59.4 & 0 \\ \cdot & \cdot & \cdot & \cdot & \cdot & 59.4 \end{pmatrix} \text{GPa} \quad (\text{A.22})$$

$$e = \begin{pmatrix} 0 & 0 & 0 & -0.16 & 0 & 0 \\ 0 & 0 & 0 & 0 & -0.16 & 0 \\ 0 & 0 & 0 & 0 & 0 & -0.16 \end{pmatrix} \text{C m}^{-2} \quad (\text{A.23})$$

$$\epsilon = \begin{pmatrix} 13.18 & 0 & 0 \\ 0 & 13.18 & 0 \\ 0 & 0 & 13.18 \end{pmatrix} \quad (\text{A.24})$$

The temperature dependence of the GaAs material parameters is given by [96, 97]:

$$c_{11} = 118.8 - 13.9 \cdot 10^{-3} \cdot (T - 300) \quad \text{GPa} \quad (\text{A.25})$$

$$c_{12} = 53.8 - 5.76 \cdot 10^{-3} \cdot (T - 300) \quad \text{GPa} \quad (\text{A.26})$$

$$c_{44} = 59.4 - 7.01 \cdot 10^{-3} \cdot (T - 300) \quad \text{GPa} \quad (\text{A.27})$$

$$\epsilon_{11} = 12.35 \cdot (1 + 2.01 \cdot 10^{-4} \cdot T) \quad (\text{A.28})$$

The piezoelectric tensor is considered to stay constant. Once again taking the temperature inside the cryostat to be equal to 10 K and by rotating the tensors around the Z axis for -45° to have SAW propagating in the compact direction, the material parameters used in the 2D FEM simulations in Chapter 6 are:

$$c = \begin{pmatrix} 150.6 & 27.8 & 55.5 & 0 & 0 & 0 \\ \cdot & 150.6 & 55.5 & 0 & 0 & 0 \\ \cdot & \cdot & 122.8 & 0 & 0 & 0 \\ \cdot & \cdot & \cdot & 61.4 & 0 & 0 \\ \cdot & \cdot & \cdot & \cdot & 61.4 & 0 \\ \cdot & \cdot & \cdot & \cdot & \cdot & 33.7 \end{pmatrix} \text{GPa} \quad (\text{A.29})$$

$$e = \begin{pmatrix} 0 & 0 & 0 & 0 & -0.16 & 0 \\ 0 & 0 & 0 & 0.16 & 0 & 0 \\ -0.16 & 0.16 & 0 & 0 & 0 & 0 \end{pmatrix} \text{C m}^{-2} \quad (\text{A.30})$$

$$\epsilon = \begin{pmatrix} 12.4 & 0 & 0 \\ 0 & 12.4 & 0 \\ 0 & 0 & 12.4 \end{pmatrix} \quad (\text{A.31})$$

A.4.1 Elasto-optic tensor of GaAs

The elasto-optic parameters used in the FDTD simulations presented in Chapter 6 are given here [98]:

$$p = \begin{pmatrix} -0.184 & -0.172 & -0.172 & 0 & 0 & 0 \\ \cdot & -0.184 & -0.172 & 0 & 0 & 0 \\ \cdot & \cdot & -0.184 & 0 & 0 & 0 \\ \cdot & \cdot & \cdot & -0.5 & 0 & 0 \\ \cdot & \cdot & \cdot & \cdot & -0.5 & 0 \\ \cdot & \cdot & \cdot & \cdot & \cdot & -0.5 \end{pmatrix} \quad (\text{A.32})$$

A.5 $\text{Al}_x\text{Ga}_{(1-x)}\text{As}$ material parameters

The material parameters of $\text{Al}_x\text{Ga}_{(1-x)}\text{As}$ can be linearly interpolated between the ones of GaAs and AlAs as a function of the Al content x [43]:

$$\rho = \rho^{\text{GaAs}} - 1560 \cdot x \quad \text{kg m}^{-3} \quad (\text{A.33})$$

$$c_{11} = c_{11}^{\text{GaAs}}(T) + 1.4 \cdot x \quad \text{GPa} \quad (\text{A.34})$$

$$c_{12} = c_{12}^{\text{GaAs}}(T) + 3.2 \cdot x \quad \text{GPa} \quad (\text{A.35})$$

$$c_{44} = c_{44}^{\text{GaAs}}(T) + 0.5 \cdot x \quad \text{GPa} \quad (\text{A.36})$$

$$e_{14} = e_{14}^{\text{GaAs}}(T) - 0.065 \cdot x \quad \text{C m}^{-2} \quad (\text{A.37})$$

$$\epsilon_{11} = \epsilon^{\text{GaAs}}(T) - 3.12 \cdot x \quad (\text{A.38})$$

Using the parameters of GaAs at 10 K, an Al content of $x = 0.33$ and a rotation of -45° around the Z axis, the parameters used for the simulations in Chapters 4 and 5 are:

$$c = \begin{pmatrix} 151.2 & 28.8 & 56.6 & 0 & 0 & 0 \\ \cdot & 151.2 & 56.6 & 0 & 0 & 0 \\ \cdot & \cdot & 123.3 & 0 & 0 & 0 \\ \cdot & \cdot & \cdot & 61.2 & 0 & 0 \\ \cdot & \cdot & \cdot & \cdot & 61.2 & 0 \\ \cdot & \cdot & \cdot & \cdot & \cdot & 33.4 \end{pmatrix} \text{GPa} \quad (\text{A.39})$$

$$e = \begin{pmatrix} 0 & 0 & 0 & 0 & -0.183 & 0 \\ 0 & 0 & 0 & 0.183 & 0 & 0 \\ -0.183 & 0.183 & 0 & 0 & 0 & 0 \end{pmatrix} \text{C m}^{-2} \quad (\text{A.40})$$

$$\epsilon = \begin{pmatrix} 11.4 & 0 & 0 \\ 0 & 11.4 & 0 \\ 0 & 0 & 11.4 \end{pmatrix} \quad (\text{A.41})$$

and a density of $\rho = 4817 \text{ kg m}^{-3}$.

List of Symbols

\mathbf{u}	displacement
\mathbf{x}	scalar system
S_{ij}	strain tensor
T_{ij}	stress tensor
c_{ijkl}	stiffness tensor
ρ	material density
\mathbf{F}	electrical field
\mathbf{D}	electrical displacement
e_{ijk}	piezoelectric tensor
ϵ_{ij}	permittivity tensor
ϵ	dielectric constant
\mathbf{B}	magnetic field
Φ	electrical potential
v_{SAW}/c_{SAW}	wave velocity
K	electromechanical coupling coefficient
ϵ_0	vacuum permittivity
λ	wavelength
f	frequency
L_{IDT}	IDT length
A_{IDT}	IDT aperture
a	width of IDT electrode
p	pitch of IDT electrode
a/p	metallisation ratio
$H(f)$	frequency response function
T	time period
p_{ij}	p-matrix elements
r_s	reflection parameter of an electrode

t_s	transmission parameter of an electrode
k	wavenumber/wavevector
ω	angular frequency
ϕ	phase
α	attenuation coefficient
L_p	penetration length of the SAW in the grating
τ_g	delay of the SAW in the grating
h	thickness of a metal electrode
Δ / d	distance between a resonator gratings
L_c	cavity length of a resonator
N	number of electrodes
$Q_{i/e}$	internal/external quality factor
S_{11}/S_{12}	reflection/transmission scattering parameter
E_g	bandgap energy
c	lattice constant
m^*	effective mass
Δ_{so}	split-off energy difference
e	electron charge
μ	effective reduced mass
r_X	exciton radius
C	bowing parameter
E/E_n	energy/energy level
$X^0/X^+/X^-$	neutral/charged exciton
$2X^0$	neutral biexciton
V^{xx}	Coulomb interaction between charge carrier
β	polarisability of an exciton
p	pressure
t_d	time delay
x	alloy composition
ΔE	energy difference or energy modulation of the QD's emission by the SAW
γ_{OM}	optomechanical coupling parameter
n	refractive index
p_{ijkl}	elasto-optic tensor

List of Acronyms

SAW	surface acoustic wave
IDT	interdigital transducer
QD	quantum dot
rf	radio frequency
RAM	reflective array model
FSR	free spectral range
fcc	face centred cubic lattice
PL	photoluminescence
QW	quantum well
μ -PL	micro-photoluminescence
STCD	spatio-temporal carrier dynamics
QCSE	quantum confined stark effect
DPC	deformation potential coupling
cw	continuous wave
CCD	charged coupled device
SPAD	single photon avalanche diode
TCSPC	time-correlated single photon counting
LDE	local droplet etching
EBL	electron beam lithography
ELO	epitaxial lift-off
FIB	focussed ion beam
TEM	transmission electron microscope
SEM	scanning electron microscope
EDX	energy dispersive X-ray
RIE	reactive ion etching
FEM	finite element method
FFT	fast Fourier transform

VNA vector network analyser
FDTD finite-difference time domain method
PML perfectly matched layers

Bibliography

- [1] Gershon Kurizki, Patrice Bertet, Yuimaru Kubo, Klaus Mølmer, David Petrosyan, Peter Rabl, and Jörg Schmiedmayer. Quantum technologies with hybrid systems. *Proceedings of the National Academy of Sciences*, 112(13):3866–3873, mar 2015.
- [2] Per Delsing, Andrew N Cleland, Martin J A Schuetz, Johannes Knörzer, Géza Giedke, J Ignacio Cirac, Kartik Srinivasan, Marcelo Wu, Krishna Coimbatore Balram, Christopher Bäuerle, Tristan Meunier, Christopher J B Ford, Paulo V Santos, Edgar Cerda-Méndez, Hailin Wang, Hubert J Krenner, Emeline D S Nysten, Matthias Weiß, Geoff R Nash, Laura Thevenard, Catherine Gourdon, Pauline Rovillain, Max Marangolo, Jean-Yves Duquesne, Gerhard Fischerauer, Werner Ruile, Alexander Reiner, Ben Paschke, Dmytro Denysenko, Dirk Volkmer, Achim Wixforth, Henrik Bruus, Martin Wiklund, Julien Reboud, Jonathan M Cooper, YongQing Fu, Manuel S Brugger, Florian Rehfeldt, and Christoph Westerhausen. The 2019 surface acoustic waves roadmap. *Journal of Physics D: Applied Physics*, 52(35):353001, jul 2019.
- [3] M. J. A. Schuetz, E. M. Kessler, G. Giedke, L. M. K. Vandersypen, M. D. Lukin, and J. I. Cirac. Universal quantum transducers based on surface acoustic waves. *Physical Review X*, 5(3), sep 2015.
- [4] Ralf Blattmann, Hubert J. Krenner, Sigmund Kohler, and Peter Hänggi. Entanglement creation in a quantum-dot–nanocavity system by fourier-synthesized acoustic pulses. *Physical Review A*, 89(1), jan 2014.
- [5] M. V. Gustafsson, T. Aref, A. F. Kockum, M. K. Ekstrom, G. Johansson, and P. Delsing. Propagating phonons coupled to an artificial atom. *Science*, 346(6206):207–211, sep 2014.
- [6] R. Manenti, M. J. Peterer, A. Nersisyan, E. B. Magnusson, A. Patterson, and P. J. Leek. Surface acoustic wave resonators in the quantum regime. *Physical Review B*, 93(4), jan 2016.
- [7] Riccardo Manenti, Anton F. Kockum, Andrew Patterson, Tanja Behrle, Joseph Rahamim, Giovanna Tancredi, Franco Nori, and Peter J. Leek. Circuit quantum

- acoustodynamics with surface acoustic waves. *Nature Communications*, 8(1), oct 2017.
- [8] A. Bienfait, K. J. Satzinger, Y. P. Zhong, H.-S. Chang, M.-H. Chou, C. R. Conner, É. Dumur, J. Grebel, G. A. Peairs, R. G. Povey, and A. N. Cleland. Phonon-mediated quantum state transfer and remote qubit entanglement. *Science*, 364(6438):368–371, apr 2019.
- [9] Sylvain Hermelin, Shintaro Takada, Michihisa Yamamoto, Seigo Tarucha, Andreas D. Wieck, Laurent Saminadayar, Christopher Bäuerle, and Tristan Meunier. Electrons surfing on a sound wave as a platform for quantum optics with flying electrons. *Nature*, 477(7365):435–438, sep 2011.
- [10] R. P. G. McNeil, M. Kataoka, C. J. B. Ford, C. H. W. Barnes, D. Anderson, G. A. C. Jones, I. Farrer, and D. A. Ritchie. On-demand single-electron transfer between distant quantum dots. *Nature*, 477(7365):439–442, sep 2011.
- [11] B. Bertrand, S. Hermelin, S. Takada, M. Yamamoto, S. Tarucha, A. Ludwig, A. D. Wieck, C. Bäuerle, and T. Meunier. Fast spin information transfer between distant quantum dots using individual electrons. *Nature Nanotechnology*, 11(8):672–676, may 2016.
- [12] Tzu-Kan Hsiao, Antonio Rubino, Yousun Chung, Seok-Kyun Son, Hangtian Hou, Jorge Pedrós, Ateeq Nasir, Gabriel Éthier-Majcher, Megan J. Stanley, Richard T. Phillips, Thomas A. Mitchell, Jonathan P. Griffiths, Ian Farrer, David A. Ritchie, and Christopher J. B. Ford. Single-photon emission from single-electron transport in a SAW-driven lateral light-emitting diode. *Nature Communications*, 11(1), feb 2020.
- [13] Matthias Weiß and Hubert J. Krenner. Interfacing quantum emitters with propagating surface acoustic waves. *Journal of Physics D: Applied Physics*, 51(37):373001, aug 2018.
- [14] Stefan Völk, Florian J. R. Schülein, Florian Knall, Dirk Reuter, Andreas D. Wieck, Tuan A. Truong, Hyochul Kim, Pierre M. Petroff, Achim Wixforth, and Hubert J. Krenner. Enhanced sequential carrier capture into individual quantum dots and quantum posts controlled by surface acoustic waves. *Nano Letters*, 10(9):3399–3407, aug 2010.
- [15] Stefan Völk, Florian Knall, Florian J R Schülein, Tuan A Truong, Hyochul Kim, Pierre M Petroff, Achim Wixforth, and Hubert J Krenner. Surface acoustic wave mediated carrier injection into individual quantum post nano emitters. *Nanotechnology*, 23(28):285201, jun 2012.
- [16] S. Völk, F. Knall, F. J. R. Schülein, T. A. Truong, H. Kim, P. M. Petroff, A. Wixforth, and H. J. Krenner. Direct observation of dynamic surface acoustic wave controlled carrier injection into single quantum posts using phase-resolved optical spectroscopy. *Applied Physics Letters*, 98(2):023109, jan 2011.

- [17] Hubert J. Krenner, Stefan Völk, Florian J. R. Schülein, Florian Knall, Achim Wixforth, Dirk Reuter, Andreas D. Wieck, Hyochul Kim, Tuan A. Truong, and Pierre M. Petroff. Surface acoustic wave controlled carrier injection into self-assembled quantum dots and quantum posts. *physica status solidi (c)*, 9(2):407–410, nov 2011.
- [18] Florian J. R. Schülein, Kai Müller, Max Bichler, Gregor Koblmüller, Jonathan J. Finley, Achim Wixforth, and Hubert J. Krenner. Acoustically regulated carrier injection into a single optically active quantum dot. *Physical Review B*, 88(8), aug 2013.
- [19] J. R. Gell, M. B. Ward, R. J. Young, R. M. Stevenson, P. Atkinson, D. Anderson, G. A. C. Jones, D. A. Ritchie, and A. J. Shields. Modulation of single quantum dot energy levels by a surface-acoustic-wave. *Applied Physics Letters*, 93(8):081115, aug 2008.
- [20] M. Metcalfe, S. M. Carr, A. Muller, G. S. Solomon, and J. Lawall. Resolved sideband emission of InAs/GaAs Quantum dots strained by surface acoustic waves. *Physical Review Letters*, 105(3), jul 2010.
- [21] Florian J. R. Schülein, Eugenio Zallo, Paola Atkinson, Oliver G. Schmidt, Rinaldo Trotta, Armando Rastelli, Achim Wixforth, and Hubert J. Krenner. Fourier synthesis of radiofrequency nanomechanical pulses with different shapes. *Nature Nanotechnology*, 10(6):512–516, apr 2015.
- [22] Eli Yablonovitch, T. Gmitter, J. P. Harbison, and R. Bhat. Extreme selectivity in the lift-off of epitaxial GaAs films. *Applied Physics Letters*, 51(26):2222–2224, dec 1987.
- [23] E. Yablonovitch, D. M. Hwang, T. J. Gmitter, L. T. Florez, and J. P. Harbison. Van der waals bonding of GaAs epitaxial liftoff films onto arbitrary substrates. *Applied Physics Letters*, 56(24):2419–2421, jun 1990.
- [24] Jens Pustowski, Kai Müller, Max Bichler, Gregor Koblmüller, Jonathan J. Finley, Achim Wixforth, and Hubert J. Krenner. Independent dynamic acousto-mechanical and electrostatic control of individual quantum dots in a LiNbO₃-GaAs hybrid. *Applied Physics Letters*, 106(1):013107, jan 2015.
- [25] David Morgan. *Surface Acoustic Wave Filters: With Applications to Electronic Communications and Signal Processing*. Academic Press, Elsevier Ltd, 2nd edition edition, 2007.
- [26] Daniel Royer and Eugène Dieulesaint. *Elastic Waves in Solids I: Free and Guided Propagation*, volume 1. Springer, 1996.
- [27] Daniel Royer and Eugène Dieulesaint. *Elastic Waves in Solids II: Generation, Acousto-optic Interaction, Applications*, volume 2. Springer, 1999.
- [28] Supriyo Datta. *Surface Acoustic Wave Devices*. Prentice-Hall, 1986.

- [29] Lord Rayleigh. On waves propagated along the plane surface of an elastic solid. *Proceedings of the London Mathematical Society*, s1-17(1):4–11, nov 1885.
- [30] Matthias Weiß, Andreas L. Hörner, Eugenio Zallo, Paola Atkinson, Armando Rastelli, Oliver G. Schmidt, Achim Wixforth, and Hubert J. Krenner. Multi-harmonic frequency-chirped transducers for surface-acoustic-wave optomechanics. *Physical Review Applied*, 9(1), jan 2018.
- [31] R.H. Tancrell and M.G. Holland. Acoustic surface wave filters. *Proceedings of the IEEE*, 59(3):393–409, 1971.
- [32] Florian J. R. Schüle. *Dynamische Kontrolle optisch aktiver Halbleiter-Quantenpunkte mittels akustischer Oberflächenwellen*. phdthesis, Universität Augsburg, 2014.
- [33] Matthias Weiß. *Quantum Dot Optomechanics with Surface Acoustic Waves*. phdthesis, Universität Augsburg, 2021.
- [34] Shen Jen and C. S. Hartmann. An improved model for chirped slanted saw devices. *IEEE Ultrasonic Symposium*, 1:7–14, 1989.
- [35] S. Mitobe N. Mishima, M. Takase and Y. Ebata. Iidt type saw filter using acoustic reflection cancel condition with solid idt. *IEEE Ultrasonic Symposium*, 1:31–35, 1989.
- [36] Mark Fox. *Optical Properties of Solids*. Oxford University Press, 2010.
- [37] Mark Fox. *Quantum Optics: An introduction*. Oxford University Press, 2006.
- [38] Oliver Gywat, Hubert J. Krenner, and Jesse Berezovsky. *Spins in Optically Active Quantum Dots: Concepts and Methods*. Wiley VCH, 2010.
- [39] NSM archive - physical properties of semiconductors. URL - <http://www.ioffe.ru/SVA/NSM/Semicond/GaAs/bandstr.html>.
- [40] S. B. Nam, D. C. Reynolds, C. W. Litton, R. J. Almassy, T. C. Collins, and C. M. Wolfe. Free-exciton energy spectrum in GaAs. *Physical Review B*, 13(2):761–767, jan 1976.
- [41] I. Vurgaftman, J. R. Meyer, and L. R. Ram-Mohan. Band parameters for III–v compound semiconductors and their alloys. *Journal of Applied Physics*, 89(11):5815–5875, jun 2001.
- [42] J. A. Van Vechten and T. K. Bergstresser. Electronic structures of semiconductor alloys. *Physical Review B*, 1(8):3351–3358, apr 1970.
- [43] Sadao Adachi. GaAs, AlAs, and Al_xGa_{1-x}As: Material parameters for use in research and device applications. *Journal of Applied Physics*, 58(3):R1–R29, aug 1985.

- [44] Hubert J Krenner, Stefan Stuffer, Matthias Sabathil, Emily C Clark, Patrick Ester, Max Bichler, Gerhard Abstreiter, Jonathan J Finley, and Artur Zrenner. Recent advances in exciton-based quantum information processing in quantum dot nanostructures. *New Journal of Physics*, 7:184–184, aug 2005.
- [45] C. Rocke, S. Zimmermann, A. Wixforth, J. P. Kotthaus, G. Böhm, and G. Weimann. Acoustically driven storage of light in a quantum well. *Physical Review Letters*, 78(21):4099–4102, may 1997.
- [46] C. Rocke, A. O. Govorov, A. Wixforth, G. Böhm, and G. Weimann. Exciton ionization in a quantum well studied by surface acoustic waves. *Physical Review B*, 57(12):R6850–R6853, mar 1998.
- [47] O. D. D. Couto, S. Lazić, F. Iikawa, J. A. H. Stotz, U. Jahn, R. Hey, and P. V. Santos. Photon anti-bunching in acoustically pumped quantum dots. *Nature Photonics*, 3(11):645–648, oct 2009.
- [48] A. Hernández-Mínguez, M. Möller, S. Breuer, C. Pfüller, C. Somaschini, S. Lazić, O. Brandt, A. García-Cristóbal, M. M. de Lima, A. Cantarero, L. Geelhaar, H. Riechert, and P. V. Santos. Acoustically driven photon antibunching in nanowires. *Nano Letters*, 12(1):252–258, dec 2011.
- [49] D. A. B. Miller, D. S. Chemla, T. C. Damen, A. C. Gossard, W. Wiegmann, T. H. Wood, and C. A. Burrus. Band-edge electroabsorption in quantum well structures: The quantum-confined stark effect. *Physical Review Letters*, 53(22):2173–2176, nov 1984.
- [50] Fred H. Pollak and Manuel Cardona. Piezo-electroreflectance in ge, GaAs, and si. *Physical Review*, 172(3):816–837, aug 1968.
- [51] Emeline D S Nysten, Yong Heng Huo, Hailong Yu, Guo Feng Song, Armando Rastelli, and Hubert J Krenner. Multi-harmonic quantum dot optomechanics in fused LiNbO₃–(al)GaAs hybrids. *Journal of Physics D: Applied Physics*, 50(43):43LT01, sep 2017.
- [52] A. P. Litvin, I. V. Martynenko, F. Purcell-Milton, A. V. Baranov, A. V. Fedorov, and Y. K. Gunko. Colloidal quantum dots for optoelectronics. *Journal of Materials Chemistry A*, 5(26):13252–13275, 2017.
- [53] Zh. M. Wang, B. L. Liang, K. A. Sablon, and G. J. Salamo. Nanoholes fabricated by self-assembled gallium nanodrill on GaAs(100). *Applied Physics Letters*, 90(11):113120, mar 2007.
- [54] P. Atkinson, E. Zallo, and O. G. Schmidt. Independent wavelength and density control of uniform GaAs/AlGaAs quantum dots grown by infilling self-assembled nanoholes. *Journal of Applied Physics*, 112(5):054303, sep 2012.
- [55] I. N. Stranski and L. Krastanow. Zur theorie der orientierten ausscheidung von ionenkristallen aufeinander. *Monatshefte für Chemie*, 71(1):351–364, dec 1937.

- [56] L. Goldstein, F. Glas, J. Y. Marzin, M. N. Charasse, and G. Le Roux. Growth by molecular beam epitaxy and characterization of InAs/GaAs strained-layer superlattices. *Applied Physics Letters*, 47(10):1099–1101, nov 1985.
- [57] J. M. Moison, F. Houzay, F. Barthe, L. Leprince, E. André, and O. Vatel. Self-organized growth of regular nanometer-scale InAs dots on GaAs. *Applied Physics Letters*, 64(2):196–198, jan 1994.
- [58] D. Leonard, M. Krishnamurthy, C. M. Reaves, S. P. Denbaars, and P. M. Petroff. Direct formation of quantum-sized dots from uniform coherent islands of InGaAs on GaAs surfaces. *Applied Physics Letters*, 63(23):3203–3205, dec 1993.
- [59] M.M.A.J. Voncken, J.J. Schermer, G.J. Bauhuis, P. Mulder, and P.K. Larsen. Multiple release layer study of the intrinsic lateral etch rate of the epitaxial lift-off process. *Applied Physics A*, 79(7):1801–1807, nov 2004.
- [60] J.J. Schermer, G.J. Bauhuis, P. Mulder, E.J. Haverkamp, J. van Deelen, A.T.J. van Niftrik, and P.K. Larsen. Photon confinement in high-efficiency, thin-film III–v solar cells obtained by epitaxial lift-off. *Thin Solid Films*, 511-512:645–653, jul 2006.
- [61] M.M.A.J Voncken, J.J Schermer, G Maduro, G.J Bauhuis, P Mulder, and P.K Larsen. Influence of radius of curvature on the lateral etch rate of the weight induced epitaxial lift-off process. *Materials Science and Engineering: B*, 95(3):242–248, sep 2002.
- [62] Shahriar Aghaeimeibodi, Boris Desiatov, Je-Hyung Kim, Chang-Min Lee, Mustafa Atabey Buyukkaya, Aziz Karasahin, Christopher J. K. Richardson, Richard P. Leavitt, Marko Lončar, and Edo Waks. Integration of quantum dots with lithium niobate photonics. *Applied Physics Letters*, 113(22):221102, nov 2018.
- [63] Je-Hyung Kim, Shahriar Aghaeimeibodi, Christopher J. K. Richardson, Richard P. Leavitt, Dirk Englund, and Edo Waks. Hybrid integration of solid-state quantum emitters on a silicon photonic chip. *Nano Letters*, 17(12):7394–7400, nov 2017.
- [64] E. Yablonovitch, T. Sands, D. M. Hwang, I. Schnitzer, T. J. Gmitter, S. K. Shastry, D. S. Hill, and J. C. C. Fan. Van der waals bonding of GaAs on pd leads to a permanent, solid-phase-topotaxial, metallurgical bond. *Applied Physics Letters*, 59(24):3159–3161, dec 1991.
- [65] H. Qiang, Fred H. Pollak, and Grayce Hickman. Piezo-photorefectance of the direct gaps of GaAs and Ga_{0.78}Al_{0.22}As. *Solid State Communications*, 76(9):1087–1091, dec 1990.
- [66] Benjamin Paschke, Achim Wixforth, Dmytro Denysenko, and Dirk Volkmer. Fast surface acoustic wave-based sensors to investigate the kinetics of gas uptake in ultra-microporous frameworks. *ACS Sensors*, 2(6):740–747, may 2017.

- [67] Matthias Weiß, Florian J R Schülein, Jörg B Kinzel, Michael Heigl, Daniel Rudolph, Max Bichler, Gerhard Abstreiter, Jonathan J Finley, Achim Wixforth, Gregor Koblmüller, and Hubert J Krenner. Radio frequency occupancy state control of a single nanowire quantum dot. *Journal of Physics D: Applied Physics*, 47(39):394011, sep 2014.
- [68] Matthias Weiß, Jörg B. Kinzel, Florian J. R. Schülein, Michael Heigl, Daniel Rudolph, Stefanie Morkötter, Markus Döblinger, Max Bichler, Gerhard Abstreiter, Jonathan J. Finley, Gregor Koblmüller, Achim Wixforth, and Hubert J. Krenner. Dynamic acoustic control of individual optically active quantum dot-like emission centers in heterostructure nanowires. *Nano Letters*, 14(5):2256–2264, apr 2014.
- [69] Emeline D. S. Nysten, Armando Rastelli, and Hubert J. Krenner. A hybrid (al)GaAs-LiNbO₃ surface acoustic wave resonator for cavity quantum dot optomechanics. *Applied Physics Letters*, 117(12):121106, sep 2020.
- [70] M. Rotter, C. Rocke, S. Böhm, A. Lorke, A. Wixforth, W. Ruile, and L. Korte. Single-chip fused hybrids for acousto-electric and acousto-optic applications. *Applied Physics Letters*, 70(16):2097–2099, apr 1997.
- [71] Clark Nguyen. MEMS technology for timing and frequency control. *IEEE Transactions on Ultrasonics, Ferroelectrics and Frequency Control*, 54(2):251–270, 2007.
- [72] D. T. Nguyen, C. Baker, W. Hease, S. Sevil, P. Senellart, A. Lemaître, S. Ducci, G. Leo, and I. Favero. Ultrahigh q-frequency product for optomechanical disk resonators with a mechanical shield. *Applied Physics Letters*, 103(24):241112, dec 2013.
- [73] Matthias Weiß, Daniel Wigger, Maximilian Nägele, Kai Müller, Jonathan J. Finley, Tilmann Kuhn, Paweł Machnikowski, and Hubert J. Krenner. Nonlinear quantum dot optomechanics. *Optica*, 8(3):291, mar 2021.
- [74] Liang Zhai, Matthias C. Löbl, Jan-Philipp Jahn, Yongheng Huo, Philipp Treutlein, Oliver G. Schmidt, Armando Rastelli, and Richard J. Warburton. Large-range frequency tuning of a narrow-linewidth quantum emitter. *Applied Physics Letters*, 117(8):083106, aug 2020.
- [75] Bruno Villa Piñeros. Dynamic acoustic control of semiconductor quantum dot-based devices for quantum light generation. 2020.
- [76] W. Bogaerts, P. De Heyn, T. Van Vaerenbergh, K. De Vos, S. Kumar Selvaraja, T. Claes, P. Dumon, P. Bienstman, D. Van Thourhout, and R. Baets. Silicon microring resonators. *Laser & Photonics Reviews*, 6(1):47–73, sep 2011.
- [77] G. C. Righini, Y. Dumeige, P. Féron, M. Ferrari, G. Nunzi Conti, D. Ristic, and S. Soria. Whispering gallery mode microresonators: Fundamentals and applications. *Rivista Del Nuovo Cimento*, 34(7):435–488, 2011.

- [78] Alexander Gondarenko, Jacob S. Levy, and Michal Lipson. High confinement micron-scale silicon nitride high q ring resonator. *Optics Express*, 17(14):11366, jun 2009.
- [79] Qing Li, Marcelo Davanço, and Kartik Srinivasan. Efficient and low-noise single-photon-level frequency conversion interfaces using silicon nanophotonics. *Nature Photonics*, 10(6):406–414, apr 2016.
- [80] Christian Reimer, Michael Kues, Piotr Roztocky, Benjamin Wetzal, Fabio Grazioso, Brent E. Little, Sai T. Chu, Tudor Johnston, Yaron Bromberg, Lucia Caspani, David J. Moss, and Roberto Morandotti. Generation of multiphoton entangled quantum states by means of integrated frequency combs. *Science*, 351(6278):1176–1180, mar 2016.
- [81] E. M. Purcell. Spontaneous emission probabilities at radio frequencies. *Physical Review*, 69:681, 1946.
- [82] M. Weiß, S. Kapfinger, T. Reichert, J. J. Finley, A. Wixforth, M. Kaniber, and H. J. Krenner. Surface acoustic wave regulated single photon emission from a coupled quantum dot–nanocavity system. *Applied Physics Letters*, 109(3):033105, jul 2016.
- [83] B. Villa, A. J. Bennett, D. J. P. Ellis, J. P. Lee, J. Skiba-Szymanska, T. A. Mitchell, J. P. Griffiths, I. Farrer, D. A. Ritchie, C. J. B. Ford, and A. J. Shields. Surface acoustic wave modulation of a coherently driven quantum dot in a pillar microcavity. *Applied Physics Letters*, 111(1):011103, jul 2017.
- [84] S. H. Wemple and M. DiDomenico. Theory of the elasto-optic effect in nonmetallic crystals. *Physical Review B*, 1(1):193–202, jan 1970.
- [85] Maurício M de Lima and Paulo V Santos. Modulation of photonic structures by surface acoustic waves. *Reports on Progress in Physics*, 68(7):1639–1701, jun 2005.
- [86] Antonio Crespo Poveda, Dominik D Bühler, Andrés Cantarero Sáez, Paulo V Santos, and Maurício M de Lima. Semiconductor optical waveguide devices modulated by surface acoustic waves. *Journal of Physics D: Applied Physics*, 52(25):253001, apr 2019.
- [87] Wei Fu, Zhen Shen, Yuntao Xu, Chang-Ling Zou, Risheng Cheng, Xu Han, and Hong X. Tang. Phononic integrated circuitry and spin–orbit interaction of phonons. *Nature Communications*, 10(1):2743, June 2019.
- [88] Farid Tajaddodianfar, Mohammad Reza Hairi Yazdi, and Hossein Nejat Pishkenari. Nonlinear dynamics of MEMS/NEMS resonators: analytical solution by the homotopy analysis method. *Microsystem Technologies*, 23(6):1913–1926, may 2016.
- [89] F. R. Braakman, D. Cadeddu, G. Tütüncüoğlu, F. Matteini, D. Ruffer, A. Fontcuberta i Morral, and M. Poggio. Nonlinear motion and mechanical mixing in as-grown GaAs nanowires. *Applied Physics Letters*, 105(17):173111, oct 2014.

- [90] I. Kozinsky, H. W. Ch. Postma, I. Bargatin, and M. L. Roukes. Tuning nonlinearity, dynamic range, and frequency of nanomechanical resonators. *Applied Physics Letters*, 88(25):253101, jun 2006.
- [91] Linbo Shao, Smarak Maity, Lu Zheng, Lue Wu, Amirhassan Shams-Ansari, Young-Ik Sohn, Eric Puma, M.N. Gadalla, Mian Zhang, Cheng Wang, Evelyn Hu, Keji Lai, and Marko Lončar. Phononic band structure engineering for high- q gigahertz surface acoustic wave resonators on lithium niobate. *Physical Review Applied*, 12(1), jul 2019.
- [92] Sarah Benchabane, Aymen Jallouli, Laetitia Raguin, Olivier Gaiffe, Jules Chatellier, Valérie Soumann, Jean-Marc Cote, Roland Salut, and Abdelkrim Khelif. Non-linear coupling of phononic resonators induced by surface acoustic waves.
- [93] Walter L. Bond. The mathematics of the physical properties of crystals. *Bell System Technical Journal*, 22(1):1–72, jan 1943.
- [94] R. S. Weis and T. K. Gaylord. Lithium niobate: Summary of physical properties and crystal structure. *Applied Physics A Solids and Surfaces*, 37(4):191–203, aug 1985.
- [95] R. T. Smith and F. S. Welsh. Temperature dependence of the elastic, piezoelectric, and dielectric constants of lithium tantalate and lithium niobate. *Journal of Applied Physics*, 42(6):2219–2230, may 1971.
- [96] A.S. Jordan. An evaluation of the thermal and elastic constants affecting GaAs crystal growth. *Journal of Crystal Growth*, 49(4):631–642, aug 1980.
- [97] Ireneusz Strzalkowski, Sharad Joshi, and C. R. Crowell. Dielectric constant and its temperature dependence for GaAs, CdTe, and ZnSe. *Applied Physics Letters*, 28(6):350–352, mar 1976.
- [98] Nobuo Suzuki and Kunio Tada. Elastooptic and electrooptic properties of GaAs. *Japanese Journal of Applied Physics*, 23(Part 1, No. 8):1011–1016, aug 1984.

List of Publications

Published Papers

- **Annealing effects on the magnetic properties of highly-packed vertically-aligned nickel nanotubes**
Vlad-Andrei Antohe, Emeline Nysten, Juan Manuel Martínez-Huerta, Pedro Miguel Pereira de Sá and Luc Piraux
RSC Advances, 7(30):18609-18616, 2017, doi: 10.1039/C7RA01276D
- **Multi-harmonic quantum dot optomechanics in fused LiNbO₃-(Al)GaAs hybrids**
Emeline D. S. Nysten, Yong Heng Huo, Hailong Yu, Guo Feng Song, Armando Rastelli and Hubert J. Krenner
Journal of Physics D: Applied Physics, 50(43):43LT01, 2017, doi: 10.1088/1361-6463/aa861a
- **The 2019 surface acoustic waves roadmap**
Per Delsing, Andrew N Cleland, Martin J A Schuetz, Johannes Knörzer, Géza Giedke, J Ignacio Cirac, Kartik Srinivasan, Marcelo Wu, Krishna Coimbatore Balram, Christopher Bäuerle, Tristan Meunier, Christopher J B Ford, Paulo V Santos, Edgar Cerda-Méndez, Hailin Wang, Hubert J Krenner, Emeline D S Nysten, Matthias Weiß, Geoff R Nash, Laura Thevenard, Catherine Gourdon, Pauline Rovillain, Max Marangolo, Jean-Yves Duquesne, Gerhard Fischerauer, Werner Ruile, Alexander Reiner, Ben Paschke, Dmytro Denysenko, Dirk Volkmer, Achim Wixforth, Henrik Bruus, Martin Wiklund, Julien Reboud, Jonathan M Cooper, YongQing Fu, Manuel S Brugger, Florian Rehfeldt and Christoph Westerhausen
Journal of Physics D: Applied Physics, 52(35):353001, 2019, doi: 10.1088/1361-6463/ab1b04
- **Quantum Dot Optomechanics in Suspended Nanophononic Strings**
Anja Vogele, Maximilian M. Sonner, Benjamin Mayer, Xueyong Yuan, Matthias Weiß, Emeline D. S. Nysten, Saimon F. Covre da Silva, Armando Rastelli and Hubert J. Krenner
Advanced Quantum Technologies, 3(2):1900102, 2019, doi: 10.1002/qute.201900102

- **A hybrid (Al)GaAs–LiNbO₃ surface acoustic wave resonator for cavity quantum dot optomechanics**

Emeline D. S. Nysten, Armando Rastelli and Hubert J. Krenner

Applied Physics Letters, 117(12):121106, 2020, doi: 10.1063/5.0022542

Submitted

- **On-chip optomechanical initialization and rotation of a photonic qubit**

Dominik D. Bühler, Matthias Weiß, Antonio Crespo-Poveda, Emeline D. S. Nysten,

Jonathan J. Finley, Kai Müller, Paulo V. Santos, Mauricio M. de Lima Jr. and

Hubert J. Krenner

Acknowledgement

At the end of this work, I would like to thank all the people who directly or indirectly contributed to this work and helped me throughout this project:

- Before anyone else, Hubert Krenner for supervising this work and for his enthusiasm, his resourceful ideas and exemplary supervision which was a driving force in the completion of this project.
- Achim Wixforth, for the supervision of the chair at which this work was conducted.
- Prof. Dr. Wolfgang Brütting for writing the assessment of this work.
- My colleague from the whole Hoobgroup for their great help, for having the best time in and out of the university and for being like a second family away from Belgium. Specifically, Matthias Weiß with whom I learned to efficiently measure single QDs and who helped with the correction of this work, Sebastian Hammer and Lisa Janker for their close help around the lab and my first introduction to PL measurement, Jens Putiowski for the development of the epitaxial lift-off technique at the chair and Tobias Petzak and Maximillian Sonner for their help and discussion in the lab. Leon Knez for the supervision of his bachelor lab work which helped me understand SAW resonators more completely.
- From SAWtrain, André Bilobran and Bruno Villa for their friendly and enriching collaboration as well as Chris Ford and Mauricio M. de Lima for the supervision on these projects. André Bilobran, Bruno Villa, Dominik Bühler and Hugo Lepage for making me feel welcomed and at home during my secondments in Valencia and Cambridge. All the PhD students of the SAWtrain Network for the long and amazing discussions as well as all the good time we had during our meetings and student retreats. All the senior members and supervisors of the SAWtrain Network for the interesting discussions and the organisation of a great collaborating network.
- Kai Müller, Jonathan Finley and their groups from the Walter Schottky Institut at the TU München for the fabrication of the QDs samples used in this work.

- Yong Heng Huo and Guo Feng Song from the Chinese Academy of Sciences in Beijing as well as Yong Heng Huo and Armando Rastelli and his group from the Johannes Kepler Universität in Linz for the fabrication of the QDs samples used in this work.
- Alexander Hupfer for being one of the first to welcome me at the chair and always being ready to be of help for any type of problems especially with my computer. The whole administrative and technical team (past and present) of the EP1 Lehrstuhl which keeps everything afloat: Sidonie Lieber, Andreas Hörner, Olga Ustinov, Andreas Spörhase, Adrian Mainka, Martina Mindt, Manuel Dreer and Funda Cevik for the help provided for any kind of problems.
- The complete EP1 Lehrstuhl for the great work atmosphere, the amazing fun we had in and out of work and for all the amazing memories and friends I made here.
- The whole Weiß family for welcoming me into their fold and helping me build a home here. The Zechel and Eggert families for welcoming me in Germany and helping me move from Belgium.
- My family and friends in Belgium for the great support all throughout this project and especially during the too long writing process. Especially my family, for keeping "my two feet on the ground" when stressing out and my papa for all the help during my studies and for the correction of this work even if just for the language.